

**ATOMISTIC MODELING OF THE MICROSTRUCTURE AND TRANSPORT  
PROPERTIES OF LEAD-FREE SOLDER ALLOYS**

by

Michael S. Sellers

August 23, 2010

A dissertation submitted to the Faculty of the Graduate School of the  
University at Buffalo, *State University of New York* in partial fulfillment  
of the requirements for the degree of

Doctor of Philosophy

*Department of Chemical and Biological Engineering*

Advisors: David A. Kofke and Cemal Basaran

# Copyright

Copyright by

Michael S. Sellers

2010

ii

# Acknowledgments

I would like to recognize the following people for their help, in one way or another, towards the completion of this work.

*My advisors, Dr. Cemal Basaran and Dr. David A. Kofke.* I am very fortunate to have worked for such skilled and understanding people. They spared no effort in providing me countless hours of guidance and chances to grow professionally. I owe each of them a great deal.

*My committee member and mentor, Dr. Jeffrey R. Errington.* Jeff has been a source of help and encouragement since the start of my research career and I am grateful for all the opportunities he has afforded me.

*My research professor and friend, Dr. Andrew J. Schultz.* NOBODY deserves such a selfless mentor! His chief quality is his unwavering patience...patience, and knowledge...knowledge and patience...His two principal qualities are his considerable knowledge and unwavering patience...and his willingness to help...His *three* top qualities are his considerable knowledge, unwavering patience, and willingness to help...and his valuable and sincere opinions. His *four*...no...Amongst his qualities...Composing Andrew's character are such elements as unwavering patience, considerable knowledge... I'll tell him in person.

*My group members and friends.* Particularly Tai Boon Tan, Katherine Shaul, Hye Min Kim, and Nancy Cribbin. I could not ask for better lab mates. I envy their talent and motivation, and will enjoy watching their continued success in the coming years. Our humorous discussions, group parties, and relaxing lunches will be missed. Also, Shidong Li, Bicheng Chen, Tarek Regab, Yongchang Lee, and Eray Gunel of the Electronics Packaging Laboratory, and Peter Mersich, Thomas Rosch, Eric Grzelak, and Ravi Chopra. Graduate school was enjoyable because of such wonderful friends.

*My parents, my sister, and Diane Youker.* I could not have done this without them. My conversations with Diane make the tough days much easier and her love and companionship gives me something wonderful to come home to. I also thank my sister Liz for all her encouragement. And finally, I am truly grateful for my parents' support and love. I owe a part of everything I accomplish to you both.

# Table of Contents

Copyright .....	ii
Acknowledgments .....	iii
Table of Contents.....	v
Tables and Figures .....	ix
Abstract.....	xv
Published Work .....	xviii
Introduction.....	1
1.1 Modeling Damage Mechanics in Solder Joints .....	2
1.1.1 Electromigration and Other Damage Phenomena.....	4
1.1.2 Thermodynamic Models and the Atomistic Realm .....	7
1.2 Objectives .....	10

1.3	Outline.....	10
	Models and Methodology for Surfaces and Interfaces.....	12
2.1	Material Structures and Molecular Models.....	13
2.1.1	Modeling $\beta$ Sn, and Sn-Ag, Sn-Cu Alloys .....	13
2.1.2	Crystal Lattice Structures.....	19
2.1.3	Constructing Interfaces .....	20
2.2	Computing Transport Properties.....	22
2.2.1	Mechanism Search with the Dimer Method .....	22
2.2.2	Diffusivity from Harmonic Transition State Theory .....	26
2.2.3	Diffusivity Computation Techniques with Molecular Dynamics.....	27
2.3	Energetics and Structure of Surfaces and Interfaces.....	31
2.3.1	Excess Potential Energies of Surfaces and Interfaces.....	31
2.3.2	Solute Contributions to Interfacial Energy .....	34
2.3.3	Identifying Regions of Structure in Grain Boundaries .....	36
2.4	Atomic Level Stress: An Introduction and Case Study .....	37
2.4.1	Macroscale Connection to Atomic Stress.....	37
2.4.2	Relationships for Volumetric Strain .....	38
2.4.3	Embedded-Atom Method.....	40
2.4.4	Virial Stress.....	42
2.4.5	Molecular Dynamics Simulation of Lattice Vacancy.....	43
2.4.6	Computing the Volumetric Strain from Simulation.....	44
2.4.7	Validation with Continuum Mechanics Methods .....	46
2.4.8	Conclusions.....	48
	Surface Energies and Adatom Diffusivity.....	50
3.1	Simulation Details.....	52
3.2	Results and Discussion .....	55
3.2.1	Surface Energy Calculation for $\beta$ Sn .....	55

3.2.2	Surface Diffusion on (100) .....	56
3.3	Conclusions.....	60
Grain Boundary Structure and Self-Diffusivity .....		62
4.1	Simulation Details.....	64
4.2	Results and Discussion .....	65
4.2.1	Grain Boundary Excess Potential Energies .....	65
4.2.2	Grain Boundary Width-Scaled Diffusivity ( $\delta_{GB}D_{GB}$ ).....	66
4.2.3	Grain Boundary Width Calculation .....	68
4.2.4	Resolving the Grain Boundary Diffusivity ( $D_{GB}$ ).....	75
4.2.5	Analysis of In-plane Directional Diffusivity .....	77
4.3	Conclusions.....	80
Solute Effects on Grain Boundary Energy and Shear Stress.....		83
5.1	Simulation Details.....	85
5.2	Results and Discussion .....	89
5.2.1	Excess Enthalpy Calculations .....	89
5.2.2	Segregation Enthalpies from Molecular Simulation.....	92
5.2.3	Segregation Enthalpies from Experimental Diffusion Measurements.....	93
5.2.4	Discussion of Experimental Behavior .....	94
5.2.5	Special Boundary Simulations.....	96
5.2.6	Boundary Under Shear Strain.....	98
5.2.7	Boundary Sliding in Solute Segregated Boundaries.....	104
5.2.8	Interface Structure During High Temperature Sliding .....	105
5.3	Conclusions.....	107
Solute Effects on Grain Boundary Self-Diffusivity .....		110
6.1	Simulation Details.....	111
6.2	Results and Discussion .....	113
6.2.1	Width-scaled Self-Diffusivity ( $\delta_{GB}D_{GB}$ ) of Sn .....	113

6.2.2	Planar Self-Diffusivity Profiles and Interface Width.....	115
6.2.3	Effect of Atomic Size and Cohesive Energy .....	121
6.2.4	Grain Boundary Self-Diffusivity ( $D_{GB}$ ) of Sn .....	124
6.3	Conclusions.....	126
Conclusions and Future Work .....		129
7.1	Original Contributions .....	133
7.2	Recommendations of Future Work.....	134
References.....		136

# Tables and Figures

## List of Tables

Table 2-1 Parameters for the MEAM potential. ....	18
Table 2-2 Al material properties used in simulations, after Sarychev. [15] .....	43
Table 2-3 Vacancy relaxation factors as reported by authors.....	45
Table 3-1 Dimer method parameters. ....	54
Table 3-2 Surface energies $\gamma_s$ of $\beta$ Sn, Cu, Ag, and Al with respect to Miller plane orientation. Cu, Ag, and Al are reproduced from [19]. ....	55
Table 3-3 Mechanism data. Respectively, the adatom direction, mechanism activation energy, attempt frequency, distance the adatom traveled, and tracer diffusivity at 300K are specified. ....	58
Table 4-1 Excess Interfacial Potential Energies ( $\text{mJ}/\text{m}^2$ ) at 300K.....	66
Table 4-2 Arrhenius properties calculated from experiment in ref [10]......	67

Table 4-3 Arrhenius Properties of Simulated Grain Boundaries from weighted least squares fit, 325K to 450K.....	76
Table 5-1 Ag and Cu solute quantities and corresponding excess interfacial density.....	86
Table 5-2 Ag solute calculations of enthalpy of segregation ( $\Delta H^{seg}$ ), critical excess interfacial concentration ( $\Gamma_{cr}$ ), and critical number of solute atoms ( $N_{A,cr}$ ). Error is a weighted least squares fit on <i>Figure 5-3</i> – Ag slope. ....	91
Table 5-3 Cu solute calculations of enthalpy of segregation ( $\Delta H^{seg}$ ), critical excess interfacial concentration ( $\Gamma_{cr}$ ), and critical number of solute atoms ( $N_{A,cr}$ ). Error is a weighted least squares fit on <i>Figure 5-3</i> – Cu slope.....	91
Table 5-4 Ag and Cu solute calculations of enthalpy of segregation ( $\Delta H^{seg}$ ) for various boundaries of $\beta$ Sn at 300K. Error is a weighted least squares fit of $H_{EX,GB+S}$ vs. $I^{EX}$ ..	97
Table 6-1 Ag and Cu solute quantities and corresponding excess interfacial density...	112

## List of Figures

Figure 1-1 Damage from high electrical current density in PbSn solder joint. Red arrows indicate direction of electron flow. ....	3
Figure 1-2 A multi solder joint finite element model. Arrows indicate direction of electrical current flow. [4].....	4
Figure 1-3 Electron wind effect on metal atoms, the main driving force in electromigration. ....	5
Figure 1-4 An SEM image of a solder joint microstructure colored by $\beta$ Sn grain orientation. ....	10
Figure 2-1 Crystal structures of $\beta$ Sn (TOP) and its alloys in $L1_2$ (BOTTOM) represented by the MEAM potential. Dimensions on lattice indicate tetragonal crystal structure (TOP) and cubic crystal structure (BOTTOM). Lattice images courtesy of ref. [29]. .	19
Figure 2-2 Shown LEFT are various Miller planes in $\beta$ Sn's lattice. RIGHT is the rotation of two grains to share a common Miller plane. Red, Blue, and Purple, are (101), (201), and (401) Miller planes, respectively. Green and Orange are (310) and (410), respectively. Note that the <i>side</i> view x-direction is stretched for figure height conformity. X-direction corresponds to the lattice a-direction, [100]; Z-direction corresponds to the lattice c-direction, [001]. ....	20

Figure 2-3 Simulation snapshot of the (101) grain boundary of $\beta$ Sn. Dark atoms are Sn, green are Ag solute at the interface. Structure is 3-dimensional and view is looking down the y-direction at the x-z plane.....	21
Figure 2-4 (1) Typical locations on the energy hyper-surface for minima and saddle points. (2) An atomistic system represented by a point on the energy hyper-surface. (3) Multiple points (systems) with their distance in hyper-surface space maintained. Colored hyper surface adapted from ref [33].....	24
Figure 2-5 When tracing the path of minimum energy from the saddle point to minimum, the dimer is rotated to a minimum energy via steepest descent (a) and then stepped (b), maintaining the correct orientation along the lowest curvature mode. This routine is repeated until the center of the dimer is at a minimum energy.....	25
Figure 2-6 Planar diffusivity vs. z-coordinate in the simulation cell. [h] is the maximum of the diffusion profile and [ $\delta$ ] is the width at [h]/2. Background is grain boundary rotated with z-axis parallel to planar diffusivity plot abscissa. Points on plot correspond to lattice planes in background separated by $\Delta z$ . .....	30
Figure 2-7 The two systems considered in excess potential energy calculations of a free surface. Orange lines are Miller planes; Green dashed lines are fixed free surfaces....	32
Figure 2-8 The three systems considered in excess potential energy calculations of a grain boundary. Orange lines are Miller planes; Green dashed lines are fixed free surfaces. ....	33
Figure 2-9 The variation of $ S(k) ^2$ , for a bulk solid at 0K and 300K, and a grain boundary at 300K. Note the abscissa is the direction perpendicular to the interface. Error bars represent the standard deviation of $ S(k) ^2$ in five snapshots of an MD run. 37	37
Figure 2-10 A plot of first-nearest neighbor distance from center of an atom (or void), versus simulation time steps in molecular dynamic simulations. Filled black circles indicated a full lattice and open circles indicate a vacancy, where the atom is removed at 10ps into the data collection run. Average neighbor positions before and after atom removal are 2.891 +/-0.009 and 2.831 +/-0.010, respectively. ....	45
Figure 2-11 Void model in continuum mechanics domain.....	47
Figure 2-12 Free body diagram under spherical coordinate system. ....	47
Figure 3-1 LEFT a z-direction, top view of the (100) surface. RIGHT a 3-dimensional view of the simulation cell. Atoms are colored white to denote movable by the dimer method and gray for fixed.....	54

Figure 3-2 Energy maps of the $\beta$ Sn (100) surface. Left. Red denotes a higher energy (ion cores), blue denotes lower energy. Right. Diamonds are respective saddle point locations of the adatom, white circles are minima locations. ....	57
Figure 3-3 Energy values along the minimum energy path for the given mechanisms. Values along the reaction coordinate are corrected to a baseline value of the minimum energy configuration—both mechanisms begin and finish at 0eV. Diamonds denote energies corresponding to saddle point configurations.....	58
Figure 3-4 Arrhenius plot of diffusivity with respect to inverse temperature. ....	60
Figure 4-1 (1) Minimization (near 0K-MD), (2) Equilibration, and (3) Production structures. Actual simulation cells are 3-dimensional and periodic in x and y-directions.....	65
Figure 4-2 Arrhenius plot of scaled diffusivity vs. temperature. Points are results for various symmetric tilt grain boundaries simulated in this work. Dark lines are experimental data from Singh and Ohring. [9] Error bars represent standard deviation of three independent simulations and computations of $\delta_{GB}D_{GB}$ .....	67
Figure 4-3 Planar diffusivity for various grain boundaries at 300K (left) and 450K (right). Note the different scales for each temperature, but similar scales for z. Lines are guides for the eye. ....	69
Figure 4-4 Square planar structure factor vs. z-axis plane for the five grain boundaries studied. Colors are different temperatures. Blue-300K, Green-350K, Orange-400K, Red-450K. Error bars represent the standard deviation of $ S(k) ^2$ in five snapshots from an MD run.....	71
Figure 4-5 TOP and BOTTOM are snapshots of the (101) GB at 300K and 450K, respectively. LEFT is looking parallel to the grain tilt axis and at RIGHT looking perpendicular.....	72
Figure 4-6 Diffusive (open points, left) and structural widths (filled points, right) versus temperature for the five grain boundaries studied. Lines are guides for the eye. Black lines is the diffusive width used in ref [9].....	73
Figure 4-7 An Arrhenius plot of grain boundary diffusivity vs. temperature. Shown as colored points are various symmetric tilt grain boundaries simulated in this work. Dark lines are experimental data from Singh and Ohring. Error bars represent standard deviation of three or more independent simulations.....	77
Figure 4-8 Arrhenius plots of scaled directional diffusivity vs. temperature. Left are (310) and (410) grain boundaries, Right are (101), (201), and (401) grain boundaries.	

Filled points are diffusion in a direction perpendicular to the grain tilt axis; Open points are diffusion in a direction parallel to the grain tilt axis. Letters in parentheses in the plot legends are crystal lattice directions of diffusion. Error bars represent standard deviation of three or more independent simulations..... 79

Figure 4-9 Simulation snapshot of (401) grain boundary at 450K. LEFT is looking down the grain tilt axis and at RIGHT the grain tilt axis is oriented left/right..... 80

Figure 5-1 Typical configuration of grain boundary with its interface loaded with solute (orange). LEFT is a simulation snapshot after equilibration and RIGHT is the same snapshot with the interface exposed for clarity..... 86

Figure 5-2 (1) Grain boundary minimization (near 0K), (2) Solute minimization, (3) NPT MD equilibration, (4) NVT MD Shear simulation. Filled arrows indicate direction of motion of the block portion. Orange circles are solute at interface. Free atoms are movable in x, y, and z directions. Actual simulation cells are 3-dimensional and periodic in x and y directions..... 87

Figure 5-3 Difference in the excess enthalpies of the solute loaded grain boundary and bulk  $\beta$ Sn with an equal amount of solute ( $H_{EX,GB+S}$ ) vs. excess solute concentration ( $I^{EX}$ ). Error is the standard deviation. Trend lines are fitted by a weighted least-squares analysis..... 90

Figure 5-4 Shear stress ( $\tau_{xz}$ ) vs. average strain ( $\gamma_{avg}$ ) for four strain rates at 300K. Curve labels point to yield stress in various shear strain rates, decreasing from top to bottom. Lowest label is stoppage of shear rate of  $6.25 \times 10^6 \text{ s}^{-1}$  at a strain of 0.0375, to simulate a steady state condition..... 99

Figure 5-5 Shear stress ( $\tau_{xz}$ ) vs. average strain ( $\gamma_{avg}$ ) for three solute amounts of Ag at 300K and 450K. Number in squares are solute atom amounts. Curves at 300K are the average of three independent simulation runs. Note different scales for 300K and 450K..... 101

Figure 5-6 Shear stress ( $\tau_{xz}$ ) vs. average strain ( $\gamma_{avg}$ ) for three solute amounts of Cu at 300K and 450K. Number in squares are solute atom amounts. Curves at 300K are the average of three independent simulation runs. Note different scales for 300K and 450K..... 102

Figure 5-7 Structural formation in pure GB interface at 450K under shear. (1) Side view in y-z plane. (2) Side view in x-z plane, shear direction indicated. (3) Top view of full BCC structure and separate lattice planes..... 107

Figure 6-1 (1) minimization (MD near 0K), (2) solute minimization (conjugate gradient), (3) equilibration, (4) production structures. Black arrows indicate direction of motion of the block portion. Free atoms are movable in x, y, and z directions. Actual simulation cells are 3-dimensional and periodic in x and y directions. ....	112
Figure 6-2 Width-scaled self-diffusivity of Sn vs. temperature for various solute atom quantities. LEFT is Ag solute, RIGHT is Cu solute. Error bars are standard deviation from three or more simulation runs. ....	115
Figure 6-3 Planar self-diffusivity profiles in z-direction of Sn for various solute atom quantities of Ag at a particular temperature. Note different scales on each ordinate. ....	117
Figure 6-4 Self-planar diffusivity profiles in z-direction of Sn for various solute atom quantities of Cu at a particular temperature. Note different scales on each ordinate. ....	118
Figure 6-5 Diffusive width vs. temperature for various solute concentrations. LEFT is Ag and RIGHT is Cu. Circle points (black) are the pure $\beta$ Sn grain boundary widths. ....	119
Figure 6-6 Rendered simulation snapshot of two grain boundaries at 450K and containing 50 solute atoms in the interface. LEFT is Ag (green) and RIGHT is Cu (orange). ....	121
Figure 6-7 Self-planar diffusivity profiles of $\beta$ Sn in z-direction for solute atom quantities of 50 at various temperatures. LEFT is Ag and RIGHT is Cu. Note different scales on ordinate. ....	124
Figure 6-8 Self-diffusivity of Sn vs. temperature for various solute atom quantities. LEFT is Ag solute, RIGHT is Cu solute. ....	126

# Abstract

# Abs

Damage mechanics models of lead-free solder joints in nanoelectronics continue to improve, and in doing so begin to utilize quantitative values describing processes at the atomic level, governing phenomena like electromigration and thermomigration. In particular, knowledge of the transport properties of specific microstructures helps continuum level models fully describe these larger-scale damage phenomena via multi-scale analysis. For example, diffusivities for different types of grain boundaries (fast diffusion paths for solvent and solute atoms, and vacancies), and a description of the boundary structure as a function of temperature, are critical in modeling solder microstructure evolution and, consequently, joint behavior under extreme temperature and electric current. Moreover, for damage that develops at larger length scales, surface

energies and diffusivities play important roles in characterizing void stability and morphology.

Unfortunately, experiments that investigate these kind of damage phenomena in the atomistic realm are often inconsistent or unable to directly quantify important parameters. One case is the particular transport and structural properties of grain boundaries in Sn (the main component in lead-free solder alloys) and their behavior in the presence of Ag and Cu impurities. This information is crucial in determining accurate diffusivity values for the common SnAgCu (SAC) type solder. Although an average grain boundary diffusivity has been reported for polycrystalline Sn in several works, the value for grain boundary width is estimated and *specific* diffusivities for boundaries known to occur in Sn have not been reported, to say nothing of solute effects on Sn diffusivity and grain boundary structure. Similarly, transport properties of Sn surfaces remain relatively uninvestigated as well. These gaps and inconsistencies in atomistic data must be remedied for micro- and macro-scale modeling to improve.

As a complement to experimental work and possessing the ability to fill in the gaps, molecular simulation serves to reinforce experimental predictions and provide insight into the atomistic processes that govern studied phenomena. In the present body of work, we employ molecular statics and dynamics simulations in the characterization and computation of  $\beta$ Sn surface energies and surface diffusivities, the determination of diffusivities and structural properties of specific  $\beta$ Sn grain boundaries, and the investigation of Cu and Ag solute effects on  $\beta$ Sn grain boundaries.

In our study of  $\beta$ Sn surfaces, energies for low number Miller index surfaces are computed and the (100) plane is found to have the lowest un-relaxed energy. We then find that two simple hopping mechanisms dominate adatom diffusion transitions on this surface. For each, we determine hopping rates of the adatom and compute its tracer diffusivity.

Our work on grain boundaries investigates the self-diffusion properties and structure of several  $\beta$ Sn symmetric tilt grain boundaries using molecular dynamics simulations. We find that larger diffusive widths are exhibited by higher excess potential energy grain boundaries. Diffusivities in the directions parallel to the interface plane are also computed and activation energies are found with the Arrhenius relation. These are shown to agree well with experimental data.

Finally, we examine the effect that solute atoms of Ag and Cu have on the microstructure of  $\beta$ Sn. Excess energies of the (101) symmetric tilt  $\beta$ Sn grain boundary are computed as a function of solute concentration at the interface, and we show that Ag lowers the energy at a greater rate than Cu. We also quantify segregation enthalpies and critical solute concentrations (where the excess energy of the boundary is reduced to zero). The effect of solute type on shear stress is also examined, and we show that solute has a strong effect on the stabilization of higher energy grain boundaries under shear stress. We then look at the self-diffusivity of Sn in the (101) symmetric tilt  $\beta$ Sn grain boundary and show that adding both Ag or Cu decrease the grain boundary self-diffusivity of Sn as solute amount in the interface increases. Effects of larger concentrations of Cu in particular are also investigated.

# Published Work

## Section 2.4 Models and Methods for Surfaces and Interfaces

Li, S., Sellers, M.S., Basaran, C., Schultz, A.J., Kofke, D.A. *Lattice Strain Due to an Atomic Vacancy*. Int. J. Mol. Sci., 10(6), pp 2798-2808 (2009).

## Chapter 3 Surface Energies and Adatom Diffusivity

Sellers, M.S., Schultz, A.J., Kofke, D.A., Basaran, C. *Atomistic Modeling of Tin Surface Energies and Adatom Diffusivity*. Applied Surface Science, 256(13), pp 4402-4407 (2010).

## Chapter 4 Grain Boundary Structure and Self-Diffusivity

Sellers, M.S., Schultz, A.J., Basaran, C., Kofke, D.A.  *$\beta$ Sn Grain Boundary Structure and Self-Diffusivity via Molecular Dynamics*. Physical Review B, 81(13), pp 4111-4121 (2010).

## Chapter 5 Solute Effects on Grain Boundary Energy and Stress

Sellers, M.S., Schultz, A.J., Basaran, C., Kofke, D.A. *Solute Effects on  $\beta$ Sn Grain Boundary Energy and Shear Stress*. Journal of Nanomechanics and Micromechanics. *Submitted* (August 2010).

## Chapter 6 Solute Effects on Grain Boundary Self-Diffusivity

Sellers, M.S., Schultz, A.J., Basaran, C., Kofke, D.A. *Effect of Cu and Ag Solute Segregation on  $\beta$ Sn Grain Boundary Diffusivity*. Physical Review B. *Under Review* (August 2010).

# Introduction



*“Therefore, since brevity is the soul of wit...”*

As analysis tools in computational materials science develop, transport properties at the atomistic level play an increasingly important role in the study of a material's behavior at large scales. Investigations once focused on the study of metals at a macroscopic level, such as finite element methods (FEM) for example, are now able to reach down into the nano-scale realm via multi-processor calculations utilizing simulation packages or software that can connect FEM and molecular simulation. As a result, in the world of macro-scale simulation, the value of information obtained about a material using molecular-level simulation techniques is being realized. Quantitative transport data explaining diffusion, cracking, or crystal growth rates, often difficult to study experimentally, can be had with relative ease using a molecular simulation package and a

few workstation grade computers. When used in conjunction with a larger-scale model, this information plays a key part in the description of microstructure and transport properties, and the phenomena they control at larger length and timescales.

## 1.1 Modeling Damage Mechanics in Solder Joints

The solder joint presents an interesting system for the application of both continuum and molecular level simulations. As the metal “glue” connecting almost all electrical components, from simple capacitors to powerful microprocessors, solder joints face damage from large temperature and electric current gradients that develop across the joint, even under normal operation. The effects from temperature and current manifest themselves as increased mass transport with solid phase growth, vacancy nucleation and cracking, extrusion at the component or circuit board interfaces, and surface whisker growth—all leading to the eventual failure or shorting of the joint (*figure 1-1*). This is acceptable in most of today’s consumer applications, as the physical lifetime of hardware is often eclipsed by the lifetime of the hardware’s computing power. However, in high power applications, or mission-critical scenarios where components are inaccessible for repair after deployment, eliminating or minimizing solder joint damage is crucial. Likewise, as electronic devices shrink, so does the joint’s cross-sectional area, thereby increasing the damage effects of electrical current—reducing these effects is key for the realization of nanoelectronics.

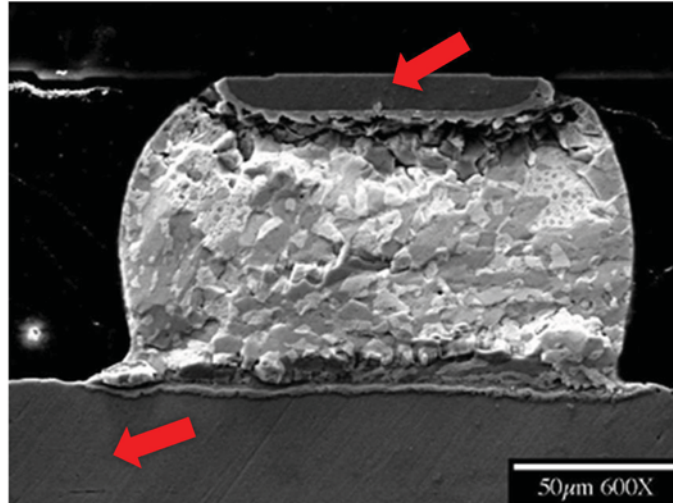
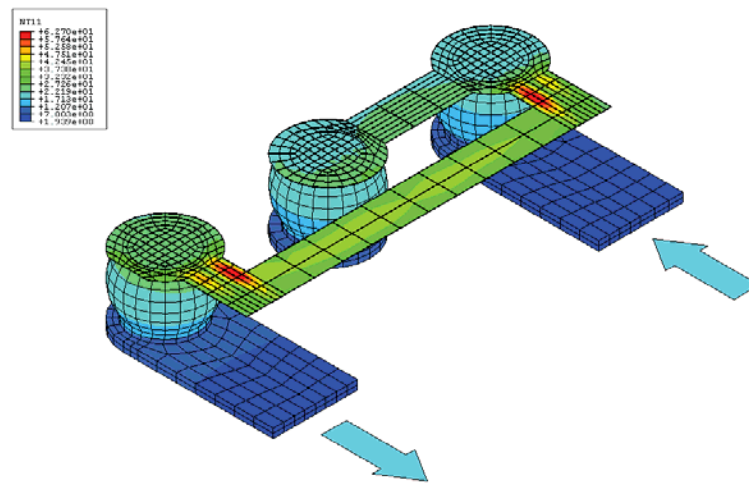


**Figure 1-1** Damage from high electrical current density in PbSn solder joint. Red arrows indicate direction of electron flow.

Quite a bit of research has been done at the continuum level on solder joints under thermal and electrical load. [1][2][3][4] A majority of this work is composed of finite element models of single or multiple solder joints that can describe the stress, temperature, and/or current profiles that develop during use. These simulations typically run faster than real-time, and are used to estimate *mean-time-to-failure* values for different joint types. Recent work in this domain has shown decent agreement with experimental results for older style solder joints, mostly alloys of Pb and Sn. [3] An example is shown in *figure 1-2*. In 2003, however, the European Union passed the *Restriction of Hazardous Substances* (RoHS) directive—partnered with the *Waste Electrical and Electronic Equipment* (WEEE) directive—that effectively removed the Pb component (among other compounds) from most future commercial electronic devices, and implemented a recycling program for older, lead-containing, products. [6] Several North American companies have followed this directive as well, advertising themselves

as *RoHS Compliant*. Replacements for the Pb component in solder vary from binary mixtures of Sn and Ag, Bi, Cu, In, Sb, or Zn, to combinations of a few of these, but a majority of the solder alloys in use today are over 90% Sn, 1.0-4.0% Ag, and contain trace amounts of Cu. [7] Current and temperature effects in these types of joints are equal to (if not worse than) PbSn joints, making damage modeling and a fundamental understanding of transport processes leading to this damage a high priority.



present in the solder also feel the force of the electron “wind”. If these solute atoms are much smaller than the host metal—as is the case with Cu and Ag present in Sn—they can rapidly diffuse through the host via an interstitial diffusion mechanism. [9][10][11]

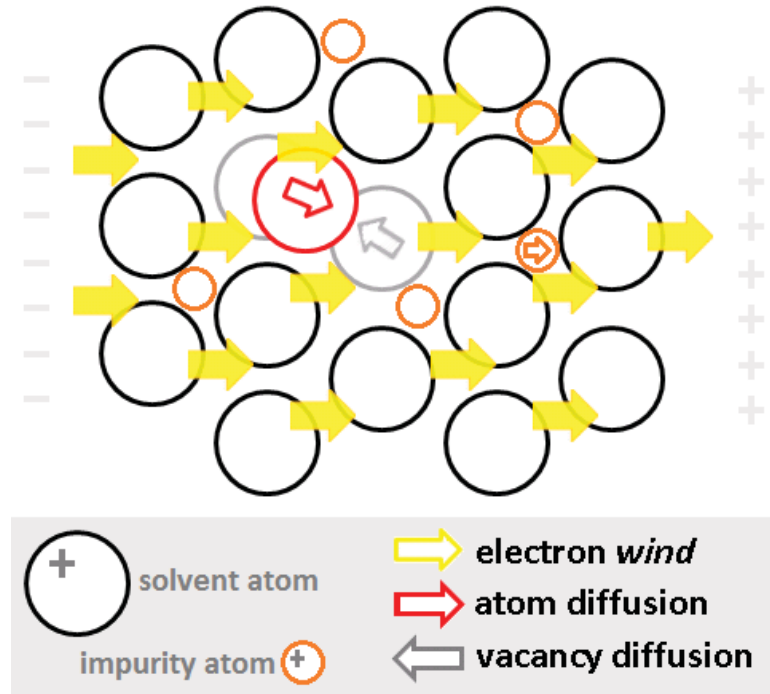


**Figure 1-3** Electron wind effect on metal atoms, the main driving force in electromigration.

As the solute and solvent atoms are pushed in one direction, the vacancies present in the metal are squeezed in the opposite direction. Micro-voids and cracking occur at the cathode side due to vacancy diffusion and coalescence at the interface. The “wind” force felt by the metal ion cores as conducting electrons collide with them is the main component in electromigration, and this force can be rigorously described for a particular material as

$$\begin{aligned}
F_{EM} &= F_{wind} + F_{field} \\
F_{EM} &= (-Z_{wind} + Z_{field}) \cdot e \cdot E \\
F_{EM} &= Z^* e \rho j
\end{aligned}
\tag{1-1}$$

Where  $F_{EM}$  is the combination of the electron wind force and the oppositely directed electric field force.  $E$  is the electric field potential,  $Z^*$  is the effective charge number (determined by electron wind forces),  $e$  is the charge of an electron,  $\rho$  is the resistivity of the metal, and  $j$  is the current density. As the electromigration force induces mass transfer in the joint, the force of stress counteracts it, where tensile stresses from vacancies cause cracking and compressive stresses from atom pileup cause extrusion. The negatively acting force of stress is represented by *equation (1-2)*.

$$F_{\sigma} = \Omega \nabla \sigma_h \tag{1-2}$$

Here,  $\Omega$  is the volume of an atom, and  $\sigma_h$  is the hydrostatic stress tensor. Additionally, the force derived from the concentration (or chemical potential) gradient opposes the electromigration force, and a component of this is the apparent force from a temperature gradient (dubbed thermomigration) which can aid or counteract the force of electromigration, depending on the direction of current flow relative to the hot component and cooler circuit board. Thus, the overall mass diffusion driving force on a solder joint can now be represented as *equation (1-3)*, where  $F_{EM}$  is the electromigration force,  $F_{TM}$  is the thermomigration force,  $F_{\sigma}$  is the stress, and  $F_{\mu}$  is the chemical potential force.

$$F = F_{EM} + F_{TM} + F_{\sigma} + F_{\mu} \quad (1-3)$$

### 1.1.2 Thermodynamic Models and the Atomistic Realm

There are a few models that relate the flux or dynamic concentration of vacancies in the solder joint to the various driving forces affecting mass diffusion that are outlined in *equation (1-3)*. Transport parameters within these models are determined by experiment, but often through secondary relationships that are not material specific, providing an avenue by which we can improve these models. In his 1993 work, Kirchheim explains a relation that connects macro-scale current density and stress gradients to atomistic vacancy diffusion—describing the change in vacancy flux based on the vacancy concentration gradient, current density, and stress gradients (respective terms in *equation (1-4)* below). [2] Several works apply this relation to aluminum thin films, and here molecular simulation has been used to determine the volumetric strain parameter,  $f$ , though it is often used inconsistently. [12][13][14] We revisit this point in Section 2.4. Other parameters such as atomic diffusivity in thin films are still based on experimental values.

$$J_v = -D_v \frac{\partial c_v}{\partial x} + \frac{D_v c_v}{kT} Z_v^* e E + \frac{D_v c_v}{kT} \Omega f \frac{\partial \sigma}{\partial x} \quad (1-4)$$

$J_v$ , vacancy flux vector

$D_v$ , effective vacancy diffusivity

$C_{eq}$ , vacancy concentration

$Z^*$ , vacancy effective charge number

$e$ , electron charge

$f$ , vacancy relaxation ratio, the ratio of the volume of an atom and the volume

of a vacancy

$\Omega$ , atomic volume

$\sigma = \text{trace}(\sigma_{ij})/3$ , hydrostatic or spherical part of the stress tensor

$k$ , Boltzman's constant

$T$ , absolute temperature

Describing more complex systems, Basaran et al. use a combination of Kirchheim's model including temperature effects with that of a model by Huntington to develop a damage evolution model for electromigration induced damage in SnAgCu solder joints (equation (1-5)). [4][16]

$$\frac{\partial c_v}{\partial t} = D_v \left[ \nabla^2 c_v - \frac{Z^* e \rho}{kT} \vec{\nabla} \cdot (c_v \vec{j}) + \frac{f \Omega}{kT} \vec{\nabla} \cdot (c_v \nabla \sigma) + \frac{Q^*}{kT^2} \vec{\nabla} \cdot (C_v \nabla T) \right] + G \quad (1-5)$$

$\rho$ , metal resistivity

$\vec{j}$ , current density vector

$Q^*$ , heat of transport, the isothermal heat transmitted by moving the atom in the process of jumping a lattice site less the intrinsic enthalpy

$G$ , vacancy generation rate,  $G = -\frac{C_v - C_{v,eq}}{\tau_s}$ ,

$C_{v,eq}$ , thermodynamic equilibrium vacancy concentration,

$$C_{v,eq} = C_{v0} \exp\left(\frac{(1-f)\Omega\sigma}{kT}\right)$$

$C_{v0}$ , equilibrium vacancy concentration in the absence of stress

$\tau_s$ , characteristic vacancy generation/annihilation time

Both of these relationships use vacancy diffusion as a damage metric for thin films and solder joints, respectively. It has been shown for aluminum thin films that the mass diffusion (vacancy diffusion) from electromigration takes place in the grain boundaries.

This was inferred by observing that the diffusion activation energy determined from *mean-time-to-failure* measurements was much lower than bulk aluminum activation energies, indicating some faster diffusion path other than the pure lattice. [15] Scanning electron microscope images present a clear picture of the grain boundaries present in pure Sn and lead-free solder alloys. [17] *Figure 1-4* shows the cross-section of a solder joint microstructure just after solidification. Shades of gray in this image are different orientations of  $\beta$ Sn grains. The interfaces these grains make with one another are called grain boundaries and allow for fast atomic diffusion because of low atomic bond coordination at the interface. Experimental work investigating the type and frequency of  $\beta$ Sn grain boundaries as a function of temperature, stress, and solute concentration have reached some important, but very general conclusions about stable boundary types and the effects of Ag and Cu on Sn microstructure. [17][18] However, specific characteristics that govern transport within the boundaries, such as a unique diffusivity and interface thickness, have not been quantified. Similarly, Ag and Cu effects on the formation of different size grains are not explained in detail, nor is their possible effect on Sn (vacancy) diffusivity in the boundary. This lack of transport and microstructural information forms the basis for this body of work.

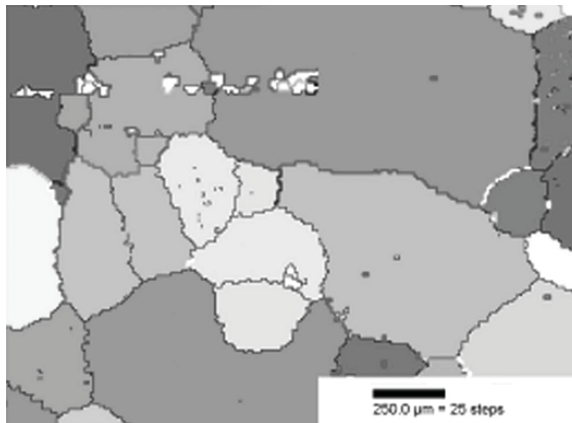


**Figure 1-4** An SEM image of a solder joint microstructure colored by  $\beta$ Sn grain orientation.

## 1.2 Objectives

With the opportunities for study developed in the previous section, this dissertation presents the goal of investigating the various structural regimes of  $\beta$ Sn present in lead-free solder joints. The transport and microstructure properties of these regimes are quantified. Additionally, we examine how these various systems react to changes in temperature and the presence of solute atoms, and provide justified explanations of their behavior under such conditions.

## 1.3 Outline

Chapter 2 continues this work, in which the simulation software, structures, and theoretical relationships used in the subsequent studies of  $\beta$ Sn are explained. Chapter 3 begins our investigation of lead-free solder with the calculation of surface energies and surface diffusivity, important quantities when modeling large voids that can develop in joints because of vacancy coalescence and solid phase growth. Next, we quantify the

transport characteristics of several grain boundaries of  $\beta\text{Sn}$  in Chapter 4 and compare them to average diffusivity measured from experiment. In Chapter 5, Ag and Cu solute effects on grain boundary energy leading to stable grain structure are investigated, and conclusions are drawn to better explain experimental observations of Sn- $x$ Ag and Sn- $x$ Cu microstructure formation. We also examine the effects of solute on shear stress as an additional metric for grain boundary stability. Chapter 6 ends our investigation of the solder system, by examining to what extent Ag and Cu atoms can aid or hinder Sn diffusion in the grain boundary. Finally, the general conclusions of the dissertation are presented and suggestions on future work are offered.

# Models and Methodology for Surfaces and Interfaces



*“Though this be madness, yet there is method in't.”*

As this dissertation continues, the studies of  $\beta$ Sn surfaces and interfaces will draw upon the simulation techniques, potential models, and relationships defining the properties of energy, structure, diffusivity, and stress in our simulations, that are outlined here. We begin with a description of the two primary types of systems studied, a  $\beta$ Sn surface and various  $\beta$ Sn grain boundaries, and the interatomic potential used. Next, we introduce a molecular statics technique for investigating diffusion mechanisms, and show how these results are used for the calculation of specific diffusivities. For systems simulated with molecular dynamics and exhibiting complex structure, modifications to the standard Einstein relation are then outlined for use in computing diffusivity in non-bulk like regions of a solid. Following this, quantities describing the difference in energy and

structure in comparison to bulk  $\beta$ Sn are developed. We then conclude this section with an introduction to atomic level stress and its relationship to the continuum, through a case study investigating vacancies in Al.

In subsequent chapters on particular investigations of surfaces and interfaces, one may find that variations or small additions to these methods are sometimes used. Explanations of this are found in the *Simulation Details* section of those chapters.

## 2.1 Material Structures and Molecular Models

This section outlines the interatomic potential used to describe Sn in various simulation styles. Also discussed are the interactions of two types of alloys commonly used in lead-free solder, as well as their equilibrium lattice structures and material properties.

### 2.1.1 Modeling $\beta$ Sn, and Sn-Ag, Sn-Cu Alloys

Over the past two decades, significant progress has been made in the computational simulation of metals through interatomic potential development. Molecular dynamics and Monte Carlo level simulation techniques now employ highly accurate and efficient potentials, parameterized from experiment and *ab initio* simulation methods. These potentials can duplicate experimental behavior of a particular material for sufficiently large systems and are of use to researchers investigating phenomena at length scales impractical to study with purely quantum-based models.

The Modified Embedded-Atom Method (MEAM), developed by M. I. Baskes, represents an accurate inter-atomic potential with applications in simulations of many types of

metallic systems. The MEAM is a “modified” version of Daw and Baskes embedded-atom method (EAM), which we introduce in Section 2.4.3. [19][20] The EAM is based on density functional theory and, though a simpler formulation in comparison, can model some basic metallic lattices accurately and with a greater efficiency. The virtue of the MEAM potential however, lies in its account for the directional bonding found in anisotropic lattices, such as Sn's  $\beta$ Sn crystal structure. [21] The potential is able to accurately model phase transitions of Sn, metallic surfaces, and Si-x alloys, just to name a few. [22][23] In the model, the total energy  $E$  is given as a sum of atom energies  $E_i$ , as follows [24][25]:

$$E = \sum_i \left[ F_i(\bar{\rho}_i) + \frac{1}{2} \sum_j \phi(r_{ij}) \right] \quad (2-1)$$

Here,  $F_i$  is the “environment-dependent” embedding function, or the energy required to embed an atom of type  $i$  in to the background electron density  $\rho_i$ . Equation (2-2) illustrates the form of the embedding function, where  $A$  is an adjustable parameter and  $E_{coh}$  is the cohesive energy.

$$F(\bar{\rho}_i) = AE_{coh} \bar{\rho}_i \ln(\bar{\rho}_i) \quad (2-2)$$

In the embedding function, the background electron density is taken as

$$\bar{\rho}_i = \rho_i^0 G(\Gamma) \quad (2-3)$$

where  $\rho^{(0)}$  is the spherically symmetric partial electron density and  $G(\Gamma)$  is represented by equation (2-4) for  $\beta\text{Sn}$ .  $\Gamma$  combines the angular dependent atomic electron densities,  $\rho^{(h)}$ , into one term with equation (2-5).

$$G(\Gamma) = \frac{2}{1 + \exp(-\Gamma)} \quad (2-4)$$

$$\Gamma = \sum_{h=1}^3 t^{(h)} \left[ \frac{\sum_{i \neq j} t_0^{(h)} \bar{\rho}_j^{(0)} S_{ji}}{\sum_{i \neq j} \bar{\rho}_j^{(0)} S_{ji}} \right]^2 \quad (2-5)$$

The average weighting factors ( $t$ 's) are parameters and  $S_{ji}$  is the many-body screening function. The electron densities— $\rho^{(0)}$ ,  $\rho^{(1)}$ ,  $\rho^{(2)}$ , and  $\rho^{(3)}$ , specific for atom  $i$ —are:

$$\bar{\rho}_i^{(0)} = \sum_{j \neq i} \rho^{a(0)} S_{ji} \quad (2-6)$$

$$(\bar{\rho}_i^{(1)})^2 = \sum_{j \neq i} \rho_j^{(0)} S_{ji} \quad (2-7)$$

$$(\bar{\rho}_i^{(2)})^2 = \sum_{\alpha, \beta=1}^3 \left[ \sum_{j \neq i} x_{ij}^\alpha x_{ij}^\beta \rho^{a(2)} S_{ji} \right]^2 - \frac{1}{3} \left[ \sum_{j \neq i} \rho^{a(2)} S_{ji} \right]^2 \quad (2-8)$$

$$(\bar{\rho}_i^{(3)})^2 = \sum_{\alpha, \beta, \gamma=1}^3 \left[ \sum_{j \neq i} x_{ij}^\alpha x_{ij}^\beta x_{ij}^\gamma \rho^{a(3)} S_{ji} \right]^2 \quad (2-9)$$

And  $\rho^{a(1)}$ ,  $\rho^{a(2)}$ , and  $\rho^{a(3)}$  are assumed to decrease exponentially, as

$$\rho^{a(h)}(r_{ij}) = \rho_{i,0} \exp \left[ -\beta^{(h)} \left( \frac{r_{ij}}{r_e} - 1 \right) \right] \quad (2-10)$$

where  $\beta^{(h)}$  and  $\rho_{i,0}$  parameters, and  $r_e$  is the nearest neighbor distance for the material's reference structure, both given in the following table. The scaled coordinates  $x_{ij}$  are

$$x_{ij}^1 = \frac{x_j - x_i}{r_{ij}} \quad x_{ij}^2 = \frac{y_j - y_i}{r_{ij}} \quad x_{ij}^3 = \frac{z_j - z_i}{r_{ij}} \quad (2-11)$$

and  $r_{ij}$  is the distance between atoms  $i$  and  $j$ . The screening function,  $S_{ji}$ , and screening parameters are reported below.

$$S_{ji} = \prod_{k \neq i, j} S_{jki}, \quad S_{jki} = \begin{cases} 0 \\ \left( 1 - \left( \frac{C_{\max} - C}{C_{\max} - C_{\min}} \right)^4 \right)^2 \\ 1 \end{cases} \text{ for } \begin{cases} C \leq C_{\min} \\ C_{\min} \leq C \leq C_{\max} \\ C \geq C_{\max} \end{cases} \quad (2-12)$$

$$C = 1 + 2 \frac{r_{jk}^2 r_{ji}^2 + r_{ki}^2 r_{ji}^2 + r_{ji}^4}{r_{ji}^4 - (r_{jk}^2 - r_{ki}^2)^2} \quad (2-13)$$

where  $k$  is a third atom. The second term in *equation (2-1)*,  $\phi(r_{ij})$ , is the pair interaction between atom  $i$  and its neighbors,  $j$ . It is derived from the universal equation of state,  $E^u$ , by Rose et al., and using equilibrium values (respective table parameters) for the reference structure of the material we get *equation (2-14)* and *equation (2-15)*. [22] The pair potential is evaluated using the embedding function for the material's reference structure. In this case *equation (2-3)* is evaluated using reference structure parameters.

$$\phi(r_{ij}) = \frac{1}{Z_{ij}^0} \{2E_i^u(r_{ij}) - F_i(\bar{\rho}_j) - F_j(\bar{\rho}_i)\} S_{ji} \quad (2-14)$$

$$E_i^u(r_{ij}) = -E_{coh} \left[ 1 + \alpha_i \left( \frac{r_{ij}}{r_{eq}} - 1 \right) \right] \cdot \exp \left[ -\alpha_i \left( \frac{r_{ij}}{r_{eq}} - 1 \right) \right] \quad (2-15)$$

$$\alpha_i^2 = \frac{9\Omega B}{E_{coh}} \quad (2-16)$$

Here,  $B$  is the material's bulk modulus and  $\Omega$  is the volume of the atom. The constants particular to a certain type of atom, or reference structure, are  $E_c$ ,  $A$ ,  $\Omega$ ,  $B$ ,  $r_e$ ,  $t^{(h)}$ ,  $\rho_0$  and  $\beta$ . Sn, Ag, Cu, and the cross-potential parameters are listed in *table 1*. Cross-potential pairwise energy and electron densities for the reference structure (*equation (2-14)*) are computed differently for Sn-X interactions, and are based on the L1<sub>2</sub> crystal structure shown below. [26] The potential was parameterized for Sn, and the Sn-Ag and Sn-Cu systems in refs.[21], [27], [28], respectively.

$$\phi_{X_3Sn} = \frac{1}{3} E_{X_3Sn}^u - \frac{1}{4} F_X(\bar{\rho}_X) - \frac{1}{12} F_{Sn}(\bar{\rho}_{Sn}) - \phi_{XX} \quad (2-17)$$

$$\bar{\rho}_X = \frac{\sqrt{(8\bar{\rho}_X^{(0)} + 4\bar{\rho}_{Sn}^{(0)})^2 + \frac{8}{3} t^{(2)} (\bar{\rho}_X^{(2)} - \bar{\rho}_{Sn}^{(2)})^2}}{12\rho_{X,0}} \quad (2-18)$$

$$\bar{\rho}_{Sn} = \frac{\bar{\rho}_X^{(0)}}{\rho_{Sn,0}} \quad (2-19)$$

**Table 2-1** Parameters for the MEAM potential.

	$E_{\text{coh}}$ (eV)	$r_0$ (Å)	$\alpha$	A	$\beta^{(0)}$	$\beta^{(1)}$	$\beta^{(2)}$	$\beta^{(3)}$	$t^{(1)}$	$t^{(2)}$	$t^{(3)}$	$\rho_0$	$C_{\text{min}}$	$C_{\text{max}}$
<b>Sn</b>	3.08	3.44	6.20	1.0	6.2	6.0	6.0	6.0	4.5	6.5	-0.183	1.0	0.8	2.8
<b>Cu</b>	3.62	2.50	5.106	1.07	3.62	2.2	6.0	2.2	3.14	2.49	2.95	1.0	2.0	2.8
<b>Ag</b>	2.85	2.89	5.89	1.06	4.46	2.2	6.0	2.2	5.54	2.45	1.29	1.0	2.0	2.8
<b>Cu<sub>3</sub>Sn</b>	3.5	2.68	5.38										0.8	2.8
<b>Ag<sub>3</sub>Sn</b>	2.83	2.96	6.07									0.7	0.8	2.8

These parameters are determined by fitting experimental values of a material's bulk modulus, average atomic volume, cohesive energy, and equilibrium nearest-neighbor distance of a reference lattice structure. As reported in ref. [21], the potential for Sn has successfully reproduced experimental values of the heat capacity for Sn's  $\alpha$  and  $\beta$  phases, as well as the phase transition temperature between liquid and  $\beta$ Sn, and  $\beta$  and  $\alpha$  Sn. The reference structure for Sn using the MEAM potential is FCC. The alloy forms of the potential reflect input from experiment as well. Cu-Sn interactions reproduce a theoretical bulk diffusion activation energy of Cu in the c-direction of  $\beta$ Sn lattice that is equivalent to experimental measurements, as well as a vacancy formation energy that is very close to experimental data. [28] Similarly, for Ag-Sn interactions, the atomic volume, bulk modulus, and polycrystalline shear modulus for Ag<sub>3</sub>Sn are reproduced almost exactly. [27]

## 2.1.2 Crystal Lattice Structures

All of our simulations use Sn's  $\beta$ Sn phase, one of the two allotropes of Sn. It is metallic and stable at temperatures above 286K to the melting point of 505K. It adopts a body-centered-tetragonal (b.c.t.) structure, shown in *figure 2-1-TOP*, with experimental lattice constants  $a = 5.831\text{\AA}$  and  $c = 3.182\text{\AA}$ . Using the MEAM potential, the equilibrium lattice constants are  $a = 5.92\text{\AA}$  and  $c = 3.23\text{\AA}$ , preserving the 0.546  $c/a$  ratio observed experimentally. The structure for the lead-free solder alloying elements used in this work is  $L1_2$  for both  $\text{Cu}_3\text{Sn}$  and  $\text{Ag}_3\text{Sn}$ . In our simulations, we do not utilize any of these structures outright, but we report this here because of their use as the MEAM reference structure in Section 2.1.1 for Sn-X interactions. Chapters 5 and 6 employ the MEAM cross-potentials to describe Ag and Cu solute interactions with Sn, and *figure 2-1-BOTTOM* provides a connection to the parameters used to describe these interactions.

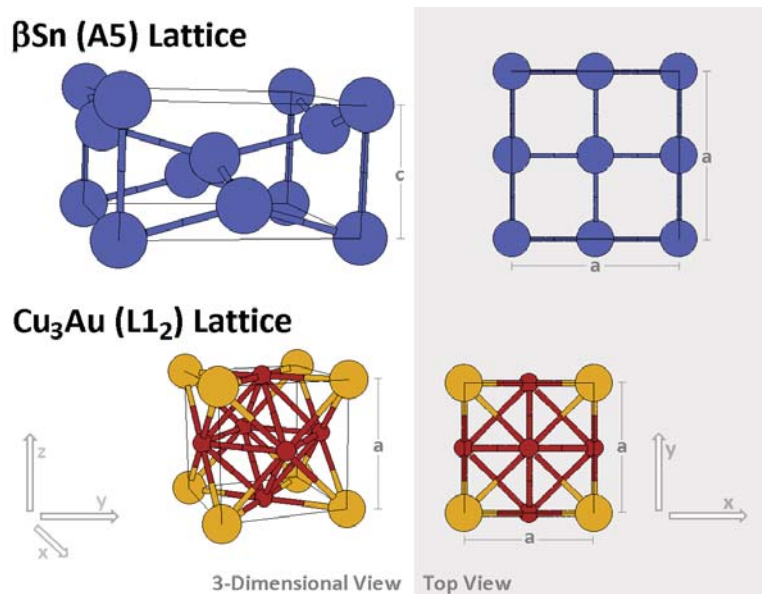


**Figure 2-1** Crystal structures of  $\beta$ Sn (TOP) and its alloys in  $L1_2$  (BOTTOM) represented by the MEAM potential. Dimensions on lattice indicate tetragonal crystal structure (TOP) and cubic crystal structure (BOTTOM). Lattice images courtesy of ref. [29].

### 2.1.3 Constructing Interfaces

In the bulk of this dissertation, we construct various types of symmetric tilt grain boundaries, which can be thought of as twist grain boundaries with  $180^\circ$  rotation. [30]

The specific types of grain boundaries simulated are limited to structures that are of medium to high energy, and whose interface atoms exhibit enough motion at our simulation temperatures to compute an accurate diffusivity using molecular dynamics.

Symmetric tilt grain boundaries that fall under these categories with shared interfacial Miller planes  $(h k l)$  of  $(h01)$  and  $(h10)$  are:  $(101)$ ,  $(201)$ ,  $(401)$ , tilted around  $[010]$ , and  $(310)$ - $\Sigma 5$ , and  $(410)$ , tilted around  $[001]$ , shown in *figure 2-2*. We can also say that the 0 Miller index value of the plane denotes the axis that the two grains are independently rotated around to expose their common Miller plane.

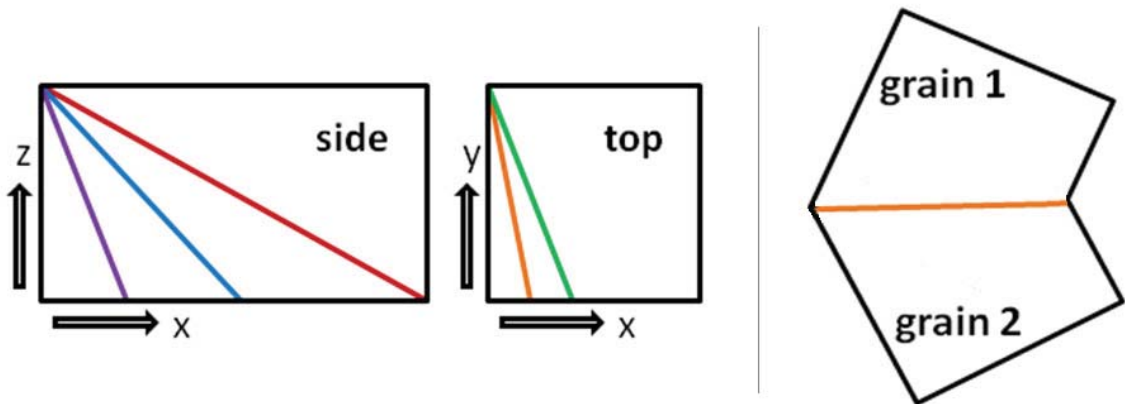


**Figure 2-2** Shown LEFT are various Miller planes in  $\beta$ Sn's lattice. RIGHT is the rotation of two grains to share a common Miller plane. Red, Blue, and Purple, are  $(101)$ ,  $(201)$ , and  $(401)$  Miller planes, respectively. Green and Orange are  $(310)$  and  $(410)$ , respectively. Note that the *side* view x-direction is stretched for figure height conformity. X-direction corresponds to the lattice a-direction,  $[100]$ ; Z-direction corresponds to the lattice c-direction,  $[001]$ .

In general, there are two types of simulation setups. The first involves a fully periodic simulation box, with repeating structural units in the x, y, and z-directions. This particular technique is used in many works, such as ref. [31]. Here one must create two grain boundaries such that the top and bottom of grain 1 creates interfaces with grain 2. This enables periodicity in a direction perpendicular to the grain boundary. The second type removes the periodic nature of the simulation box in the direction perpendicular to the grain boundary, and fixes atoms at the top of grain 1 and at the bottom of grain 2, mimicking a bulk structure and creating a periodic “sandwich”. [30] In this case it is important to equilibrate the system correctly in order to obtain a zero average pressure. For this work we use the latter method, as this system often contains fewer atoms than the fully periodic, dual interface structure. A snapshot from a simulation is shown below.

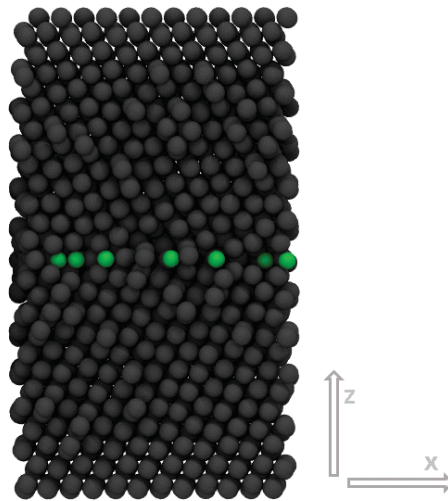


**Figure 2-3** Simulation snapshot of the (101) grain boundary of  $\beta$ Sn. Dark atoms are Sn, green are Ag solute at the interface. Structure is 3-dimensional and view is looking down the y-direction at the x-z plane.

## 2.2 Computing Transport Properties

In Chapters 3, 4, and 5, analysis of our  $\beta\text{Sn}$  systems requires calculation of transport properties of single or multiple atoms in particular structural regimes. Computing during simulations for these type of properties is often tricky in inhomogeneous systems, so the various methods used in subsequent chapters are outlined in the following subsections.

### 2.2.1 Mechanism Search with the Dimer Method

From a molecular dynamics point of view, diffusion in solids is considered a rare event. An atom moving along a surface, in a grain boundary, or through a bulk lattice typically takes many orders of magnitude longer than the time scale of the atomic vibrations, which determines the time step for classical molecular dynamics (MD). Simulations using MD can run for days, or longer, before a significant diffusion event might occur. This inefficiency in direct rare event simulation has been overcome with methods developed to bridge the two timescales of vibrations and diffusive movement. One popular technique is the Nudged Elastic Band (NEB) method, where once an initial and final state of the system are known, the energy of the path a system can take from initial state to final state is minimized to determine the likely mechanism. [32] Transition Path Sampling (TPS) can also locate likely mechanisms of a state A to state B process by generating an ensemble of dynamic paths from an initial state A-to-state B path. [33] A third technique developed by Henkelman, called the Dimer Method, can locate saddle points (typically a maximum in energy along the path) on the hyper-surface defined by the model's potential energy function, starting only from a minimum energy configuration. [34]

While robust in their ability to handle many types of systems, NEB and TPS require the known locations of initial and final states of a system. For this work, we desire a method with the ability to seek out final states and associated saddle points that are perhaps unanticipated. As such, the Dimer method is used in our present study to examine the mechanisms of a diffusing adatom. Henkelman's Dimer method is a potential energy surface walker used to locate saddle point and minimum-energy configurations of a system of atoms. It has successfully been used to predict single- and concerted-adatom movement on Cu and Al surfaces and shown to reduce the number of force calculations necessary in saddle point searches, when compared to eigenvector following methods. [35] We apply this method in our surface diffusion study by piecing together parts of a mechanism that a group of atoms might undergo—moving from some *minimum energy state a*, through a *high energy saddle point*, to *minimum energy state b*. A diffusion mechanism mapped to a potential energy hyper-surface is shown in *figure 2-4-1*.

Each point on this surface in *figure 2-4* represents a specific configuration of atoms. Our system of study, an adatom (red) sitting in a pocket of surface atoms, is shown in *figure 2-4-2*. We can create two replicas of our system and slightly displace the atoms in each replica, yielding *three* unique points on the hyper-surface, each with different energies and collective atomic positions. With this, a “dimer” on the potential energy hyper surface is created, shown in *figure 2-4-3*. If the replica distance in surface-space is maintained, information from the middle and each end of the dimer, such as total energy of each system and the gradient of the energy, provides an estimate for the curvature of the hyper-surface. We can then move the dimer in a direction opposite to the collective

force vectors of the atoms. This leads to a saddle point: a location with one negative mode of curvature and corresponding to a peak in the energy of a diffusion mechanism.

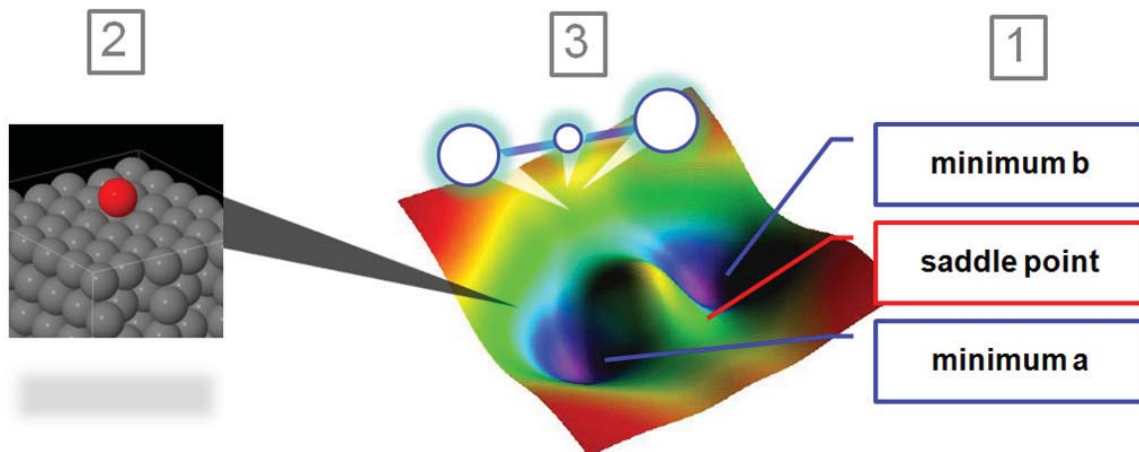


**Figure 2-4** (1) Typical locations on the energy hyper-surface for minima and saddle points. (2) An atomistic system represented by a point on the energy hyper-surface. (3) Multiple points (systems) with their distance in hyper-surface space maintained. Colored hyper surface adapted from ref [33].

As the dimer is stepped from a low energy region up to a saddle point, it is “rotated” in  $3N$  space (where  $N$  is the number of atoms) around its center system to minimize the total energy of the dimer. This ensures that the dimer is following a mode of curvature that leads to a saddle point, and not climbing up some direction of infinitely increasing energy. This minimization in the rotation sub-step is carried out in this work by the steepest descent method. A saddle point is found when the gradient of the energy on the center of the dimer is zero and there is one negative mode of curvature for that system. In this configuration, the dimer can be said to be straddling the saddle point. In Chapter 3, we present our parameters used in the dimer searches, such as dimer length, number of rotations per step, and saddle point force tolerance.

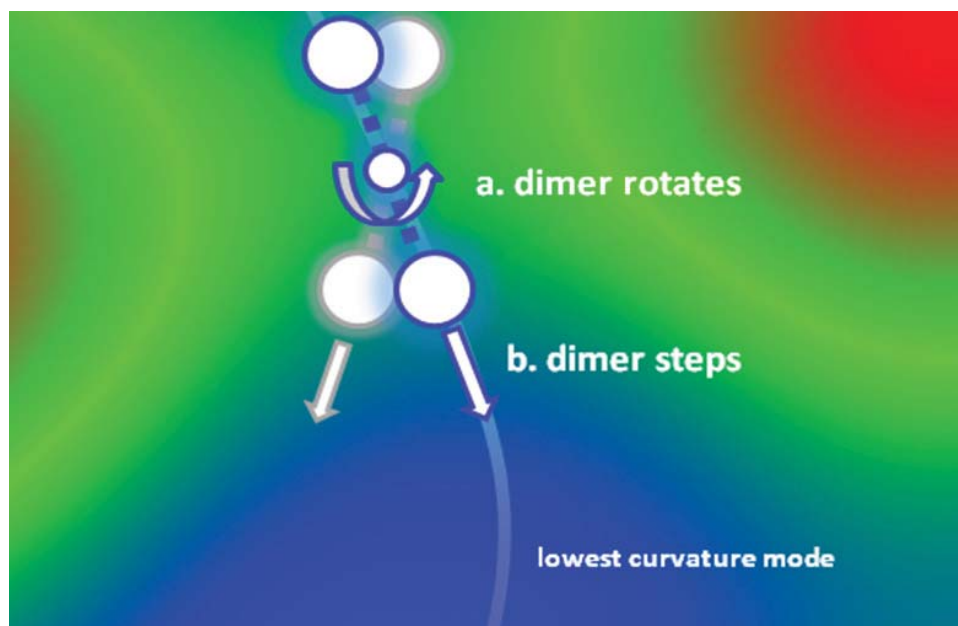


**Figure 2-5** When tracing the path of minimum energy from the saddle point to minimum, the dimer is rotated to a minimum energy via steepest descent (a) and then stepped (b), maintaining the correct orientation along the lowest curvature mode. This routine is repeated until the center of the dimer is at a minimum energy.

According to Henkelman, from a saddle point configuration we can find the minimum energy path of a given mechanism using a method similar to the dimer search. We minimize the rotational energy at each step “down” the potential energy surface with a full steepest descent minimization of the rotational energy of the dimer. This is sufficient to keep the dimer on the path of the minimum mode and lessens the number of full force calculations required for minimization. When the energy of the “front” system (end with lower energy) of the dimer is greater than the energy of the center system, it has reached a minimum energy configuration.

As a result of the dimer search and subsequent minimization routine, the configurations and energies of the initial state minimum, saddle point, and corresponding final state

minimum are known (*figure 2-4*). In the next section, we will outline how this information for a particular mechanism is used to compute a rate and/or a diffusivity.

### 2.2.2 Diffusivity from Harmonic Transition State Theory

For solid systems, the harmonic form of TST is a good approximation to full TST for computations of rate constants, shown below. [36] In this formula  $\nu_i$  are the vibrational normal mode frequencies at the minimum and saddle point configurations for a given mechanism (indicated “init” and “\*”, respectively),  $N$  is the number of atoms,  $E$  is the energy of the system at the minimum and saddle configurations,  $k_B$  is Boltzmann’s constant, and  $T$  is temperature.

$$k^{hTST} = \frac{\prod_i^{3N} \nu_i^{init}}{\prod_i^{3N-1} \nu_i^*} e^{-(E^* - E^{init})/k_B T} \quad (2-20)$$

We can extend hTST to describe the diffusivity of a hopping adatom by computing first the pre-exponential factor of the Arrhenius form. A review by Gomer provides a relationship for computing this factor, as do Ratsch and Scheffler. [37][38] This is shown in *equation (2-21)*. By computing the distance the adatom has traveled from minimum A to minimum B and computing its attempt frequency, shown in *equation (2-22)*, the pre-exponential factor is found.

$$D_0 = \frac{\Gamma l^2}{2\alpha} \quad (2-21)$$

$$\Gamma = \frac{\prod_i^{3N} v_i^{init}}{\prod_i^{3N-1} v_i^*} \quad (2-22)$$

Here,  $\Gamma$  is the attempt frequency (also the non-exponential factor from *equation (2-20)*) and  $v_i$  are the normal modes at the minimum (*init*) and saddle point (\*) for an N atom system,  $l$  is the distance traveled by the adatom, and  $\alpha$  is the dimensionality of the lattice ( $\alpha=2$  for a square lattice, 1 for a specific diffusion direction x or y or z). From our dimer searches, we can find  $E_A$ , the difference in energies of the saddle and minimum configurations, and using the relation for  $D_0$ , we can compute the diffusivity  $D^*$  for a particular mechanism, expecting a simple Arrhenius relationship, as in *equation(2-23)*.

$$D^* = D_0 e^{-E_A/kT} \quad (2-23)$$

In addition to the dimer method in Section 2.2.1, the relationships from this section are used in Chapter 3 to investigate various single and multi-atom mechanisms available to a diffusing Sn adatom on a low energy  $\beta$ Sn surface.

### 2.2.3 Diffusivity Computation Techniques with Molecular Dynamics

Self-diffusion of particles in an MD simulation is typically computed via the Einstein or Green-Kubo relations, which involve tracking atomic displacements or velocities. [39] Here, we follow the work of Keblinski et al., wherein diffusion is measured with an adjusted form of the Einstein relation. [40] This adjustment is performed because in a particular MD run, atoms close to the grain boundary will exhibit a variety of displacement lengths. As one moves away in a direction perpendicular to the interface

(z-direction, in our case) and into the defect-free bulk lattice, displacement begins to decrease to the order of atomic vibrations. Averaging the squared displacement over *all* atoms, as is normally done in a structurally homogeneous system, will wash out the true value of solvent self-diffusivity in the grain boundary. One could specify a region of the simulation box, within which the mean squared displacement would be calculated, but the dividing surface between fast and non-existent diffusivity regions for our systems is not known *a priori*. As a result, we compute the total squared displacement in our system and normalize this quantity by atomic volume per grain boundary area, shown in *equation (2-24)*.

$$\delta_{GB}D_{GB} = \frac{\Omega N_A}{A} \cdot \frac{1}{4} \frac{dMSD}{dt} \quad (2-24)$$

Here,  $\Omega$  is the volume per Sn atom in our system,  $N_A$  is the number of atoms used to compute the mean squared displacement,  $A$  is the interfacial area, and the factor of 1/4 is determined by the dimensionality of the mean squared displacement (MSD). After this scaling, the quantity computed is likened to the interface width  $\delta_{GB}$  perpendicular to the plane of  $A$ , multiplied by the true grain boundary diffusivity,  $D_{GB}$ . Now,  $\delta_{GB}$  may be represented as shown in *equation (2-25)*, where  $N_D$  is the number of diffusing atoms.

$$\delta_{GB} = \frac{N_D \Omega}{A} \quad (2-25)$$

During a particular simulation run, like those in Chapters 4 and 6, the total squared displacement ( $N_A \times MSD$ ) is calculated and with *equation (2-24)* yields the quantity

$\delta_{GB}D_{GB}$ . To finally resolve a value of  $D_{GB}$  for each system, we must determine  $\delta_{GB}$ , the width of the interface, by means other than *equation (2-25)*.

$\delta_{GB}$  is evaluated post-MD run by examining the diffusive profiles of each  $\beta$ Sn grain boundary, and computing its value from these profiles via a *full-width at half maximum* analysis. The diffusive profiles are measured in addition to the simulation cell's total diffusivity outlined above. For a particular simulation run, we compute planar quantities of the diffusivity ( $D_{xy}$ ) in directions parallel to the grain boundary interface, calculated using a typical Einstein relation for atoms in a plane. We restrict the volume of space in which *MSD* is sampled to slices in successive z-planes of width  $\Delta z$ , and  $D_{xy}$  is evaluated as the slope of this quantity versus time. An example of this method is shown in *figure 2-6*. The background of this figure is a grain boundary, rotated from a typical viewing angle so that the simulation cell's z-axis is parallel to the z-positions on the plot. Here, we see that planes in the z-direction close to the interface are areas of high diffusivity. The *full-width at half maximum* of such profiles are used to quantify an interface width, as indicated in the figure. In addition to the width, and as shown in Chapter 5, the shape of these profiles are useful in comparing and contrasting the effects of solutes studied in this work.

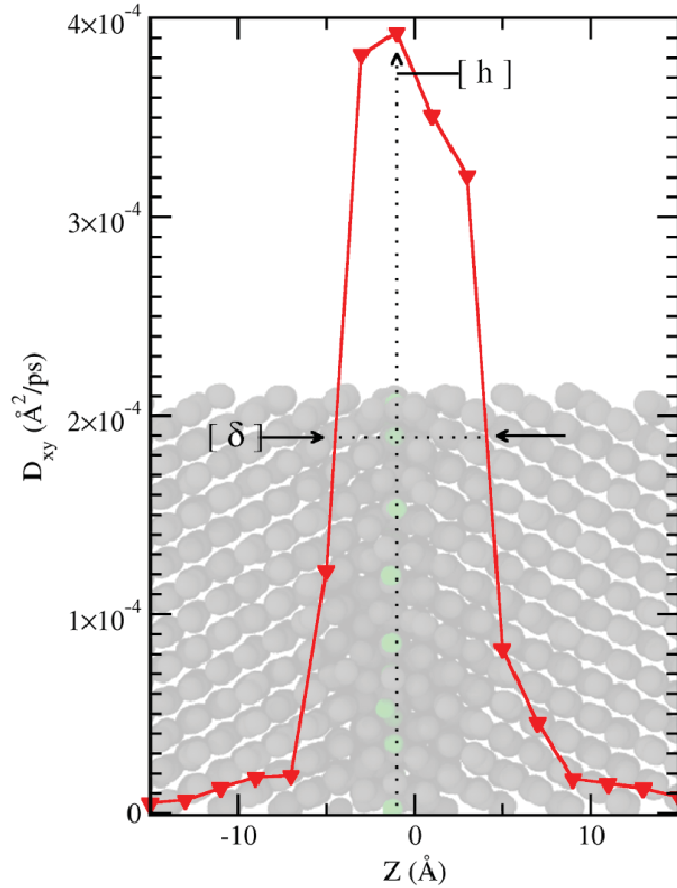


**Figure 2-6** Planar diffusivity vs. z-coordinate in the simulation cell.  $[h]$  is the maximum of the diffusion profile and  $[\delta]$  is the width at  $[h]/2$ . Background is grain boundary rotated with z-axis parallel to planar diffusivity plot abscissa. Points on plot correspond to lattice planes in background separated by  $\Delta z$ .

In the literature, a variety of measures of the interface structure and atomic mobility are utilized to investigate interface width. [31][40][41][42] The use of a potential energy profile per plane, as well as the square of the planar structure factor, has been used to determine  $\delta_{GB}$ . [31][40] For our work, the diffusive width provides information about how the grain boundary interfaces evolve with increasing solute and simulation temperature, and we use the diffusive width in the calculation of  $D_{GB}$  given the quantity  $\delta_{GB}D_{GB}$  computed in simulation. Values of  $\delta_{GB}$  calculated from a planar diffusion

computations are more closely related to the total squared displacement we are computing in simulation. As such, we believe the most meaningful grain boundary diffusivity,  $D_{GB}$ , is computed using the width computations from diffusive profiles.

## 2.3 Energetics and Structure of Surfaces and Interfaces

In the comparison of similar atomic structures, or in the analysis of perturbations on a particular structure, it is handy to characterize them with a single parameter. Often times this is the difference in potential energy when compared to the homogeneous bulk structure of the same material. This “excess” potential energy offers either an extensive or intensive (when scaled by volume or area, for example) quantity, relatable to various types of structures on a single thermodynamic scale. While the excess potential energy does not completely describe the structures in a thermodynamic sense (one would need the free energy, through calculation of entropic contributions or various simulation techniques), it provides a substantive metric for the systems investigated in this body of work.

Additionally, a quantity purely describing the atomic structure is used to further characterize the interfaces found in subsequent chapters. This is another useful measure, offering a way to capture changes in a structure, when compared to the bulk system, that may not be described through the excess potential energy.

### 2.3.1 Excess Potential Energies of Surfaces and Interfaces

The excess potential energy  $\gamma_{SURF}$  of a free surface system is calculated through a simple relation given as *equation (2-26)* and illustrated in *figure 2-7*.

$$\gamma_{SURF} = \frac{E_{SLAB} - (N_{ATOMS} \cdot E_{BULK,ATOM})}{2A} \quad (2-26)$$

To accomplish computing only the excess energy of the actual surface in our simulation, we need information from two types of systems. First, we calculate the total energy  $E_{SLAB}$  of a dual surface slab system, with desired Miller planes exposed and periodic in both directions parallel to the plane of the interface. Next, the energy of a bulk system with the same number of atoms as the dual slab system is computed, given by  $N_{ATOMS} \times E_{BULK,ATOM}$ , where  $E_{BULK,ATOM}$  is the average energy per atom in a fully periodic simulation. These two quantities are subtracted to give the excess potential energy of both surfaces in the dual surface slab system. Finally, the difference is divided by two to get a single excess potential energy value, and scaled by the area of the dual surface slab system.

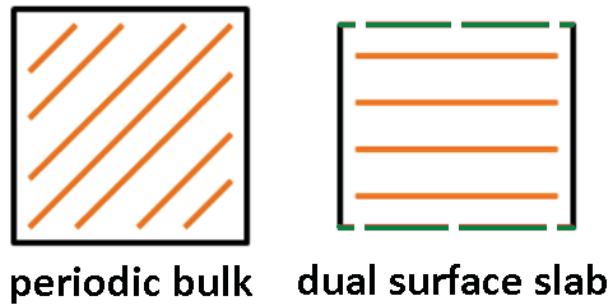


**Figure 2-7** The two systems considered in excess potential energy calculations of a free surface. Orange lines are Miller planes; Green dashed lines are fixed free surfaces.

Computation of the excess potential energy for a grain boundary is equally as straightforward. Because of our system setup outlined in Section 2.1.3, we add a 3<sup>rd</sup> intermediary structure to remove the effect of the two free surfaces at the top and bottom

of the simulation cell. This is shown in *figure 2-8*. From here we can obtain a measure of the excess potential energy of the grain boundary interface only.



**Figure 2-8** The three systems considered in excess potential energy calculations of a grain boundary. Orange lines are Miller planes; Green dashed lines are fixed free surfaces.

Shown in *equation (2-27)* and used in several works is the excess grain boundary potential energy  $\gamma_{GB}$ , where  $E_{GB}$  is the potential energy of the grain boundary structure,  $E_{SLAB}$  is the energy of the tilted slab structure, and the quantity  $N_{X,ATOMS} \times E_{BULK,ATOM}$  is the energy of a periodic bulk structure with the same number of atoms as the slab or grain boundary. [41][42] Finally,  $\gamma_{GB}$  is scaled by the interface area  $A$ . We note that *equation (2-27)* can be simplified, but is left in expanded form for clarity. Starting with the potential energy of the grain boundary system, we remove the energy increase due to the upper and lower free surfaces (2<sup>nd</sup> term of the numerator) and then compare the remaining energy to that of a fully periodic structure of the same number of atoms (3<sup>rd</sup> term).

$$\gamma_{GB} = \frac{E_{GB} - (E_{SLAB} - N_{SLAB,ATOMS} \cdot E_{BULK,ATOM}) - (N_{GB,ATOMS} \cdot E_{BULK,ATOM})}{A} \quad (2-27)$$

### 2.3.2 Solute Contributions to Interfacial Energy

In this sub-section, we present background on the theory of solute segregation at interfaces and in nanocrystalline materials. We also outline the specific relations between solute concentration and grain boundary energy employed in this work.

When a solute atom segregates to a interface, the Gibbs adsorption equation describes the relationship between the change of free energy of the interface ( $\gamma$ ), the concentration of solute at the interface ( $\Gamma_A$ ), and the chemical potential of the solute ( $\mu_A$ ), shown in *equation (2-28)*. [43] This shows that the free energy, for a positive excess solute amount and increasing chemical potential, will be reduced.

$$d\gamma = -\Gamma_A d\mu_A \quad (2-28)$$

At equilibrium, the concentrations of solute in the bulk grain and at a grain boundary interface can be represented well by the Langmuir-McLean adsorption isotherm. [44] *Equation (2-29)* gives the relationship between the amount of solute in the grain boundary  $N_{A,GB}$ , the number of total atomic sites in the boundary  $N_{GB}$ , the amount of solute in the bulk matrix  $N_{A,M}$ , and the number of atomic sites in the bulk matrix  $N_M$ , based on McLean's model.

$$\frac{N_A^{GB}}{N^{GB} - N_A^{GB}} = \frac{N_A^M}{N^M} \exp\left(\frac{\Delta H_{A,M}^{SOL} - \Delta H_{A,GB}^{SOL}}{RT}\right) \quad (2-29)$$

Here,  $\Delta H_{A,M,SOL}$  is the enthalpy of solution for the solute in the bulk matrix and  $\Delta H_{A,GB,SOL}$  is the enthalpy of solution for the solute in the grain boundary. Weissmuller extends these models to write the total free energy of a grain boundary or polycrystalline structure as [45]

$$\gamma = \gamma_0 - \Gamma_A \left( RT \ln x_L + \Delta H_A^{SEG} \right) \quad (2-30)$$

In *equation (2-30)*, the energy is now the difference between the free energy of the pure grain boundary or polycrystal ( $\gamma_0$ , and  $\Gamma_A=0$ ), and the effect of the solute on boundary configurational entropy and enthalpy terms.  $x_L$  is the solute fraction in the lattice and  $\Delta H_{A,SEG} = \Delta H_{A,M,SOL} - \Delta H_{A,GB,SOL}$ , the enthalpy of segregation. Neglecting entropic effects and at a constant pressure, similar to refs.[46], [47], and [48], we can use *equation (2-30)* to calculate the decrease in potential energy of our system, upon the addition of solute at the interface. *Equation (2-30)* is simplified below and the notation is made consistent for use in later sections of this work.

$$H_{GB+S}^{EX} = H_{GB,0}^{EX} - \Gamma^{EX} \left( \Delta H_A^{SEG} \right) \quad (2-31)$$

For the excess energy of a grain boundary containing solute  $H_{EX,GB+S}$ , the calculation is slightly different than in Section 2.3.1. Now, the energy difference is between a grain boundary containing a given amount of solute, and a periodic bulk structure containing the same amount of solute. Since it is difficult to follow the above procedure with solute atoms included, we outline a few additional steps to compute  $H_{EX,GB+S}$ . First we obtain the energy of only the solute atoms in the bulk structure, by subtracting the energy of a

pure periodic bulk structure from a periodic bulk containing solute atoms. We then subtract the energy of these solute atoms from the grain boundary with solute structure. From here, we can use *equation (2-27)*, where  $E_{GB}$  is now  $H_{GB+S}$ , to find  $\gamma_{GB}$ , now  $H_{EX,GB+S}$ .

### 2.3.3 Identifying Regions of Structure in Grain Boundaries

In addition to potential energy, we can characterize interfaces purely through the differences in their atomic positions when compared to the bulk. By computing the square of the structure factor in a per plane basis and plotting this versus the z-axis coordinate, similar to Section 2.2.3, a value between zero and unity is given for sequential planes throughout the grain boundary. [31] Shown in *equation (2-32)* is the relation for the squared structure factor,  $|S(k)|^2$ .

$$|S(\vec{k})|^2 = \frac{1}{N^2} \left[ \left( \sum_{i=1}^N \cos(\vec{k} \cdot \vec{r}_i) \right)^2 + \left( \sum_{i=1}^N \sin(\vec{k} \cdot \vec{r}_i) \right)^2 \right] \quad (2-32)$$

In this case,  $k$  is a wave vector that describes the periodicity of the perfect lattice in a particular direction,  $r$  is the position of the atom contained in the plane, and  $N$  is the number of atoms in the plane. Depending on the current structure's deviation from the perfect lattice, the quantity  $|S(k)|^2$  can range from 1 (identical structure to the wave vector) to 0 (no structure with respect to the wave vector). This provides a good measure of any structural transitions that develop at or around the grain boundary interface. Shown in *figure 2-9* are plots of the squared structure factor for sequential (201) Miller planes in a bulk structure at 0K, at 300K, and a (201) grain boundary at 300K. Here the

system is rotated so the normal vector of the (201) plane is perpendicular to the z-axis of the simulation cell.

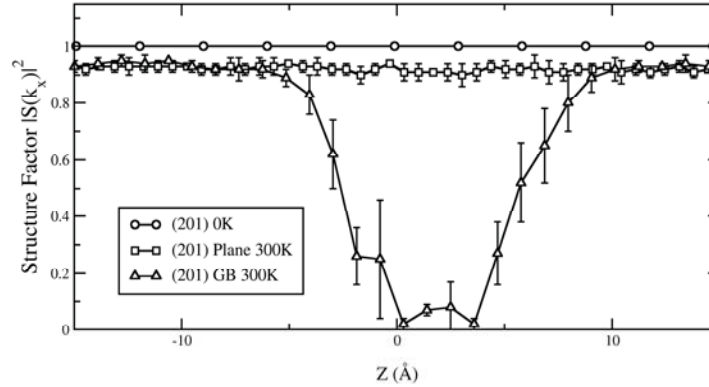


**Figure 2-9** The variation of  $|S(k)|^2$ , for a bulk solid at 0K and 300K, and a grain boundary at 300K. Note the abscissa is the direction perpendicular to the interface. Error bars represent the standard deviation of  $|S(k)|^2$  in five snapshots of an MD run.

## 2.4 Atomic Level Stress: An Introduction and Case Study

### 2.4.1 Macroscale Connection to Atomic Stress

In a work published in 1976, Blech showed that the atomic vacancy flux process creates a stress gradient during electromigration. [49] When this stress gradient is large enough, the electromigration process cannot happen in metals if the cathode and anode are within a certain maximum distance. This stress-vacancy relationship is referred to as *Blech's critical length*. In 1993, Kirchheim proposed a model that reached to the microscopic level, describing the generation of tensile and compressive stresses in aluminum lines. [2] He used the instances of atomic vacancy generation, annihilation, and transport to account for these electromigration induced stresses. In 1999, Gleixner and Nix proposed

another model for electromigration and stress-induced void formation in aluminum VLSI interconnects based on classical nucleation theory. [50] In that work they provide a discussion of an upper limit for hydrostatic tensile stresses in such lines based on an assumed volumetric lattice strain value. Kirchheim's model has been expanded by Sarychev, *et al.* and Bassman. [14][51] Sarychev et al. state that the main disadvantage of Kirchheim's approach is the neglect of vacancy flux in the stress evolution of the system. Their model offers a method for connecting the evolution of the stress tensor with the transport of vacancies, the geometry of the metallization, and the stress and displacement boundary conditions that apply to it. In a dissertation by Bassman, a thermodynamic formalism for both the vacancy contribution to stress and chemical potential gradients was developed. Her work investigates stress-mediated self-diffusion in polycrystalline solids. In all three models, the size of an aluminum atomic vacancy is characterized by the strain that the volume of an atom would undergo upon its removal from a perfect lattice.

#### 2.4.2 Relationships for Volumetric Strain

The change in volume describing a vacancy is related to the original atomic volume by the parameter  $f$ , called the vacancy relaxation factor. The form of Sarychev's relation is shown below in *equation (2-33)*.

$$\varepsilon_v = -f \cdot \Omega < 0 \tag{2-33}$$

$\varepsilon_v$  is the strain deformation introduced by vacancy volume relaxation.  $f$  is the vacancy relaxation factor which is a dimensionless number, and  $\Omega$  is the volume of an atom.

However, apparent dimensional inconsistency is observed in *equation (2-33)*. Sarychev's notation will be abandoned in our context, which will be more reasonably described by Kirchheim's form who defined  $f$  as the volumetric strain induced by replacing a matrix atom with a vacancy. Following Kirchheim's definition, the volume change induced by generation/ annihilation of a vacancy can be expressed by

$$V_f = (1 - f) \cdot \Omega < 0 \quad (2-34)$$

*Equation (2-34)* assumes that vacancy behaves like a foreign atom with smaller volume,  $(1-f)\Omega$ , than that of a matrix atom.

Very early analytical work investigating the value of  $f$  was conducted by Doyama and Cotterill. [52] Their work calculated the volume of a vacancy by computing the change in positions of copper atoms in a crystal. A pairwise Morse potential described atomic interactions nearest to the point defect, treating the atoms as discrete particles. Further away, atoms were susceptible to treatment by the elastic theory. Doyama and Cotterill found the volume of a copper vacancy to be  $0.83 \cdot \Omega$ , where  $\Omega$  is the atomic volume. Gleixner and Nix, in their work mentioned earlier, and Shewmon, report that for FCC metals, the vacancy volume is  $0.9 \cdot \Omega$ . [53]

Our work attempts to provide a more accurate representation of this relaxation factor, both in atomic scale and in continuum mechanics scale. By comparing results from methods applicable in different length domains, constitutive values are sought for multiscale material modeling. The interactions between aluminum atoms in our

simulation are characterized by Daw and Baskes' Embedded-Atom Method. [19][20] This method serves as a desirable alternative to simpler, pair-wise approaches because of the method's realistic description of metallic cohesion, and is discussed in a comprehensive review and detailed in other papers. A brief summary of the method, based on these works, is presented here.

### 2.4.3 Embedded-Atom Method

Daw, Foiles, and Baskes proposed that the major contribution to the energetics of a metal is the energy to embed an atom into the electron density of neighboring atoms. The remaining energy is explained by a short-range, doubly screened pair interaction that accounts for core-core repulsions. This forms the basis for the Embedded-Atom Method (EAM) description of the system's energy. The potential uses a spherically symmetric electron density, while the Modified Embedded-Atom Method (MEAM), outlined in Section 2.1.1, includes angular dependent terms. EAM is the foundation for MEAM, and consequently the total energy of the system is written in a similar form as

$$E_{total} = \sum_i F_i(\rho_{h,i}) + \frac{1}{2} \sum_{i,j(i \neq j)} \phi_{ij}(R_{ij}) \quad (2-35)$$

Here,  $F_i$  is the embedding energy for placing an atom in a host electron density. That density is described by  $\rho_{h,i}$  which is the total electron density at atom  $i$ , due to the rest of the atoms in the system. We can simplify the description of  $\rho_{h,i}$  by assuming that the host density is closely approximated by a sum of the atomic densities,  $\rho_{a,j}$  of the neighbors  $j$  of atom  $i$ .

$$\rho_{h,i} = \sum_{i \neq j} \rho_j^a(R_{ij}) \quad (2-36)$$

These atomic densities are, as shown in *equation (2-36)*, merely functions of position and provide straightforward calculation of the embedding energy of the atom in question.

The embedding function,  $F_i$ , maintains its simplicity when calculating an atom in an alloy versus a pure material, as it does not depend on the source of the electron density, but only on atom  $i$ .

The second term in *equation (2-35)*,  $\phi_{ij}$  represents the pair interaction and is purely repulsive. Both the embedding function and pair interaction terms are derived on a per material basis, calculated from the formal definitions within the author's density-functional framework, as well as fitting them to describe the bulk equilibrium solid's properties—specifically, the equilibrium lattice constant, heat of sublimation, elastic constants, vacancy formation energy, and BCC-FCC energy difference. The specific potential file for aluminum used with the EAM was developed by Mishin and Farkas, et al. in 1999. Compared to other aluminum potential files for EAM, this accurately reproduces basic equilibrium properties of aluminum derived from both *ab initio* and experimental data, as well as the correct relative stability of different alternative structures with coordination numbers ranging from 12 to 4. This latter feature is particularly desirable for this study.

#### 2.4.4 Virial Stress

The virial definition of atomic stress is used to calculate the stress around a given volume of simulation space.

$$\sigma_{\alpha,\beta} = -\frac{1}{V} \left[ \sum_i r_i^\alpha F_i^\beta + \sum_i m v_i^\alpha v_i^\beta \right] \quad (2-37)$$

Where,  $F_i$  is the force on an atom  $i$  by its neighbors in the  $\beta$  direction, multiplied by the components of the position of  $i$  in the  $\alpha$  direction. The second term represents the ideal gas contribution of the internal pressure of the system (found instantaneously by the kinetic energy). Where  $m$  is the mass of atom  $i$ , and  $v$  is the particular component of its velocity in directions  $\alpha$  and  $\beta$ .  $V$  is the volume containing the atoms  $i$  included in the equation. *Equation (2-38)* shows an expanded view of the symmetric stress tensor, where  $\tau$  is also used to describe a system under shear.

$$\sigma_{\alpha,\beta} = \begin{pmatrix} \sigma_{xx} & \tau_{xy} & \tau_{xz} \\ & \sigma_{yy} & \tau_{yz} \\ & & \sigma_{zz} \end{pmatrix} \quad (2-38)$$

There have been several researchers who question point-wise stress calculation in a system using the expression for atomic stress taken from the virial theorem. Zimmerman et al. show that an expression for continuum mechanical stress in atomistic systems, derived by Hardy converges quicker than the virial to values expected from continuum theory, as a function of volume. [54][55] Zhou argues that neither the virial stress, which includes total atomic velocities, nor Hardy's stress, which includes velocity fluctuations,

represent a measure of the true mechanical stress. [56] We present our results calculated from the virial form of the stress, as this was more convenient to implement and is used extensively in countless other works.

#### 2.4.5 Molecular Dynamics Simulation of Lattice Vacancy

For the aluminum simulations, the LAMMPS molecular dynamics simulation software package was used. [57][58] Data collection runs were conducted using a constant number of particles, constant volume, and at a constant temperature (NVT) for pure aluminum in an FCC lattice at 533K. These conditions are the same as in Sarychev's work, see *table 2-2*. A simulation box size of 6 x 6 x 6 lattice lengths with periodic boundary conditions was used and an initial FCC lattice unit cell length was set at 4.032 angstroms. The system was first equilibrated with an NPT style integrator to allow the lattice (volume) to expand to its zero pressure value at 533K. Next, the system was switched to an NVT integrator for data collection. Simulations were controlled with a Nose-Hoover thermostat and integrated with time steps of 0.001 picoseconds.

**Table 2-2** Al material properties used in simulations, after Sarychev. [14]

<b>E</b>	Young's modulus, (111) texture	$6.6 \times 10^4$ MPa at (533K)
<b>G</b>	Shear modulus	59.3 GPa
<b><math>\Omega</math></b>	Volume per Al atom, bulk	$1.38 \times 10^{-23}$ cm <sup>3</sup>
<b><i>f</i></b>	Vacancy relaxation factor	~0.60

The system was first allowed to converge to equilibrium, which we simulated for 40 picoseconds (ps). Following achieving a convergence, atomic positions and point-wise

stresses were collected every 0.5ps for duration of 10.0ps under NVT conditions. Next, a void was created by removing an atom from the lattice. Data collection continued for 10.0ps. Atom specific positions and stresses were collected for the original atom's 12 nearest-neighbors before and after atom removal.

#### 2.4.6 Computing the Volumetric Strain from Simulation

The volumetric strain created after the removal of an atom is found by direct measurement of first-nearest neighbor positions. Prior to the vacancy formation, distances between each first-nearest neighbor and the atom to be removed were recorded every 0.5ps (500 time steps), for 10.0ps ( $10^3$  time steps). Averaging the first-nearest neighbor positions, we can find the center of the void, and from there an average neighbor distance from the void,  $R_1$ , is found. Next, the atom is removed and the system is allowed to converge to an equilibrium which took about 500 time steps. Similar to before, distances between each first-nearest neighbor and the center of the void are recorded every 500 time steps, for  $10^3$  time steps. A second average neighbor distance,  $R_2$ , is found. Spherical volumes based on these two radii are computed and the volumetric strain is computed as shown below.

$$\varepsilon_v = \frac{\Omega_1 - \Omega_2}{\Omega_1} = \frac{(R_1)^3 - (R_2)^3}{(R_1)^3} \quad (2-39)$$

The average initial ( $R_1$ ) and final ( $R_2$ ) distances to the atom or void center for one particular molecular dynamics run are shown in *figure 2-10*. Dotted lines of ( $R_1$ ) and ( $R_2$ ) values are averages over multiple simulation runs, with statistical uncertainty shown in the legend. From our first-nearest neighbor distance, and using *equation (2-33)* we

obtain that  $f_1 = 0.060 \pm 0.013$ . The error found here is based on uncertainty in ( $R_1$ ) and ( $R_2$ ), propagated through *equation (2-39)*. The values reported by authors doing similar research are listed in *table 2-3*.

**Table 2-3** Vacancy relaxation factors as reported by authors.

<b>Sarychev, <i>et al.</i></b>	0.60
<b>Bassman</b>	0.20
<b>Doyama, <i>et al.</i></b>	0.17
<b>Gleixner and Nix</b>	0.10
<b>This work</b>	0.060

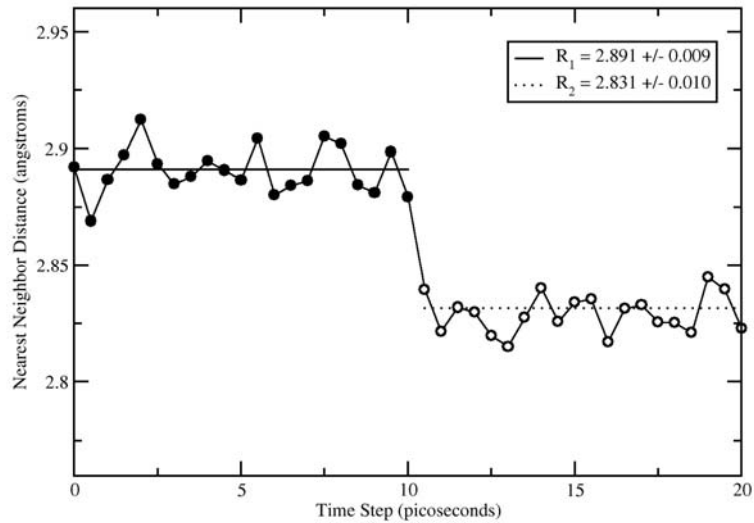


**Figure 2-10** A plot of first-nearest neighbor distance from center of an atom (or void), versus simulation time steps in molecular dynamic simulations. Filled black circles indicated a full lattice and open circles indicate a vacancy, where the atom is removed at 10ps into the data collection run. Average neighbor positions before and after atom removal are  $2.891 \pm 0.009$  and  $2.831 \pm 0.010$ , respectively.

### 2.4.7 Validation with Continuum Mechanics Methods

In this section, continuum mechanics formulations are introduced to calculate the spherical stress induced by the removal of a matrix atom. The location of the missing atom is simplified as a spherical cavity inside an infinite elastic body. The interactions between atoms, including short range repulsion and long distance attraction, are the source of the stresses in continuum level. After the sudden removal of an atom, the attraction can no longer be balanced by the repulsion. Hence the atoms nearby will sink into the void until they reach another balance. This is the mechanism of shrinkage strain at the missing atom site. In this method, the atoms interactions are treated as hydrostatic pressure around the cavity. By introducing the elastic constitutive relationship, the volumetric stress can be calculated, which is shown in *figure 2-11*.

$$P = \frac{1}{3} \times \begin{bmatrix} \sigma_r & & \\ & \sigma_\theta & \\ & & \sigma_\phi \end{bmatrix} \quad (2-40)$$

Shown in *figure 2-12* is a free body diagram of our sphere under stress. Further analysis of these stresses show that at the inner boundary of the cavity, we have

$$\sigma_r = 0 \quad (2-41)$$

$$\sigma_\theta = \sigma_\phi = \frac{3}{2}P \quad (2-42)$$

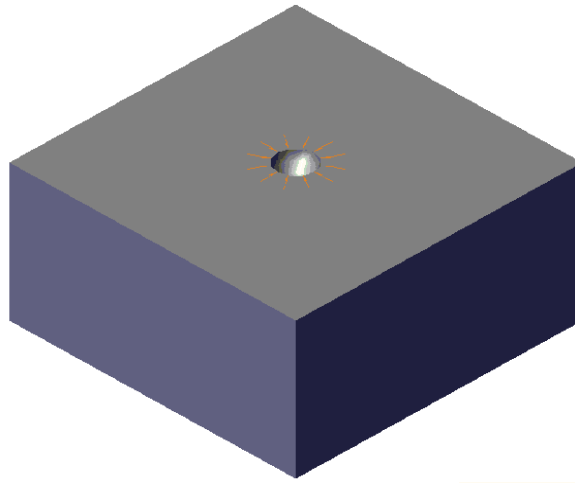


Figure 2-11 Void model in continuum mechanics domain.

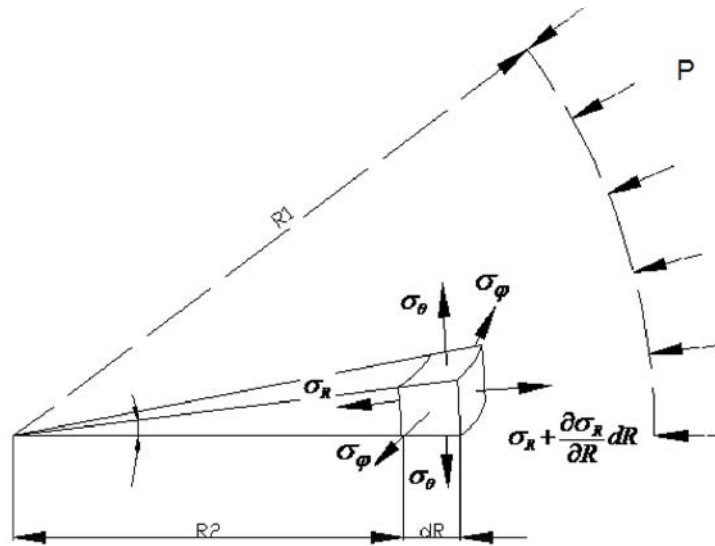


Figure 2-12 Free body diagram under spherical coordinate system.

By Hooke's Law in spherical coordinates, we have

$$\varepsilon_{\theta} = \frac{\nu\sigma_r}{E} + \frac{(1-\nu)\sigma_{\theta}}{E} \quad (2-43)$$

where  $E$  is Young's modulus and  $\nu$  is Poisson's ratio. Volumetric strain from the strain of our sphere in the  $\theta$  direction can be obtained by

$$\varepsilon_v = \varepsilon_{\theta} + \varepsilon_r + \varepsilon_{\varphi} \quad (2-44)$$

Applying *equations (2-40) to (2-44)*, the spherical stress is calculated to be  $-3932.57\text{MPa}$ , which is about 20% smaller than the virial stress  $P = -4932.38\text{MPa}$ . As stated in the previous section, in continuum mechanics, stress is defined as the internal force intensity across an imaginary face. It doesn't consider the particles that cross over the boundary. While in molecular dynamics, virial stress measures the momentum change in a definite group of particles. Only when the density change is negligible can the virial stress be approximated to be Cauchy stress. In this example, a reduction factor between atomistic and macroscopic scale will be needed to precisely consider the bulk modulus difference in between atomic scale method and continuum mechanics method. However, considering the small density of vacancies in the total lattice sites,  $C_v/C_a \approx 1 \times 10^{-5}$ , the vacancy relaxation factor can be safely estimated to be 0.12~0.15 in most cases. [59]

## 2.4.8 Conclusions

Using LAMMPS molecular dynamics simulator with the Embedded-Atom Method, we simulated an aluminum lattice at 533K. We outputted atom positions and virial stresses

for a particular atom and its first-nearest neighbors. That atom was then removed, and we used the change in positions to calculate the volume strain due to the creation of a void. We also calculated the volumetric strain induced spherical stress with continuum mechanics constitutive. The comparison of mechanical stress and virial stress shows that a reduction factor is needed in order to bridge material modeling methods applicable in atomic scale to macroscale.

# Surface Energies and Adatom Diffusivity



*“Madam, I swear I use no art at all.”*

For a metallic system under electrical load, effectively describing the electromigration process at the macroscale requires quantitative knowledge of vacancy diffusivity in lattice and grain boundaries, grain coarsening properties, and void flux and formation mechanisms at the microscale, just to name a few. Additionally, knowledge of surface energies for specific orientations of Sn’s lattice is a particularly important piece in the characterization of the behavior of solder joints and thin films undergoing electromigration. These energies provide an additional driving force for preferred orientation growth of thin films and it has been shown experimentally that  $\beta$ Sn prefers its (100) surface when grown on Si(111). [60] Surface energies of certain lattice orientations are also a major component in determining the morphology and stability of

voids that develop in thin film interconnects under electromigration conditions. [61][62]

In addition, diffusion of adatoms on these void surfaces control the overall void flux, with movement highly dependent on anisotropy of diffusivity and direction of the electric current. [63]

We can aid in the determination of such surface properties, normally computed experimentally, through the use of molecular simulation. Rare-event methods are available specifically for simulating diffusive processes in solid systems—typically slow at simulation timescales—and can be used with relative efficiency on workstation-grade computers or small computing clusters. [33][35][64] One technique, Henkelman’s Dimer method, has been used to calculate activation energies and attempt frequencies of Al adatom diffusive mechanisms with an EAM potential. [65] These compare well to *ab initio* calculations using the Nudged Elastic Band method and require many fewer potential force evaluations, without knowledge of the initial and final states of the system. In another work, they were able to show preference of multi-atom processes in simulated epitaxial growth of Al and Cu over long time scales. [66] Molecular simulation also aids in the prediction of surface energies. Zhang, et al. have used the MEAM potential to successfully calculate surface energies for various FCC and BCC metals, and predicted lowest energy surfaces in agreement with experimental results. [67][68]

In the present chapter, we combine an MEAM potential for Sn and the Dimer method in a quantitative study, to characterize the surface energies of  $\beta$ Sn and determine adatom diffusivities for  $\beta$ Sn’s lowest energy surface. To our knowledge at the time of publication, this work is the first study on the calculation of  $\beta$ Sn surface energies and

surface diffusion. This chapter continues with the details of our simulation setup in Section 3.1, describing the properties of the simulation cell for surface energy calculation and Dimer method simulations. Next, results from the surface energy calculations, Dimer simulations, and diffusivity computations are presented and analyzed in Section 3.2. We offer concluding remarks in Section 3.3.

## 3.1 Simulation Details

In creating the surfaces for our surface energy calculation, the solid lattice was rotated so its surface normal vector was perpendicular to the z-axis of the simulation cell. The system was periodic in the x and y axes and the z height fixed. This allowed for the creation of a two-surface slab. The thickness of the slabs was such that the two surfaces did not interact with one another. Typically, this is a value greater than twice the potential cutoff—ours often surpassed this and was dependent on the spacing between periodic Miller planes in the simulation cell z-direction. We use *equation (2-26)* to compute the surface energy relative to the bulk. A mathematically equivalent form is used by Zhang et al. [67][68]

While the static (near 0K) system and relationship in *equation (2-26)* offer a straightforward way to compute excess surface energies from molecular simulation, one might consider other choices for the quantitative comparison of unlike material surfaces. To unite the many relations and perceived inconsistencies in units of surface energy, Zhao, et al. proposed the extension of the bond-order-length-strength (BOLS) correlation that quantifies a volume-based energy density and incorporates the effect of temperature. [69] Key components here are the representation of atomic bond contraction of under-

coordinated surface and near-surface atoms, thermal expansion of the lattice, and their resulting effect on bond strength. For a more detailed investigation of surface energetics, the work of Zhao et al. may be considered.

For our dimer simulations, the simulation cell consisted of a 4x-4y-6z block of  $\beta$ Sn lattice with a single Sn adatom on the (100) surface. This surface is parallel to the YZ plane and the cell is periodic in these directions. A total of 217 atoms made up the system, governed by the MEAM potential with a cutoff of 4.5Å. Initially, an adatom was placed at random on the (100) surface and allowed to equilibrate to a low energy configuration using molecular dynamics. We presumed (and confirmed visually) that the adatom was now seated in a low energy pocket on the (100) surface. From this initial configuration, the dimer searches were carried out. Atoms within a distance of 8.7Å of the adatom are allowed to move, shown in *figure 3-1*. Before starting the search, the movable atoms close to the adatom were all displaced by a value between -0.2 and 0.2Å, drawn from a Gaussian distribution, increasing the dimer's ability to locate different low lying saddle point configurations. Once a saddle point configuration was found, the dimer was marched back along the lowest curvature mode to verify that it ended up in the initial minimum region. In *table 3-1* are the parameters used in the dimer saddle point and minimum searches. The energy of the saddle point, minimum region, and periodic points along the minimum energy path (lowest curvature mode) were saved. All atoms in the simulation are included in determining the specific energy of a configuration.

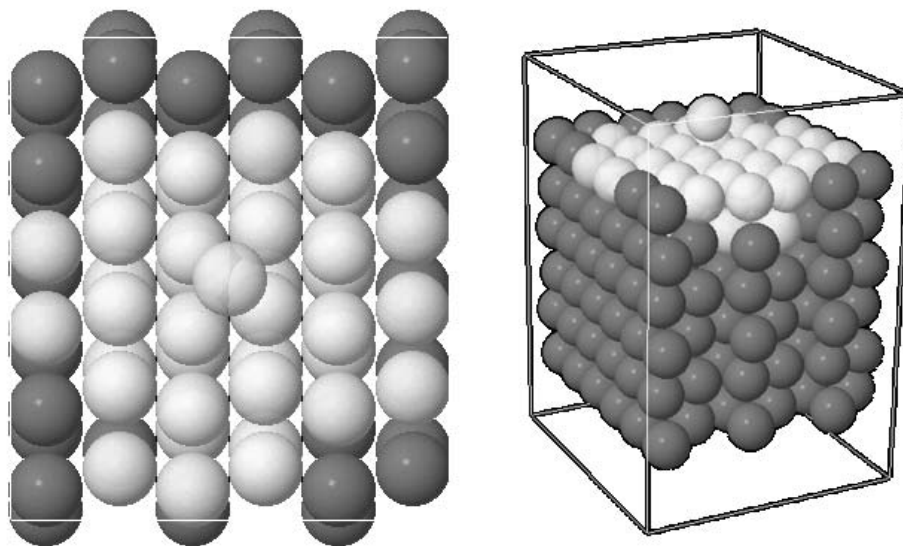


**Figure 3-1** LEFT a z-direction, top view of the (100) surface. RIGHT a 3-dimensional view of the simulation cell. Atoms are colored white to denote movable by the dimer method and gray for fixed.

**Table 3-1** Dimer method parameters.

	Length (Å)	Step length (Å)	Step converg.	Rot. converg.	Rot./step
<b>Saddle</b>	0.001	0.025	$F_{\text{center}} < 0.1 \text{ eV/\AA}$	$F_{\text{rot}} < 0.1 \text{ eV/\AA}$	2 max
<b>Min</b>	0.003	0.001	$E_{\text{front}} > E_{\text{center}}$	$F_{\text{rot}} < 0.1 \text{ eV/\AA}$	until converg.

At saddle-point and minimum-energy configurations only the 37 movable atoms are included in the vibrational normal mode frequency calculations. We computed the vibrational normal modes assuming atoms behaved as harmonic oscillators and developed a  $3N$  by  $3N$  matrix of the gradient of the force. The eigenvalues of this matrix are the normal modes of the system and were converted to vibrational frequencies.

## 3.2 Results and Discussion

### 3.2.1 Surface Energy Calculation for $\beta$ Sn

We calculated excess surface energies of the (100), (110), (101), (111), (210), and (201) un-relaxed surfaces for  $\beta$ Sn using the relation shown in *equation (2-26)* and a simulation setup described in Section III. Results from these calculations are shown in *table 3-2*, along with results from FCC surface energy calculations for Cu, Ag, and Al from Zhang and co-workers. [19] It is straightforward to identify the lowest energy surface for each of these elements—for Cu, Ag, and Al in an FCC crystal structure the lowest energy surface is (111), while for  $\beta$ Sn our calculations show that (100) is the lowest energy surface. For cubic structures, the (101) surface is equivalent to the (110) surface, as is (210) and (201).

**Table 3-2** Surface energies  $\gamma_s$  of  $\beta$ Sn, Cu, Ag, and Al with respect to Miller plane orientation. Cu, Ag, and Al are reproduced from [19].

hkl	$\gamma_s$ (eV/Å <sup>2</sup> )			
	$\beta$ Sn	Cu	Ag	Al
100	0.0497	0.1030	0.0795	0.0561
110	0.0622	0.1024	0.0765	0.0606
101	0.0569	--	--	--
111	0.0646	0.0879	0.0681	0.0386
210	0.0671	0.1069	0.0792	0.0666
201	0.0684	--	--	--

### 3.2.2 Surface Diffusion on (100)

Dimer searches were conducted starting from a low energy configuration of our adatom (100) surface system, equilibrated via low temperature molecular dynamics. The dimer searches provide information about the saddle point and minimum configurations for a given mechanism, and with this data we computed the theoretical tracer diffusivity for each mechanism found.

In our system a large number of configurational degrees of freedom exist, and we rely on the dimer method to seek out and find the many possible low lying saddle points available to the system as it undergoes some diffusive transition. More than one thousand searches, starting with random orientations of the dimer, converged to only three types of mechanisms. The first two involved the adatom moving across the surface in a hop mechanism. The third was a variety of different movements of the surface atoms, where atoms far removed from the adatom would “pop-up” out of the surface slightly. These would lead the system to a saddle point, as well as back to the initial minimum, but a second minimum was simply a partially raised surface atom and no movement of the adatom. Therefore, we considered only mechanisms in which the adatom moved. With this restriction, we found only the two hopping mechanisms contribute to adatom movement.

It is fairly straightforward to enumerate the saddle points a diffusing adatom would encounter hopping across the (100) face of a  $\beta$ Sn lattice. *Figure 3-2* illustrates the (100) surface of  $\beta$ Sn in an energy map, created by rasterizing the surface with an atom at a distance of  $2.0\text{\AA}$  above and recording the energy. The high energy ion-core locations are

shown in red, while the low energy pockets are shown in blue. Referring to this figure, it is quite clear where the saddle point for a single atom diffusion transition might be located. We have labeled the energy map with the location of the common minimum and two unique saddle points found in our dimer method searches and minimum energy path traces.

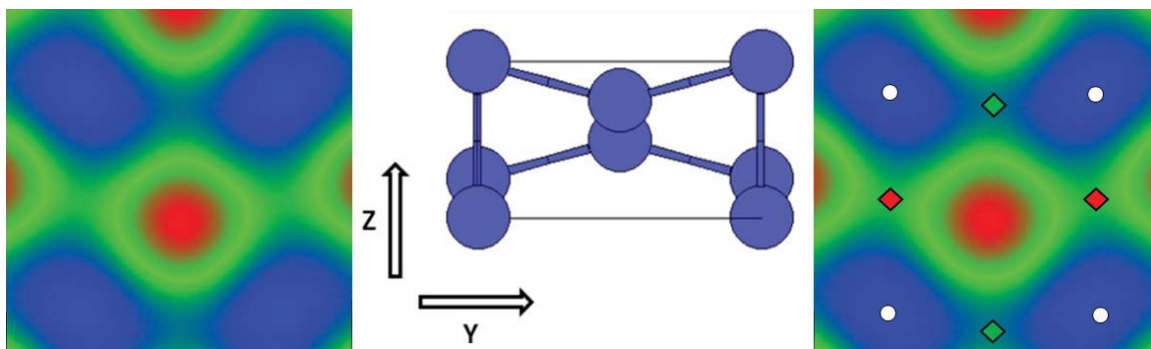


**Figure 3-2** Energy maps of the  $\beta\text{Sn}$  (100) surface. Left. Red denotes a higher energy (ion cores), blue denotes lower energy. Right. Diamonds are respective saddle point locations of the adatom, white circles are minima locations.

The two mechanisms found were a relatively simple movement of the adatom from one minimum energy pocket to the next closest minimum energy pocket. Looking at the (100) plane in *figure 3-2*, these translate to a z-direction movement (lattice *c-direction*) of the adatom and a y-direction movement (lattice *a-direction*) of the adatom. If a system started at one of the specified minimum configurations (white circles in *figure 3-2*), it could either move in the positive or negative c-direction through a saddle point (indicated by the red diamond) or in the positive or negative a-direction (indicated by a green diamond). Specific data from these mechanisms is shown in *table 3-3* and the energy values along the minimum-energy path are shown in *figure 3-3* as red and green curves.

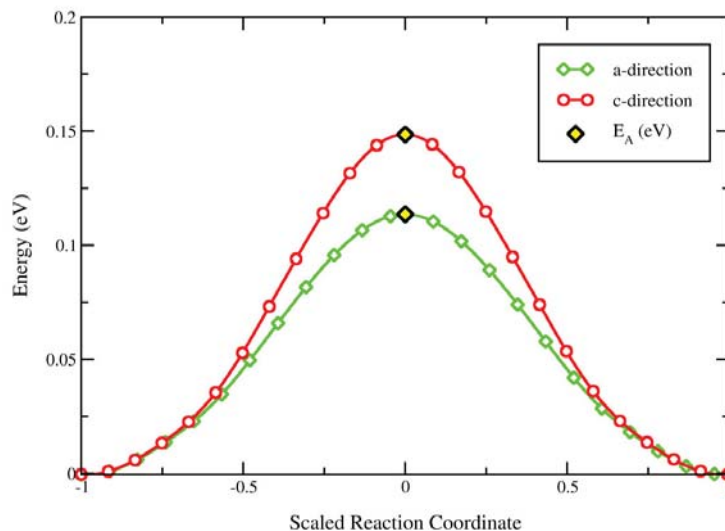


**Figure 3-3** Energy values along the minimum energy path for the given mechanisms. Values along the reaction coordinate are corrected to a baseline value of the minimum energy configuration—both mechanisms begin and finish at 0eV. Diamonds denote energies corresponding to saddle point configurations.

With the results of the dimer search, vibrational analysis, and displacement measurements, we computed the theoretical tracer diffusivity of the adatom for each mechanism at a temperature of 300K using *equations (2-21), (2-22), and (2-23)*. The factor  $\alpha$  for these diffusivities is taken to be 1 because the mechanisms move the adatom in only one dimension. Shown in *table 3-3* are our values for attempt frequency, activation energy, and diffusivity at 300K.

**Table 3-3** Mechanism data. Respectively, the adatom direction, mechanism activation energy, attempt frequency, distance the adatom traveled, and tracer diffusivity at 300K are specified.

Mechanism	$E_A$ (eV)	$\Gamma$ (THz)	$l$ (Å)	$D$ ( $10^{-06}$ cm <sup>2</sup> /s) 300K
c-dir	0.1493	1.17	3.23	1.893
a-dir	0.1138	0.745	2.96	3.994

Ratsch and Scheffler report that for Ag adatom on an Ag (111) surface, as the number of degrees of freedom considered in the vibrational normal mode frequency calculation increase, the attempt frequency decreases. [38] For their largest normal mode frequency calculation, they compute an attempt frequency value of 0.71THz, where  $3N=99$  and  $N$  is the number of atoms included. This result is similar to our calculations shown in *table 3-3*. In addition, their activation energy was calculated at 0.082eV for an adatom hopping on the (111) surface of Ag, known to be FCC's lowest energy surface, and compares on a similar scale to our measurements for an adatom hopping on  $\beta$ Sn's lowest energy surface. In contrast, Henkelman's results for Cu and Al adatom activation energies on higher energy (100) surfaces are 2 to 3 times larger than our values. [65][66]

Additional values of the theoretical tracer diffusivity for each mechanism are computed via the previously mentioned relations and an Arrhenius plot of diffusivity vs. temperature is shown in *figure 3-4*. The y-axis is in logarithmic scale and the x-axis is in inverse temperature scale. Here,  $\beta$ Sn's lattice anisotropy clearly plays a role in the directional diffusivity. At high temperatures however, this difference is less pronounced.

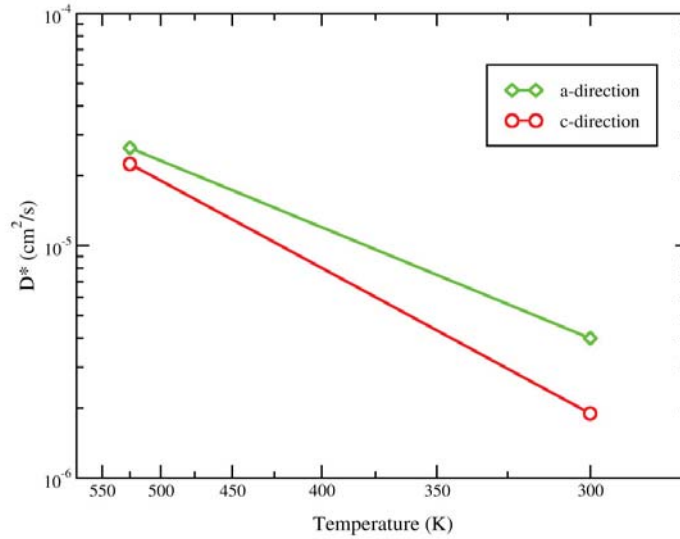


Figure 3-4 Arrhenius plot of diffusivity with respect to inverse temperature.

### 3.3 Conclusions

Our calculations of surface energies of various low index Miller planes of the  $\beta\text{Sn}$  phase indicate that the (100) surface has the lowest excess surface energy. A preference for the (100) surface has been shown in experiment, and our results using the MEAM potential confirm that from a surface energy minimization standpoint, the (100) surface preference should be exhibited in most epitaxial growth experiments. In addition, we also provide a list of surface energies for use in studies of void migration in  $\beta\text{Sn}$ . We have also shown results for the diffusivity of a Sn adatom on a  $\beta\text{Sn}$  (100) surface via theoretical and numerical methods. The adatom on the (100) surface exhibited hopping diffusion mechanisms in the a-direction and c-direction of the lattice. Attempt frequencies and activation energies were slightly different for each type of system. The differences in

each case correspond to unique behaviors of diffusivity with respect to temperature and directionality of diffusion.

In all our dimer simulations, we did not observe any concerted atom rearrangement like that of the Cu and Al (100) surfaces that Henkelman simulated. We believe this is most likely due to the apparent layering of the  $\beta$ Sn lattice in the [100] direction. An FCC lattice exhibits a tight, alternating packing in the [100] direction for successive (200) lattice planes, providing a physically and energetically deeper pocket for an adatom to sit on its surface. This may cause mechanisms involving concerted rearrangements to have activation energies similar to those involving adatom hopping. While for  $\beta$ Sn, successive (200) surfaces in the [100] direction appear shifted with respect to FCC. Atoms in the faces of  $\beta$ Sn's structure fall closer in line with its corner atoms along the [100] direction, creating sheet-like layers of atoms. Accordingly, an adatom on the energetically smoother (100) layer of  $\beta$ Sn may move much more freely by hopping than taking part in surface atom rearrangement.

# Grain Boundary Structure and Self-Diffusivity



*“This above all: to thine own self be true.”*

Diffusivities for different types of grain boundaries and a description of the boundary behavior with temperature, are critical in modeling microstructure evolution. Few experimental diffusion studies have been conducted on Sn grain boundaries, but activation energies obtained from experimental work on diffusion in the bulk Sn have been determined. They span a range of values. [9][70][71][72] Sun and Ohring suggest that some authors who report low activation energies may in fact be unknowingly measuring grain boundary diffusion. [72] Results from a significant number of bulk Sn studies are compiled in their work and reveal that grain boundary diffusion activation energies fall in a distinct range. In a follow-up study on polycrystalline Sn, Singh and Ohring measure grain boundary diffusivity at low and high temperatures. [9] Their high

temperature results match well with a cited second study on grain boundary diffusion and the values from Singh and Ohring's work are used in many studies of solder joint damage. One example is a finite-element simulation incorporating  $\beta$ Sn, Ag, and Cu diffusivities providing overall “solder joint diffusive activation energies” computed from time-to-failure measurements. [73]

In the present chapter, we employ molecular dynamics (MD) simulation to determine grain boundary diffusivity of specific  $\beta$ Sn grain boundaries. Although a significant amount of simulation work has been completed on grain boundaries in various materials and by a variety of methods, we believe, at the time of publication, this is the first to study  $\beta$ Sn grain boundaries. [41][64][74] We compare our results of diffusivities calculated in grain boundary structures to Singh and Ohring’s average  $\beta$ Sn grain boundary diffusivity and activation energy. Recent work by Telang and Bieler show the consumption and growth of particular grains of Sn when a polycrystalline sample is subjected to stress and high temperature anneal. [17][75] The specific grain boundary structures that persist in their work form the basis for the range of structures we study here. Notably, they see an increase in the number of (101) and (301) symmetric tilt grain boundaries present in their samples after separate stress and heat trials. [17] We construct the first of these boundaries in simulation, and include other structures that are of a similar grain boundary character. The range of grain boundaries studied can describe an average diffusivity one might expect in a polycrystalline sample, yet also exhibit individual behavior worthy of investigation.

This chapter follows with our simulation details in Section 4.1 as we outline our specific grain boundary structure choices and their minimization. We then present results with discussion in Section 4.2 and follow up with conclusions in 4.3.

## 4.1 Simulation Details

$\beta$ Sn phase grain boundaries in this work are created with custom Java code using the Etonica API and modeled using the modified embedded atom method (MEAM) with MD simulations conducted in the LAMMPS molecular simulation package. [58][76]

The process of minimization of the grain boundary is done in two steps. First, near 0K the two grains move independently in x, y, and z-directions via molecular dynamics, their respective atoms all having the same average force each time step. This step is shown in *figure 4-1-1*. An investigation in NiAl alloy grain boundaries by Mishin and Farkas employed the  $\gamma$ -surface technique to map out the energy surface created by the two static moving grains. [77] We do not employ this technique; however our 0K minimized structures do find lower energy configurations relative to their initial structure. Once a minimum energy structure has been found, the system is then equilibrated at the desired production run temperature, *figure 4-1-2*. Here, atoms in the bottom grain within twice the potential cutoff distance of the bottom edge of the structure are fixed and atoms in the top grain within twice the potential cutoff distance of the top edge of the structure are given an average force in the x, y, and z-directions. This creates a floating boundary at the top of the box and allows the system to reach an average zero pressure over 100 picoseconds. Following these steps, the floating boundary is now fixed and the grain boundaries are simulated between 2 and 4 nanoseconds, *figure 4-1-3*.

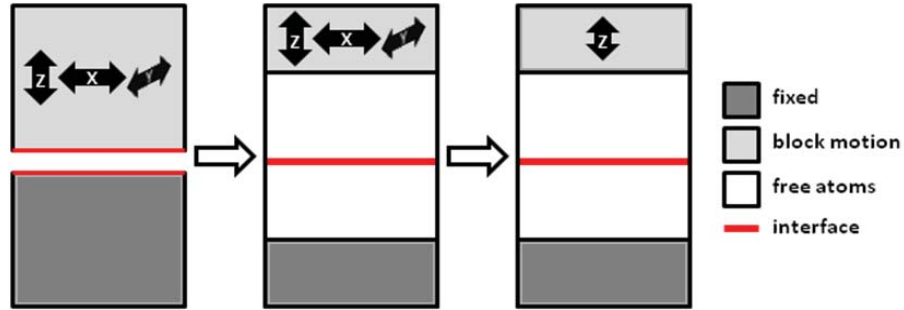


**Figure 4-1** (1) Minimization (near 0K-MD), (2) Equilibration, and (3) Production structures. Actual simulation cells are 3-dimensional and periodic in x and y-directions.

## 4.2 Results and Discussion

With MD we simulated five medium to high energy  $\beta$ Sn symmetric tilt grain boundaries. Specifically, boundaries with grains that share the (101), (201), (401), (310), and (410) Miller planes at their interface. For each grain boundary, we computed the excess potential energy at 300K from an average value sampled over the course of our molecular dynamics production runs. We also computed  $\delta_{GB}D_{GB}$  during the simulations and estimated the value of  $\delta_{GB}$ , the grain boundary diffusive width, at temperatures from 300K to 450K. From here we calculated  $D_{GB}$  for all boundaries in the temperature range and examined more closely directional diffusion in the interface of the (401) grain boundary.

### 4.2.1 Grain Boundary Excess Potential Energies

An often adequate measure of the order at the grain boundary interface and a characteristic of its transport behavior is the excess potential energy of a grain boundary. Outlined in a previous section, this quantity is the extra energy resulting from the low

coordination of interface atoms. Shown in *table 4-1* are computed excess energies of the five grain boundaries studied in this work. It is clear from these calculations that, depending on the Miller plane chosen, there exists a different degree of lattice mismatch, corresponding to an excess energy value. For the (101), (201), and (401) grain boundaries, the excess grain boundary energy decreases with increasing  $h$  index. However, for the (310) and (410) planes, the energy slightly increases with increasing  $h$  index.

**Table 4-1** Excess Interfacial Potential Energies (mJ/m<sup>2</sup>) at 300K.

GB	(101)	(201)	(401)	(310)	(410)
<b>300K</b>	1089.68	364.08	198.98	338.76	343.44

#### 4.2.2 Grain Boundary Width-Scaled Diffusivity ( $\delta_{GB}D_{GB}$ )

Results from squared displacement samples are shown in *figure 6*. Here we plot in Arrhenius form the scaled diffusivity,  $\delta_{GB}D_{GB}$ , versus temperature. In addition to data from our grain boundary simulations, experimental scaled diffusivity values from Singh and Ohring are shown as dark lines. [9] These lines represent the two different experimental relationships used to analyze the concentration profiles of Sn radiotracer in polycrystalline thin films. Arrhenius parameters for the experimental data plotted in *figure 4-2* are shown in *table 4-2*.

**Table 4-2** Arrhenius properties calculated from experiment in ref [9].

	300K to 350K	350K to 450K
$D_{GB}$ ( $10^{-8} \text{cm}^2/\text{s}$ )	1.45 (300K)	6.34 (350K)
$\delta_{GB}$ ( $10^{-8} \text{cm}$ )	5.0 (assumed)	
$E_A$ (eV)	$0.50^{+/- 0.04}$	0.4245
$D_0$ ( $10^{-2} \text{cm}^2/\text{s}$ )	$490^{+1560/-370}$	8.3

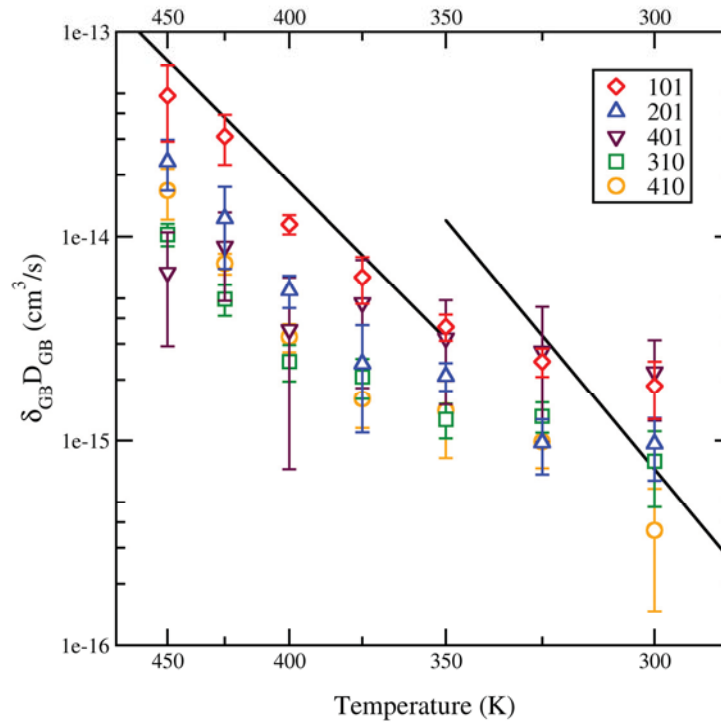


**Figure 4-2** Arrhenius plot of scaled diffusivity vs. temperature. Points are results for various symmetric tilt grain boundaries simulated in this work. Dark lines are experimental data from Singh and Ohring. [9] Error bars represent standard deviation of three independent simulations and computations of  $\delta_{GB} D_{GB}$ .

We can see from *figure 4-2* that the  $\delta_{GB}D_{GB}$  values for the simulated grain boundaries, with the exception of the (401) grain boundary, behave in a trend relative to their excess potential energies. For example, the (101) grain boundary exhibits the highest excess energy and the highest width scaled diffusivity. When compared to experiment at low temperature, the simulated boundaries show good agreement with experimental data. Magnitudes of the width scaled diffusivity at low temperature are all within the error reported in [9] and reproduced in *table 4-2*. An argument could be made about the large discrepancy in slope (diffusive activation energy) at low T, however when considering statistical uncertainty the slopes appear similar for many of the grain boundaries. This point will be discussed later in our analysis of  $D_{GB}$ . Continuing the comparison to higher temperatures, all our boundaries fall, at most, within one order of magnitude of experimental values and show a similar trend in slope. Further comparison of diffusivities is done by calculating  $D_{GB}$  using values of  $\delta_{GB}$  for each grain boundary at a range of temperatures.

### 4.2.3 Grain Boundary Width Calculation

To investigate possible changes in interface width with particular grain boundaries and/or temperature, we calculated planar profiles of diffusivity and structure in planes parallel to the grain boundary interface. For every grain boundary, at temperatures from 300K to 450K, diffusive and structural widths were calculated using methods outlined in the previous section. Shown below are two figures representing results from calculations of  $\delta_{GB}$ . The first, *figure 4-3*, presents planar diffusivity profiles of the five grain boundaries studied in this work. We have selected temperatures of 300K and 450K to display.

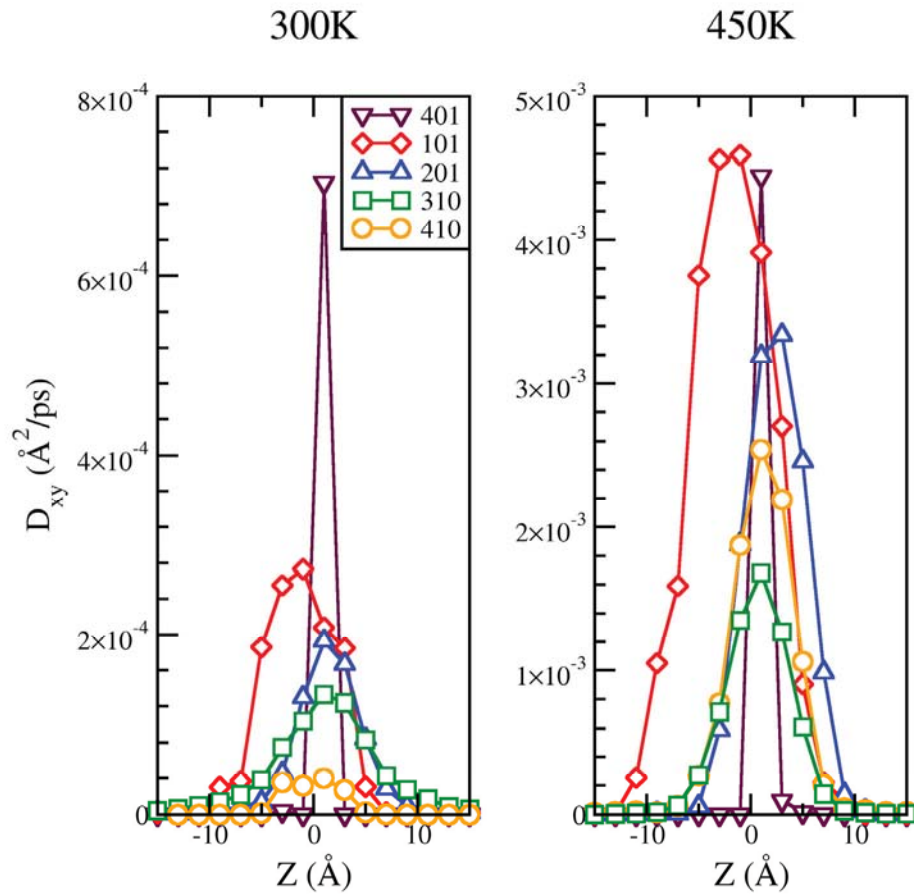


**Figure 4-3** Planar diffusivity for various grain boundaries at 300K (left) and 450K (right). Note the different scales for each temperature, but similar scales for  $z$ . Lines are guides for the eye.

As shown in *figure 4-3* for a temperature of 300K, we see an increase in planar diffusivity and an increase in diffusive width with increasing grain boundary energy. Here, the (401) boundary exhibits a relatively high diffusivity with a narrow width. For 450K, the (401) grain boundary again displays similar behavior, while the other boundaries now have a diffusivity within the same order of magnitude. Also, at higher temperature, the boundaries are shown to maintain their diffusive widths.

In addition to measuring the width via planar diffusion, we investigated the structural behavior of each grain boundary. *Figure 4-4* shows plots of the squared planar structure factor for each grain boundary. Each illustrates a change in the boundary's structure with temperature. The type of change varies between grain boundaries, but we note for the (101) and (201) grain boundaries, as we approach 450K the disordered structure at the interface grows in a width-wise fashion. For (401) and (410) the width is maintained, yet the amount of disorder changes with temperature. In *figure 4-5*, we include simulation snapshots for the (101) grain boundary at temperatures of 300K and 450K. For views oriented parallel to the grain boundary tilt axis, we see a slight decrease in ordering (increase in width) at the lattice-interface plane when comparing 300K to 450K.

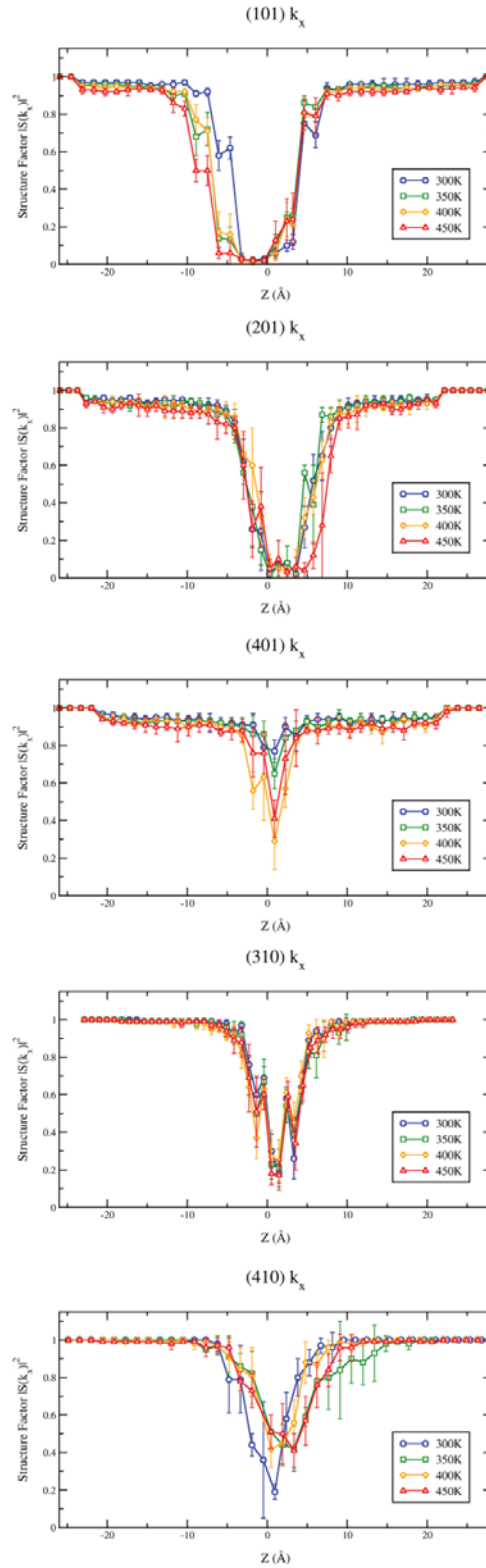


**Figure 4-4** Square planar structure factor vs. z-axis plane for the five grain boundaries studied. Colors are different temperatures. Blue-300K, Green-350K, Orange-400K, Red-450K. Error bars represent the standard deviation of  $|S(k)|^2$  in five snapshots from an MD run.

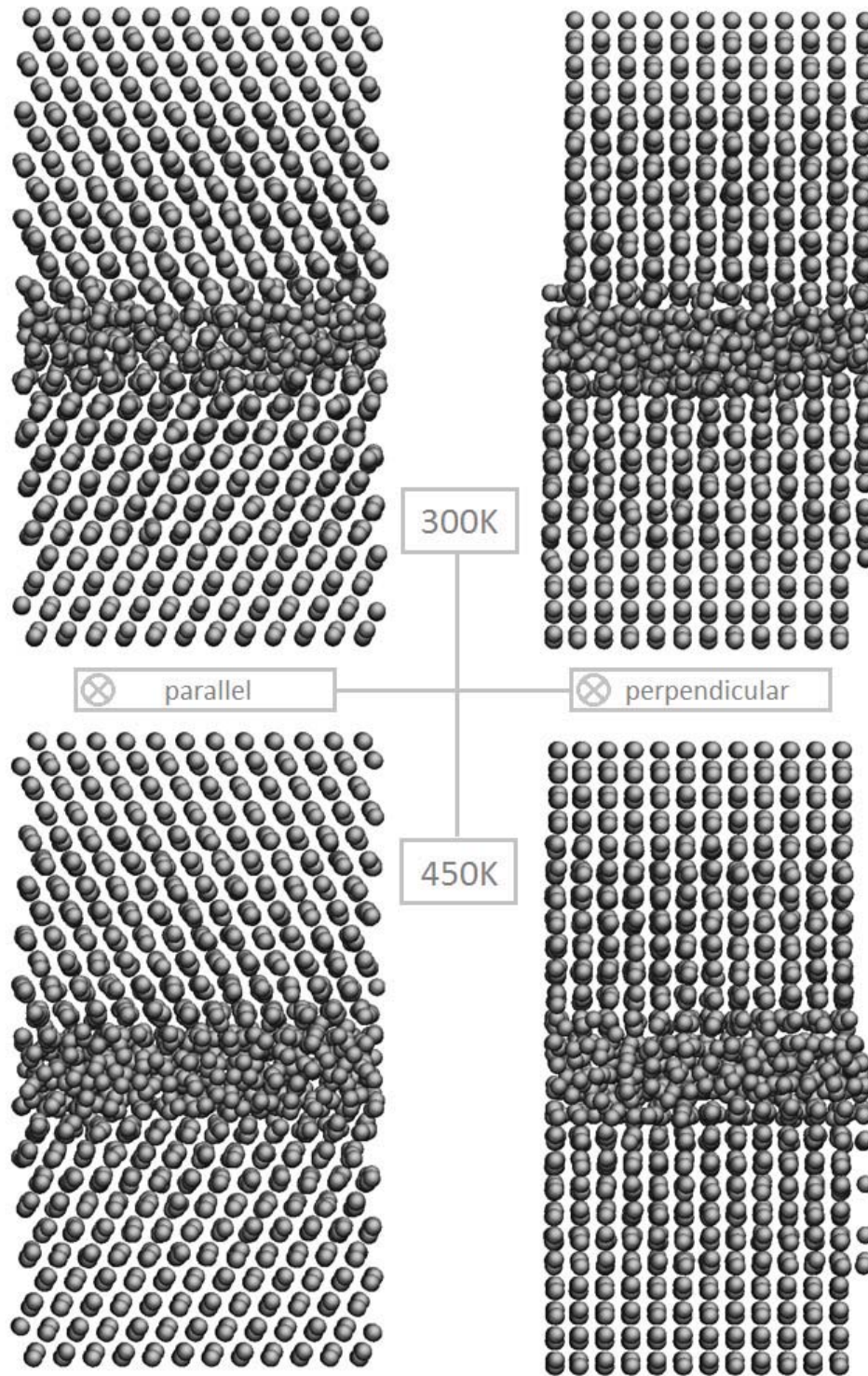


**Figure 4-5** TOP and BOTTOM are snapshots of the (101) GB at 300K and 450K, respectively. LEFT is looking parallel to the grain tilt axis and at RIGHT looking perpendicular.

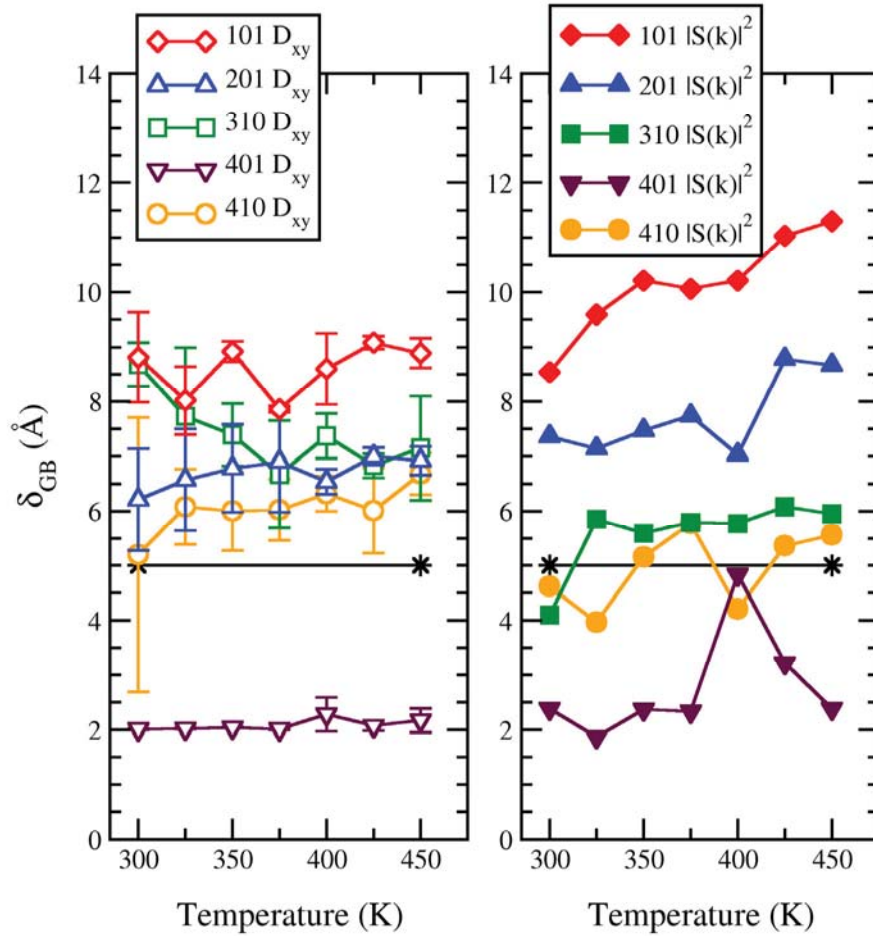


**Figure 4-6** Diffusive (open points, left) and structural widths (filled points, right) versus temperature for the five grain boundaries studied. Lines are guides for the eye. Black lines is the diffusive width used in ref [9].

Diffusive and structural widths for each grain boundary are compiled and plotted versus temperature in *figure 4-6*. We also include the value used in the experimental work,  $\delta_{GB} = 5.0\text{\AA}$ . From *figure 4-6* we can see that each grain boundary exhibits different widths. While not as distinct as the magnitudes of diffusivity, the high energy grain boundary shows the largest width, medium energies show slightly smaller widths, and the low energy (401) shows the smallest width. Contrasting the two types of analysis, diffusive

and structural, we see that the diffusive width remains relatively constant while the structural is more dynamic and increases with temperature for a few of the boundaries.

For the two boundaries ((101) and (201)) that show slight increases in their structural width with temperature, we also observe a large degree of disorder at the interface. Compared to the other plots in *figure 4-4*, these two boundaries exhibit almost no structure when compared to  $\beta$ Sn's bulk lattice. The extreme of this scenario is evidence of a large increase in grain boundary width and a transition to liquid-like disorder with an increase in temperature at points below the material's bulk melting point. This is referred to in literature as a "pre-melting" transition. Previous work by Koblinski et al. on molecular dynamics simulations of FCC Pd grain boundaries asserts the existence of grain boundary pre-melting at temperatures below the bulk melting temperature. [40] Their high energy boundaries undergo a transition to a confined liquid structure at a critical temperature dependent on boundary energy. Evidence of this liquid structure transition is given by a change in diffusion activation energy and a diffusivity that increases to a value close to the liquid value at the melting temperature. An earlier study by Ciccotti et al. of Lennard-Jones (310)- $\Sigma$ 5 grain boundaries found only partial structural disorder in this boundary as the melting point is approached. In their analysis, they compute a grain boundary diffusivity for their system near the melting point that is below the super-cooled liquid value at the same temperature. [42] In another study by Suzuki and Mishin, where Cu (210)- $\Sigma$ 5 and (310)- $\Sigma$ 5 grain boundaries were simulated up to the melting point, they did not see any evidence of pre-melting in their systems. They do note however, that all the grain boundaries collapse on a common self-diffusivity close to the melting temperature. [41] Similar to reports in literature, the various studies

of structure and dynamics in our grain boundaries do not explicitly show that pre-melting is occurring for  $\beta\text{Sn}$ . We do see disordered interfaces develop for the (101) and (201) grain boundaries and they remain stable throughout the temperature range studied in this work. While this may suggest the notion of pre-melting in our boundaries, the foundation of its existence is dependent on a change in slope of the grain boundary diffusivity.  $D_{GB}$  at high temperature must also present a value close to liquid self-diffusivity as the melting point is approached. Upon further analysis, detailed in the next section, we see no change in the slope of  $D_{GB}$  as temperature is increased and magnitudes that do not approach the liquid diffusivity as the melting point is approached. We can therefore say that although some of our simulated interfaces show disorder, none exhibit the pre-melting phenomenon.

#### 4.2.4 Resolving the Grain Boundary Diffusivity ( $D_{GB}$ )

Using values of the diffusive width ( $\delta_{GB}$ ) for each temperature and grain boundary type, we now resolve  $D_{GB}$  for each grain boundary, and remove the effect of  $\delta_{GB}$ 's variation with grain boundary type on  $\delta_{GB}D_{GB}$  previously shown in *figure 4-2*. Here, the specific grain boundary self-diffusivity,  $D_{GB}$ , for each type studied in this work is shown in *figure 4-7*. The standalone data in *figure 4-7* is the (401) grain boundary. It now shows its true diffusivity in comparison to the other simulated grain boundaries. Although the width is small, the low energy (401) boundary exhibits fast, low activation energy, diffusion. This behavior is given further study in the next section. Singh and Ohring report values of  $D_{GB}$  using  $\delta_{GB} = 5.0\text{\AA}$  to adjust their experimentally measured values of  $\delta_{GB}D_{GB}$ . This is also plotted in *figure 4-7*. Compared to *figure 4-2* and relative to Singh and Ohring's

reported values, we see similar trends from the (201), (310), and (410) grain boundaries. For the (101) grain boundary, the magnitude of  $D_{GB}$  has shifted slightly lower relative to the experimental results. Our low temperature values, 300K to 350K, still fall within the error in Singh and Ohring's measurements, outlined in *table 4-2* (though no error is listed for high temperature), and all our values are still within one order of magnitude of experiment. It is important to mention finally that using any value larger than  $\delta_{GB} = 5.0\text{\AA}$  with the experimental results will decrease the gap between it and simulation. The authors of ref. [9] do not mention the significance of this value for  $\beta\text{Sn}$ , although in other works, when used in analytical expressions, it is shown to match experimental results in higher melting point materials, such as Ag. [78]

**Table 4-3** Arrhenius Properties of Simulated Grain Boundaries from weighted least squares fit, 325K to 450K

<b>GB</b>	<b>(101)</b>	<b>(201)</b>	<b>(401)</b>	<b>(310)</b>	<b>(410)</b>
$D_{GB-300K} (10^{-8}\text{cm}^2/\text{s})$	2.11	1.55	10.9	0.914	0.700
$E_A (\text{eV})$	0.263(4)	0.295(5)	0.10(1)	0.22(5)	0.274(7)
$D_0 (10^{-4}\text{cm}^2/\text{s})$	2.9(4)	6(1)	0.08(5)	2.2(8)	40(2)

The slopes of simulation data from 350K to 450K show good agreement with experiment. At low temperatures of 300K and 325K however, average values from multiple simulations create a low-slope region. This behavior is similar to that in *figure 4-2* and is maintained even after removing the influence of width. While the amount of error shows that statistically, these points may have a slope that is similar to higher temperature data, we've restricted the analysis of  $D_{GB}$  to values simulated at temperatures of 325K to 450K.

We believe the large error at 300K arises from poor sampling because of the timescale constraints of molecular dynamics. A weighted least squares fit is applied to *figure 4-7* diffusion data in this temperature range to calculate Arrhenius parameters for each grain boundary. These are shown in *table 4-3*.

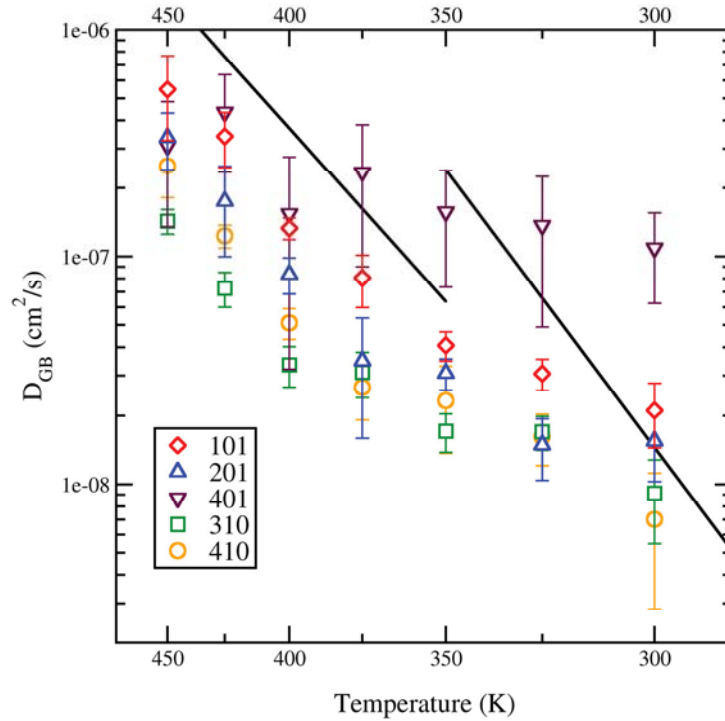


**Figure 4-7** An Arrhenius plot of grain boundary diffusivity vs. temperature. Shown as colored points are various symmetric tilt grain boundaries simulated in this work. Dark lines are experimental data from Singh and Ohring. Error bars represent standard deviation of three or more independent simulations.

#### 4.2.5 Analysis of In-plane Directional Diffusivity

In *figure 4-7* and *table 4-3*, we see a contrast in slope of the (401) grain boundary when compared to other low  $D_{GB}$  grain boundaries (e.g. (310), (410)). While of low excess potential energy and therefore high atomic coordination at the interface, the activation energy of diffusion in this grain boundary is low. This duality is indicative of possible

channel structures forming at the interface in a single direction. [30] Accordingly, we investigated the development of any anisotropy in diffusivity in the plane of the grain boundary interface. Shown in *figure 4-8* are plots of  $(h10)$  and  $(h01)$  grain boundaries and their respective  $\delta_{GB}D_{GB}$  component values. For both plots, diffusion in the direction parallel to the grain tilt is shown as open points and diffusion perpendicular to the grain tilt is shown as filled points. For the  $(310)$  and  $(410)$  grain boundaries, shown in the left plot, self-diffusion in either direction is essentially equivalent. For the  $(101)$ ,  $(201)$ , and  $(401)$  however, as the  $h$  index of the grain boundary is increased, a degree of anisotropy in the diffusion coefficient develops.

If we focus on the  $(401)$  grain boundary, we can see a high degree of directional diffusivity. This is also evidenced in simulation snapshots, shown below in *figure 4-9*. By inspection, the structure of the  $(401)$  grain boundary is much more evident in a view down the grain tilt axis ( $[010]$ ), as shown in the parallel view direction of *figure 4-9*. Conversely, the perpendicular view direction of this figure shows a thin interface with disordered atoms.

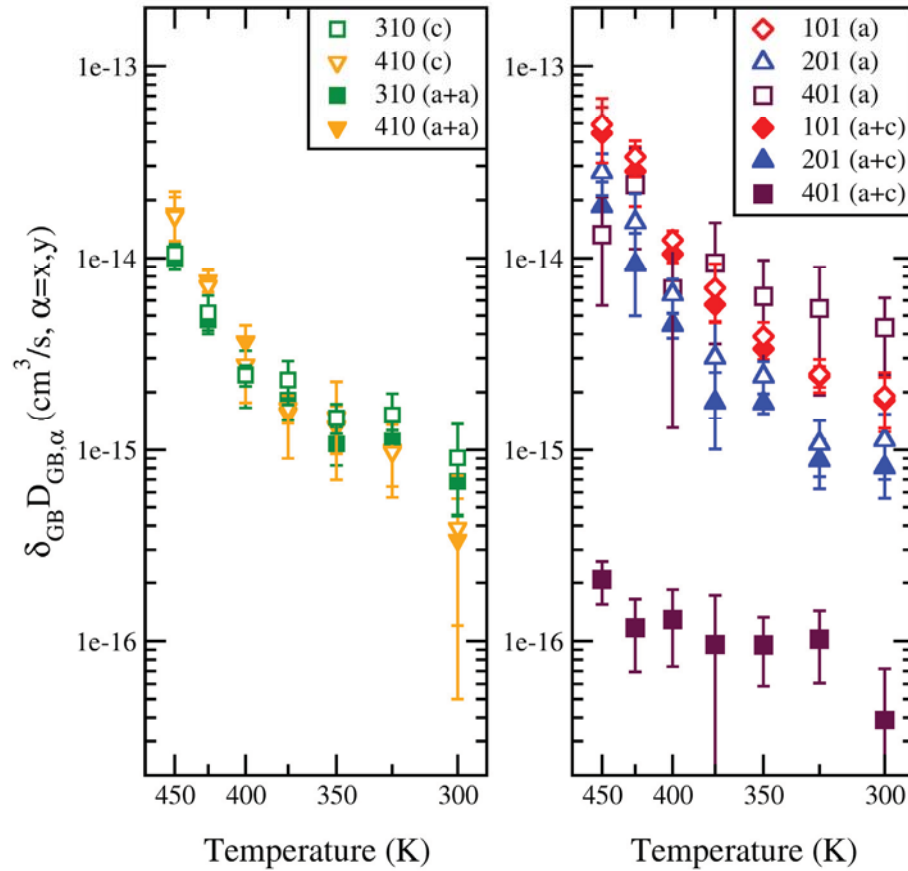


**Figure 4-8** Arrhenius plots of scaled directional diffusivity vs. temperature. Left are (310) and (410) grain boundaries, Right are (101), (201), and (401) grain boundaries. Filled points are diffusion in a direction perpendicular to the grain tilt axis; Open points are diffusion in a direction parallel to the grain tilt axis. Letters in parentheses in the plot legends are crystal lattice directions of diffusion. Error bars represent standard deviation of three or more independent simulations.

We can explain the behavior of the (401) grain boundary in *figure 4-7*, *figure 4-8* and *figure 4-9* by first referencing the  $\beta$ Sn crystal structure. It has been shown in experiment that diffusion in the c-direction of the bulk crystal proceeds much more slowly than diffusion in the a-direction. [70] When we identify the crystal orientation in these grain boundaries, we notice that for increasing Miller index in the  $h01$  boundaries, the interface adopts more of the c-direction of the bulk lattice. This behavior is shown in *figure 2-2*, where in moving from the (101) to (201) to (401), red to blue to purple in the figure, the

interface shared by the two grains increasingly aligns with the c-direction of the lattice. The  $\beta$ Sn bulk lattice anisotropy does not explain the loss of structure, however. The simulation snapshots in *figure 4-9* show a disordered structure parallel to the grain boundary interface and parallel grain tilt direction (shown in the perpendicular view). This can be explained by the existence of channels in the interface that aid in fast solvent and solute diffusion. We can say at this point that the (401) grain boundary's anisotropic diffusivity is a function of both the tetragonal crystal structure, and the formation of structural channels.

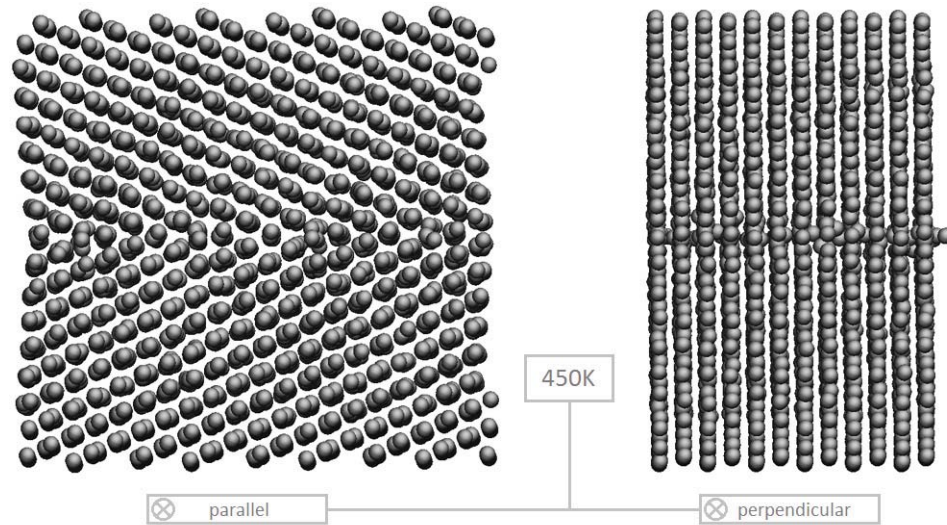


**Figure 4-9** Simulation snapshot of (401) grain boundary at 450K. LEFT is looking down the grain tilt axis and at RIGHT the grain tilt axis is oriented left/right.

### 4.3 Conclusions

This work investigated diffusion in five grain boundaries, the (101), (201), (401), (310), and (410) symmetric tilts. Our structures are based on those shown to exist in experiment

and those that exhibit sufficient motion for squared displacement calculations during molecular dynamics simulations at temperatures of 300K to 450K. We find that  $\delta_{GB}D_{GB}$  is not the most effective way to describe the transport behavior of these grain boundaries. One must also investigate the boundary's interface width.

By determining the structural and diffusive widths of the interfaces of the grain boundaries, we can resolve the specific grain boundary diffusivity,  $D_{GB}$ , for each type. The diffusive width is used to back out  $D_{GB}$  from the simulation quantity  $\delta_{GB}D_{GB}$ , while the structural width analysis reveals information about possible changes in structural order of the grain boundaries. Calculation of the parameter  $\delta_{GB}$  shows that a grain boundary with higher energy will exhibit a larger width. We also show that this width remains fairly constant at temperatures from 300K to 450K. Specifically for the (101) grain boundary, structural and diffusive widths reveal a highly diffusive, disordered structure in comparison to other boundaries in this work. The (201) grain boundary exhibits this to a lesser extent. Parameters necessary to formulate an Arrhenius relation for each grain boundary, such as activation energy and diffusive prefactor, are tabulated.

A directional analysis of the diffusivity in each grain boundary interface illustrates anisotropy in diffusivity, developing as the  $h$  Miller index is increased from 1 to 2 to 4 in ( $h01$ ). Further analysis of the (401) grain boundary shows that even at low temperatures, it is a fast diffusing interface dominated by structural channels. This is described in two parts. We first show this by examining the slow bulk lattice diffusivity of  $\beta\text{Sn}$  in the crystal's c-direction ([001]). In this case, the lattice c-direction is perpendicular to the axis of grain tilt ([010]) in the (401) grain boundary, lending very slow diffusion to the

boundary in this direction. Second, it is confirmed by inspection of simulation snapshots and knowledge of the boundary's excess energy. For a boundary of such low excess potential energy compared to a bulk structure, and such high diffusivity with low activation energy, stable structural channels must develop in the interface. We see this disorder in only the perpendicular-to-tilt view of the grain boundary. These two observations explain slow diffusion in the perpendicular direction of the interface, and overall low activation energy and fast diffusion in the (401) boundary caused by disordered channels in the parallel direction of the interface.

# Solute Effects on Grain Boundary Energy and Shear Stress

*“Neither a borrower nor a lender be...”*

The structure of Sn, commonly microcrystalline or polycrystalline  $\beta$ Sn in solder joints, allows for a range of macroscale material strength and mass diffusion regimes, both resulting from the frequency and types of boundaries created by the  $\beta$ Sn grains.

[9][17][75] Many factors influence the size of the grains and amount of grain boundaries in a joint. Current experimental work shows that solder joints exhibit varying types of microstructure, due in part to changing solute concentration. In 2009, Seo et al. examined Sn- $x$ Ag and Sn- $x$ Cu solder joints and found that microstructure was significantly affected by alloy composition and cooling rate. [18] In a later but similar work by the same authors, the time evolution of microstructure is examined during high-temperature aging, and solute concentration is shown to affect grain growth. [79] Earlier

work by Telang et al. confirms Seo et al.'s findings. [17] For pure Sn ingots, reflowed Sn, and solder joints with concentrations of Ag similar to that of Seo et al., they observe a similar fine microstructure of  $\beta$ Sn.

Studies at an atomistic level have investigated the effect of size, cohesive energy, and concentration of solute atoms on total grain boundary energy ( $E_{GB}$ ). In 2005, Millett et al. showed that Lennard-Jones solute atoms of a range of sizes are more effective at lowering  $E_{GB}$  than atoms of various cohesive energies. [46] In fact, atoms with larger cohesive energies increased  $E_{GB}$ . Millett's work also demonstrates the possibility of solute stabilization of grain growth in nanocrystals. [48] They show that for a nanocrystalline system of LJ atoms, at concentrations of solute atoms greater than 2.0%, all grain growth is halted during molecular dynamics simulations of the system. Furthermore, they compute the excess energy of the grain boundaries (difference from the bulk structure with solute), and find that at these concentrations, the nanocrystalline system exhibits a lower energy than the bulk single crystal counterpart.

The recent experimental studies on Ag and Cu solute effects on  $\beta$ Sn microstructure, solid base of theory and simulation work, present an opportunity to use molecular simulation to directly model a realistic system, with the goal of quantifying and explaining solute effects at an atomistic level. In this work we use molecular dynamics simulation to examine the effect that low-to-moderate concentrations of Ag and Cu solute atoms have on the grain boundary energy of  $\beta$ Sn. The (101) symmetric tilt boundary of  $\beta$ Sn is simulated with varying amounts of solute, and using the Modified Embedded-atom method, we obtain values for the segregation enthalpy of Ag and Cu, as well as

respective critical excess solute amounts. We also investigate the behavior of the solute stabilized boundaries under shear stress as a function of solute amount and compare these to experimental and simulation work. Finally, we offer conclusions that explain some of the behavior exhibited by the solder joints in experimental work.

We continue this chapter with an explanation of the details of our simulation setup and data collection in Section 5.1. We then present and discuss our results of grain boundary energy calculations and shear stress simulations in Section 5.2, and end with conclusions in Section .

## 5.1 Simulation Details

In our simulations, we are modeling the (101) symmetric tilt grain boundary of  $\beta\text{Sn}$ , with varying amounts of Ag or Cu solute particles randomly placed in interstitial positions along the interface. The grain boundary with solute configurations are constructed with the Etomica Molecular Simulation API. [76] Interactions between Sn and Ag, and Sn and Cu are modeled with the Modified Embedded-atom method (MEAM) in the LAMMPS Molecular Simulator. [24][58]

Similar to Chapter 4, our simulation cell is periodic in the directions parallel to the grain boundary interface, and fixes atoms at the top of grain 1 and at the bottom of grain 2, mimicking a bulk structure and creating a “sandwich” of movable atoms. [30] Various quantities of solute are then randomly inserted into interstitial positions at the grain boundary interface. The final structure is shown in *figure 5-1* as a normal and expanded view. In this type of setup it is important to equilibrate the system correctly in order to

obtain a grain boundary interface of minimum energy, and to simulate at an average pressure of zero.

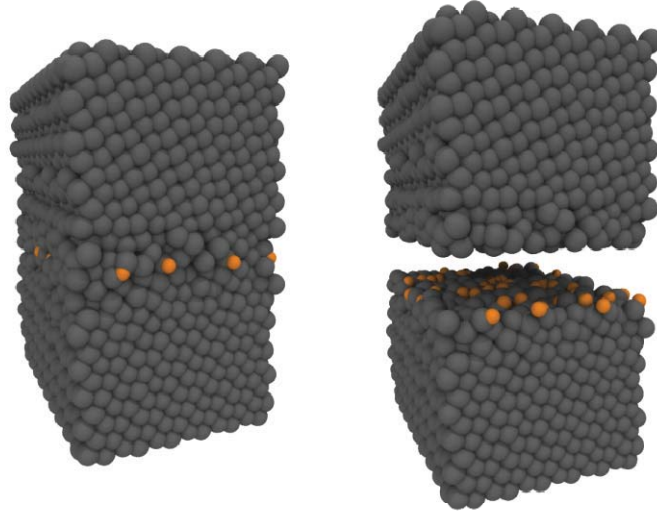


**Figure 5-1** Typical configuration of grain boundary with its interface loaded with solute (orange). LEFT is a simulation snapshot after equilibration and RIGHT is the same snapshot with the interface exposed for clarity.

**Table 5-1** Ag and Cu solute quantities and corresponding excess interfacial density.

$N_s$ (atoms)	5	10	25	50
$\Gamma_s$ ( $10^{-3}$ atoms/ $\text{\AA}^2$ )	2.085	4.171	10.43	20.85

The process of equilibration of the grain boundary is done in three steps, followed by our shear simulation. First, near 0K the two grains move independently in x, y, and z-directions via molecular dynamics, their respective atoms all having the same average force each time step. This step is shown in *figure 5-2-1*. Next, solute atoms are randomly inserted at interstitial positions in the grain boundary interface. Shown in *table 5-1* are the specific amounts of solute inserted and their corresponding interfacial excess

density. The positions of the solute atoms are then adjusted via a conjugate gradient energy minimization, while holding the Sn atoms fixed (*figure 5-2-2*).

Finally, once a minimum energy configuration is found, the system is then equilibrated for 100 ps using molecular dynamics (MD) with a *Nose-Hoover* thermostat and barostat (NPT) at the desired production run temperature and with a timestep of 0.001 ps (*figure 5-2-3*). Here, atoms in the bottom grain within twice the potential cutoff distance of the bottom edge of the structure are fixed and atoms in the top grain within twice the potential cutoff distance of the top edge of the structure are given an average force in the x, y, and z-directions. This creates a floating boundary at the top of the box and allows the system to reach an average pressure of zero over 100 ps. During the last 50,000 timesteps (50 ps) of this step we collect our average energies of grain boundaries with solute concentrations shown in *table 5-1*.

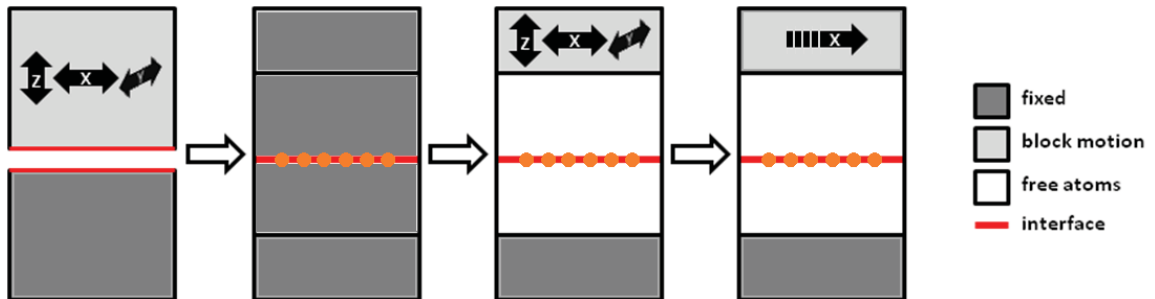


**Figure 5-2** (1) Grain boundary minimization (near 0K), (2) Solute minimization, (3) NPT MD equilibration, (4) NVT MD Shear simulation. Filled arrows indicate direction of motion of the block portion. Orange circles are solute at interface. Free atoms are movable in x, y, and z directions. Actual simulation cells are 3-dimensional and periodic in x and y directions.

Following these steps, the floating boundary is fixed in the y- and z-directions, and moved at a constant velocity of  $v_x = 5 \times 10^{-4} \text{ \AA/ps}$  in the x-direction. Initially, the free

atoms of the system are given an additional x-velocity profile in the z-direction to offset the sudden shock of the moving top boundary. The initial profile is linear from  $(v_x, z)$  points of  $(0.0\text{\AA}/\text{ps}, -40\text{\AA})$  to  $(5 \times 10^{-4}\text{\AA}/\text{ps}, 40\text{\AA})$ . For a system under shear, we calculate the off-diagonal term of the stress tensor describing the stress in the direction of the shear force and the out of plane normal. In this chapter, all shear is in the x-direction of the x-y plane, so the desired stress is  $\tau_{xz}$ . It follows that the shear strain rate is given by *equation (5-1)*, where  $v_x$  is the shear velocity in the x direction and z is the height of the simulation cell.

$$\dot{\gamma} = \frac{v_x}{z} \quad (5-1)$$

Applying *equation (5-1)*, this becomes the equivalent to a shear strain rate of  $\dot{\gamma} = 6.25 \times 10^6 \text{ s}^{-1}$ , as all of our systems have a height (in z-direction) of roughly  $80\text{\AA}$ . During the shear, systems containing various amounts solute are simulated with constant volume (NVT) MD between 9 and 15 ns (*figure 5-2*) using the same timestep as in step 3. Our simulation box remains un-deformed.

Doing work on the system in the form of shear adds energy, and for significant shear strain rates this can have an effect on the temperature. It is customary in this case to either compute the temperature using a non-sheared component of the velocity, or to remove the shear effect by subtracting shear velocity based on an atom's location perpendicular to the shear direction (effectively removing our initial velocity profile).

[81][82] Although we are imposing a comparably low shear rate on our system, we use

the method of ref. [82] and subtract the shear velocity profile from our kinetic energy calculation before computing the temperature.

## 5.2 Results and Discussion

Molecular dynamics simulations of the (101)  $\beta$ Sn grain boundary are conducted for various temperatures and solute concentrations. The average energy of each structure containing amounts of Ag and Cu listed in *table 5-1* is determined and used with the energy of the pure boundary to compute the enthalpies of segregation for Ag and Cu at different temperatures. We also investigate the behavior of this boundary with 25 and 50 solute atoms under a constant shear rate. As a complement to the excess energy calculation, measuring the boundary's response to a steady shear and observing the yield stress offers a way to qualitatively represent the structural stability of the boundary and the effect of solute atoms on boundary slip.

### 5.2.1 Excess Enthalpy Calculations

*Table 5-1* lists the four excess solute concentrations inserted into the (101) grain boundary interface. At temperatures of 300K, 350K, 400K, and 450K, molecular dynamics simulations were used to obtain the average energies of all the temperature-solute amount combinations. Following the procedure outlined in Sections 2.3.1 and 2.3.2, the excess energies of the boundary with solute and the pure boundary were computed. Employing *equation (2-31)*, we know  $H_{EX,GB+S}$ ,  $H_{EX,GB}$ , and  $\Gamma_{EX}$  for each temperature, and can solve for  $\Delta H^{SEG}$ , the enthalpy of segregation. In *figure 5-3* we plot  $H_{EX,GB+S}$ , the excess energy of the grain boundary with solute, as a function of interfacial

excess solute concentration,  $\Gamma^{EX}$ . At each temperature, the weighted least-squares method was used to determine trend lines, and the slope of these lines is the solute's enthalpy of segregation. The first rows of *table 5-2* and *table 5-3* report these values.

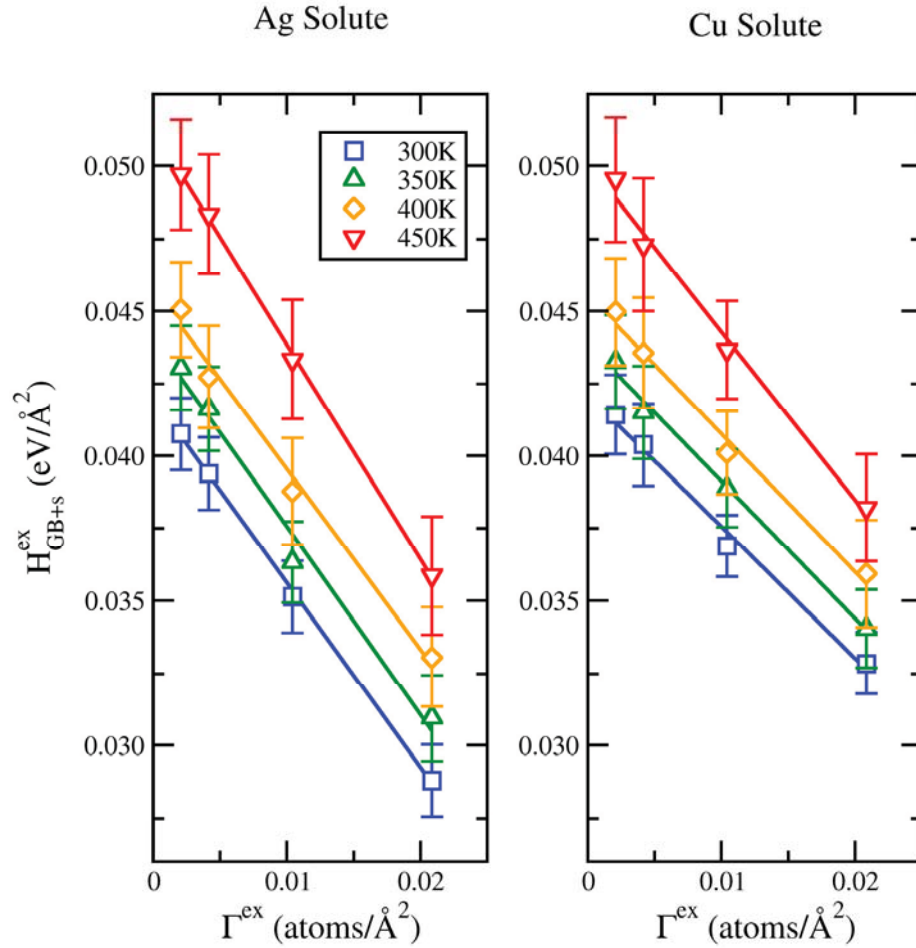


**Figure 5-3** Difference in the excess enthalpies of the solute loaded grain boundary and bulk  $\beta$ Sn with an equal amount of solute ( $H_{EX,GB+s}$ ) vs. excess solute concentration ( $\Gamma^{EX}$ ). Error is the standard deviation. Trend lines are fitted by a weighted least-squares analysis.

*Equation (2-31)* also allows for the possibility of reducing the energy of the grain boundary with solute to a value equal to, or less than, that of the pure crystal. In *figure 5-3*, the trend lines for each temperature will intersect the y-axis of the plots at or near

the value for the excess energy of the pure grain boundary (i.e. where  $I^{ex} = 0$ ). In the case of a grain boundary with a given amount of solute,  $H_{EX,GB+S} = 0$  represents a structure with no energy difference in comparison to the bulk structure with solute. It follows then from *equation (2-31)*, as we add solute to the grain boundary (and corresponding bulk structure), that the excess energy of the boundary will eventually be reduced to  $H_{EX,GB+S} = 0$ . We denote this point as the critical excess solute concentration,  $\Gamma_{CR}$ . This, along with the actual number of solute atoms for our system  $N_{A,CR}$  is reported in the remaining rows of *table 5-2* and *table 5-3* for Ag and Cu solute additions.

**Table 5-2** Ag solute calculations of enthalpy of segregation ( $\Delta H^{seg}$ ), critical excess interfacial concentration ( $\Gamma_{cr}$ ), and critical number of solute atoms ( $N_{A,cr}$ ). Error is a weighted least squares fit on *Figure 5-3*– Ag slope.

Temperature (K)	300	350	400	450
$\Delta H^{seg}$ (eV/atom)	0.64(9)	0.65(10)	0.62(12)	0.74(14)
$\Gamma_{cr}$ ( $10^{-3}$ atoms/ $\text{\AA}^2$ )	106	103	105	91
$N_{A,cr}$ (atoms)	256	248	252	219

**Table 5-3** Cu solute calculations of enthalpy of segregation ( $\Delta H^{seg}$ ), critical excess interfacial concentration ( $\Gamma_{cr}$ ), and critical number of solute atoms ( $N_{A,cr}$ ). Error is a weighted least squares fit on *Figure 5-3*– Cu slope.

Temperature (K)	300	350	400	450
$\Delta H^{seg}$ (eV/atom)	0.45(8)	0.47(10)	0.48(13)	0.58(14)
$\Gamma_{cr}$ ( $10^{-3}$ atoms/ $\text{\AA}^2$ )	150	142	137	116
$N_{A,cr}$ (atoms)	360	340	328	280

## 5.2.2 Segregation Enthalpies from Molecular Simulation

From the slope of the fitted lines in *figure 5-3*, we see that both Ag and Cu lower the excess energy of the boundary when compared to the bulk structure containing the same amount of solute. After computing values for  $\Delta H^{SEG}$  for both solutes, it is clear that Ag lowers the energy more for an equal amount of solute and accordingly, has a larger driving force for grain boundary segregation. A larger  $\Delta H^{SEG}$  corresponds to a smaller number of atoms required to meet the critical excess interface concentration,  $\Gamma_{CR}$ . This behavior is consistent with the trends observed by ref. [46]. In that work, Millett, et al. modeled a Cu grain boundary with solute using the Lennard-Jones (LJ) potential. For their Cu system in reduced units, the atomic cohesive energy was  $\varepsilon_{Cu} = 1.0$ , and the atomic radius was  $\sigma_{Cu} = 1.0$ . By creating solute atoms of separate species,  $\varepsilon_{sol}$  and  $\sigma_{sol}$ , with parameters ranging from values less than to greater than  $\varepsilon_{Cu}$  and  $\sigma_{Cu}$  respectively, they evaluated the effect of solute cohesive energy and size on  $H_{EX,GB+S}$ . They found that solute atoms with  $\varepsilon_{sol} < \varepsilon_{Cu}$  slightly lowered  $H_{EX,GB+S}$  compared to the pure grain boundary, and  $\varepsilon_{sol} > \varepsilon_{Cu}$  slightly raised  $H_{EX,GB+S}$ . However, any size of solute atom ( $\sigma_{sol}$ ) lowered  $H_{EX,GB+S}$ , with the larger solute providing a larger decrease in energy. They attribute this to a large decrease in lattice strain energy upon segregation to the boundary. For the atoms larger than Cu,  $\sigma_{sol} = 1.6, 2.0, 2.4, 2.8$ ,  $\Delta H^{SEG} = 1.12, 2.74, 4.01, 6.03$  eV, respectively.

In our system, Ag has a larger covalent radius than Cu with Sn, and both solute types have smaller radii than Sn. Also, the Cu-Sn alloy has a larger cohesive energy ( $E_c$ ) than Sn-Sn, and Ag-Sn, with Ag-Sn being the smallest. This is shown in *table 2-1*. From

Millett, et al.'s work, we can say that Ag's larger radius increases its tendency for boundary segregation, while Cu's greater cohesive energy decreases its tendency for segregation. However, our segregation enthalpies are significantly lower than those found in by Millett, et al. This is a result of the difference in size of their solute atoms compared to ours. As a consequence, more Ag or Cu atoms are required to reduce  $H_{EX,GB+S}$  to zero. Comparing the critical atom number ( $N_{A,CR}$ ) to the size of our system, for lower temperature Ag and all temperatures of Cu, the number of atoms in the boundary is approaching the physical limit for a single layer and at these amounts will undoubtedly have solute-solute effects that are not examined here.

An interesting contrast to the previous work, is a study by Namilae et al., where they investigate the energy of the Al (111)- $\Sigma$ 3 boundary energy in the presence of a substitutional atom of Mg. [83] They find that for this particular low energy twin boundary, the oversized Mg atom actually increases the excess energy. They explain that there is an unfavorable neighbor coordination at the boundary for Mg, and this energy increase is greater than the strain energy created by inserting Mg into a position in the bulk lattice.

### 5.2.3 Segregation Enthalpies from Experimental Diffusion Measurements

Two experimental studies by Divinski, et al. use low solute concentrations to measure solute grain boundary diffusivity and calculate segregation enthalpies for Ni in Cu and Ag in Cu via direct radiotracer measurement. [84][85] They show that atomic radius plays a major role in the magnitude of segregation enthalpy, but note there may be other causes for particular species. In a high temperature regime, the triple product  $P = s\delta D_{GB}$

is the measured value of diffusivity in the boundary, where  $s$  is the solute segregation factor,  $\delta$  is the grain boundary width, and  $D_{GB}$  is the grain boundary diffusivity.

Assuming  $\delta$  is constant, measuring diffusivity again in a low temperature regime, where all diffusion takes place in the boundary and  $D_{GB}$  can therefore be measured directly, the authors determine the temperature dependence of  $s$ . Here,  $s$  follows an Arrhenius dependence as  $s = s_0 \exp(-H_S/RT)$ , and  $H_S$  is the segregation factor of the solute. They determine the value of  $H_S = 0.40(4)$  eV for Ag in Cu and 0.176 eV for Ni in Cu, and also report another study of Bi in Cu, where  $H_S = 0.552$  eV. Compared to Ni, Ag and Bi have larger atomic radii, and Bi is said to have the largest segregation enthalpy among solutes studied for Cu. It is obvious the strain introduced by the solute atoms plays a role in  $H_S$  at the experimental level as well. However, in the case of Bi and Ag, solute atoms with a radius larger than the solvent produce segregation enthalpies on the order of 0.4 to 0.5 eV, significantly lower than values from Millett et al.'s work. The authors also mention that a cited solute study for Au, which has a significantly larger radius than Ni and is comparable to Ag, determined the Au segregation enthalpy in Cu to be less than that of Ni.

#### 5.2.4 Discussion of Experimental Behavior

Thus far, when comparing both experimental segregation enthalpies and those computed in this work, to Millett et al.'s from separate investigations of atomic size and cohesive energy, we can say that the combined effect of the size and interaction properties must be considered for  $\Delta H^{SEG}$  to be computed within a reasonable order of magnitude. It is important as well to visit the idea that other factors can influence the driving force for

boundary segregation. The authors in the previous experimental work in refs. [84] and [85] stress that thermodynamics plays a role in segregation. Clearly a thermodynamic description of the system should consider more than atomic size and cohesive energy, and does so based on theory developed by Gibbs and McLean included in Section 2.3.2. To this point, Kirchheim has shown that at certain concentrations, solute atoms can form a thermodynamic equilibrium state via a two phase system in which a precipitated phase exists with the solvent. [86] Seo et. al mention experimental evidence of this fact in their 2009 study. [79] As they increased the Ag content of their joints, the microstructure became finer. However, for Cu, all low concentration joints exhibited large  $\beta$ Sn grains and only slow cooling and high Cu concentration produced a fine microstructure. This microstructure was shown to exhibit many dendrites of  $\text{Cu}_6\text{Sn}_5$  intermetallic compound (IMC), thought to stabilize the Sn grains. Our work shows a lower preference for Cu to segregate into the (101) boundary when compared to Ag, most likely because of the smaller radius and higher cohesive energy. We also observe a decrease in  $H_{EX,GB+S}$  upon additions of both solutes, though greater for Ag because of the factors previously mentioned. Therefore, if the preserved fine microstructure of  $\beta$ Sn is a result of decreased grain growth by way of grain boundary stabilization, it is our belief that Ag addition stabilizes the boundaries, while for Cu at low concentrations, the solute is unable to effectively stabilize the boundaries. At higher Cu concentrations however, it is possible that a competing precipitation reaction between Cu and Sn is dominant, forming IMC within the grain boundaries.

Telang et al. also offer an explanation for the microstructure that results from Ag or Cu addition to Sn. [17] In their work, orientation imaging microscopy (OIM) was used to

characterize the types and distributions of  $\beta$ Sn grain boundaries in ingots, reflowed specimens, and solder joints, each containing different amounts of Ag and Cu. Here, they are able to identify the types of boundaries created between grains and show that there is a high frequency of “special” (low energy) boundaries. As Ag concentration increases, they observe a more uniform distribution of boundary types and accredit this to the boundary segregated Ag, effectively increasing the energy of the special boundaries and making them less likely to form during cooling. Similarly, they contend that Cu reduces the interfacial energy, increasing the likelihood of formation.

### 5.2.5 Special Boundary Simulations

Contrary to Telang, et al., we do not see any evidence of solute increasing the excess enthalpy of the (101) boundary, and as we have shown, Ag will lower the excess energy of the grain boundaries in a greater capacity than Cu for the same concentration.

Millett’s work with low energy LJ and Cu  $\Sigma 5$  boundaries supports this as well. As reported earlier however, the work by Namilaie, et al. introduces the idea that for some boundary-solute combinations, the enthalpy of segregation can be negative (in our context) and the solute will favor the bulk lattice. To test the validity of Telang’s et al.’s claims, we simulated solute loading in a (301) grain boundary, as well as two other medium energy boundaries. The (301) boundary was identified by Telang, et al. to persist in  $\beta$ Sn after annealing of the sample, and characterized as a “special” boundary. Solute additions were conducted at 300K and we computed the segregation enthalpies for Ag and Cu, shown in *table 5-4*. Also shown are the energies of the pure boundaries. These values indicate a very weak, yet similar preference for both Ag and Cu in the (301)

boundary, and the error suggests the possibility of bulk preference (a small increase in boundary energy upon segregation). For the other two medium energy boundaries, we see a reasonable preference for Ag and Cu segregation, when compared to experimental  $H_S$  values. Therefore, according to simulations with the MEAM potential, while the scenario that Telang, et al. state is statistically possible, all indications are that Ag and Cu only lower the energy of  $\beta$ Sn grain boundaries. We believe that the effect Telang, et al. were seeing was the Ag stabilization of non-special (medium and higher energy) boundaries, and consequently, the inability for the special boundaries to grow and consume the non-special boundaries. For Cu, at low concentrations, this solute cannot stabilize higher energy boundaries to the necessary degree, and therefore the solder joints with Cu exhibit  $\beta$ Sn grain growth of special boundaries. As we have shown, the effect of Ag and Cu on higher energy boundaries is much greater than the possible effect of solute on low energy “special” boundaries. According to experimental work and our simulation results, the (301) boundary is one of the lowest energy observed in  $\beta$ Sn. Accordingly, this boundary presents a good lower-limit by which to judge segregation effects.

**Table 5-4** Ag and Cu solute calculations of enthalpy of segregation ( $\Delta H^{seg}$ ) for various boundaries of  $\beta$ Sn at 300K. Error is a weighted least squares fit of  $H_{EX,GB+S}$  vs.  $I^{EX}$ .

<b>Boundary</b>	<b>(301)</b>	<b>(310)</b>	<b>(201)</b>	<b>(101)</b>
<b><math>H_{EX,GB,0}</math> (<math>10^{-2}</math> eV/Å<sup>2</sup>)</b>	0.8775	2.152	2.658	4.239
<b>Ag <math>\Delta H^{seg}</math> (eV/atom)</b>	0.12(9)	0.49(8)	0.44(8)	0.64(9)
<b>Cu <math>\Delta H^{seg}</math> (eV/atom)</b>	0.06(9)	0.54(8)	0.37(8)	0.45(8)

### 5.2.6 Boundary Under Shear Strain

Computing the energy change of a  $\beta$ Sn grain boundary upon solute addition with molecular dynamics provides some explanation as to the behavior of the material in experiment. After reflow of the solder joint, the microstructure must arrive at some thermodynamic equilibrium and the effect of solute amount on the boundary energy can be related to boundary stability. During device operation however, the solder joint is subject to electrical current and temperature gradients, adding more driving forces to the dynamics of the microstructure, resulting in an increase of stress on the joint. Here, we investigate interface behavior subject to shear strain with our (101)  $\beta$ Sn grain boundary containing Ag and Cu solute amounts of 25 and 50 atoms.

We begin this portion of our study by comparing the yield stress of our pure grain boundary under different constant shear rates. *Figure 5-4* shows this shear stress vs. shear strain behavior. Decreasing shear rates by an order of magnitude gives a near-linear behavior of yield stress vs. shear rate on a log/log plot. The post-yield behavior of the systems undergoing the two slowest shear rates,  $10^6 \text{ s}^{-1}$  and  $10^7 \text{ s}^{-1}$ , is similar—they both maintain a level of shear stress at about 100MPa. We note here that this level is considerably higher than experimentally measured values of yield stress. This discrepancy is discussed in the final paragraph of this section. Additionally, we conducted a “steady-state” simulation at the slowest shear rate of  $10^6 \text{ s}^{-1}$ . The label in *figure 5-4* points to a shear simulation where the strain was stopped and held at 0.0375, and the system was simulated for 2 nanoseconds. The flat line on the lowest curve indicates the system was at a steady state and maintained its stress level. The slowest shear rate pushes the limits of computational feasibility, with a shear strain of 0.12

requiring 144 hours using four CPUs of a *Quad-core 2.27GHz Intel Xeon L5520* "Nehalem" processor. We believe the increase in accuracy by reducing the shear rate 2-fold or 3-fold, following the trend in *figure 5-4*, is outweighed by the large increase in simulation time. As such, we use the slowest shear rate (outlined in Section 5.1) from this figure in the rest of this study.

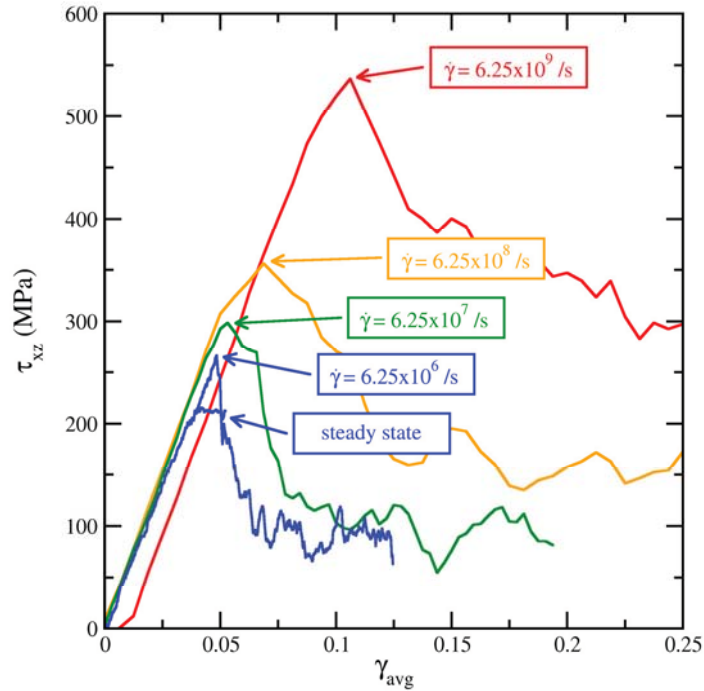


**Figure 5-4** Shear stress ( $\tau_{xz}$ ) vs. average strain ( $\gamma_{avg}$ ) for four strain rates at 300K. Curve labels point to yield stress in various shear strain rates, decreasing from top to bottom. Lowest label is stoppage of shear rate of  $6.25 \times 10^6 \text{ s}^{-1}$  at a strain of 0.0375, to simulate a steady state condition.

In *figure 5-5* we plot the shear stress vs. shear strain results for the pure grain boundary and two amounts of Ag solute in the interface for 300K and 450K. At 300K, the pure boundary exhibits the largest yield stress, followed by a large decrease (initial boundary slip) down to a steady shear stress of about 100MPa. Initial loading of 25 Ag atoms

causes the yield stress to drop slightly in comparison to the pure interface, yet it maintains an increased level of stress until a strain of about 0.07, where it drops to roughly 100MPa. For 50 Ag atoms, the yield stress is larger than for the 25 atom case, closer to the level of the pure boundary. This interface maintains its yield stress level for a larger strain, and slips slowly to a value of 100MPa. The curves at 300K for boundaries containing are averages of three runs with different initial configurations. We report only properties that are consistent among the these three. At 450K, the pure boundary and boundary containing 25 Ag atoms show various points of yield stress during shear strain to 0.06. A contrasting behavior is shown when 50 atoms of Ag are present in the boundary. The stress is now distinctly higher than the pure and 25 atom interfaces, and the interface exhibits near-elastic behavior up to its peak of about 134MPa.

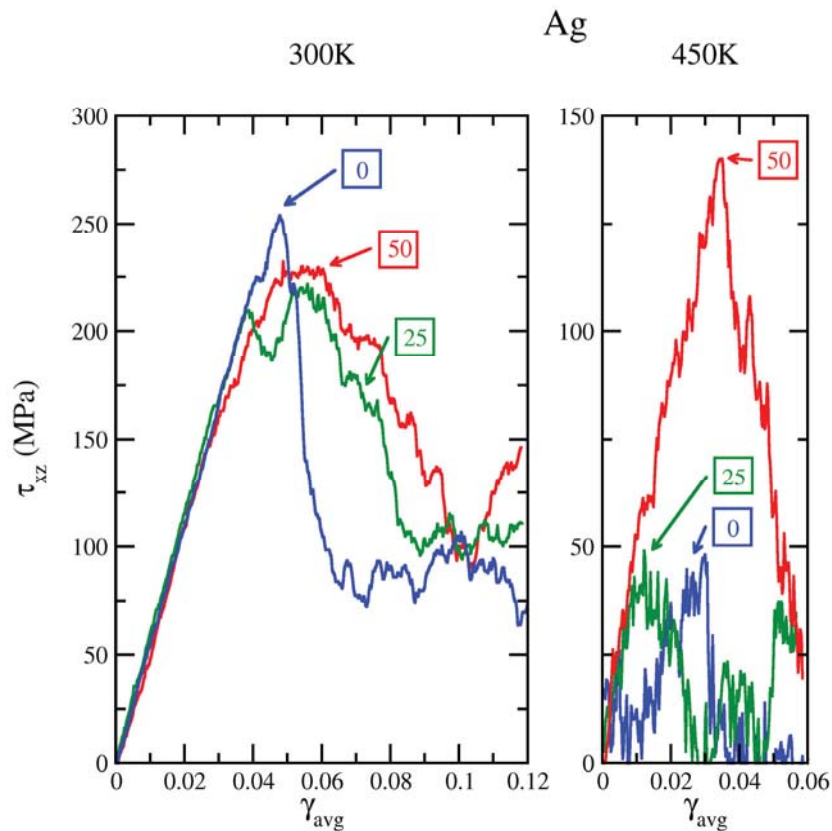


**Figure 5-5** Shear stress ( $\tau_{xz}$ ) vs. average strain ( $\gamma_{avg}$ ) for three solute amounts of Ag at 300K and 450K. Number in squares are solute atom amounts. Curves at 300K are the average of three independent simulation runs. Note different scales for 300K and 450K.

Many of the trends of Ag solute addition are present in the stress vs. strain plots of the boundary with Cu solute. In *figure 5-6* we plot the same shear stress vs. strain behavior of the pure boundary as was shown in *figure 5-5*. In the case of Cu at 300K, addition of 25 atoms at the interface causes the yield stress to drop, similar to Ag. We then see a large decrease at a strain of about 0.07. The stress state for 50 atoms of Cu is elevated until a strain of about 0.07, where it decreases to a level comparable to the other interface concentrations. At larger strain in *figure 5-6* it appears the interfaces containing solute are again increasing their level of shear stress as the strain increases. At 450K, the trends in stress vs. strain are comparable to the Ag solute case. We mention that while 50 atoms

of Cu also appears to increase the stress during shear strain, the level is significantly lower than the 50 Ag atom case from *figure 5-6*. There are also some small “shoulders” present in the increasing shear stress portion of the curve, possibly indicating various degrees of atomic rearrangement.

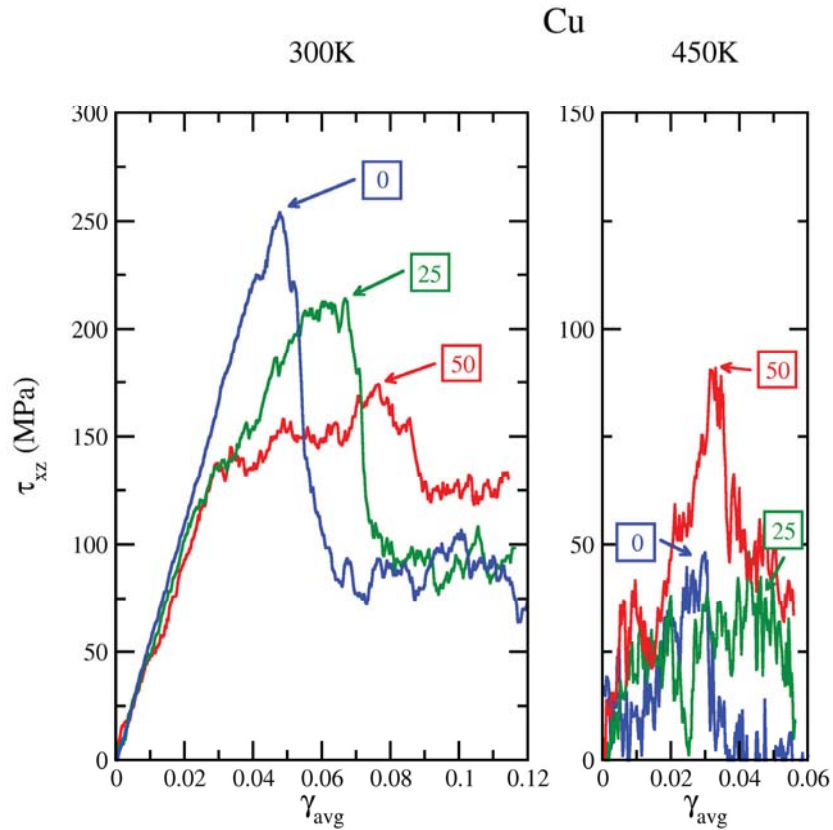


**Figure 5-6** Shear stress ( $\tau_{xz}$ ) vs. average strain ( $\gamma_{avg}$ ) for three solute amounts of Cu at 300K and 450K. Number in squares are solute atom amounts. Curves at 300K are the average of three independent simulation runs. Note different scales for 300K and 450K.

For both types of solute at 300K, the yield stress during boundary shear is lowered upon the addition of 25 solute atoms. However, a high level of stress is maintained for larger strains, compared to the pure boundary. After initial slip, shown as a rapid decrease in

stress in *figure 5-5* and *figure 5-6*, all of the interface stress levels dropped to about 100MPa, with the exception of 50 Cu atoms which fall to about 125MPa. At the higher temperature of 450K, addition of 25 atoms of solute may increase the elasticity of the boundary, if only slightly, compared to the pure case. With 50 atoms at the interface however, the shear stress is markedly higher and the boundary now exhibits elastic behavior. In this case, Ag addition provides a larger yield stress than Cu.

For pure Sn, the experimental value for the shear modulus is given as 17.804 GPa. This is computed by Adams from an average of the single-crystal elastic constants. [87] In our simulations, the slope of the linear elastic regions of *figure 5-5* and *figure 5-6* show a modulus for the (101) grain boundary of 5.605 GPa. Discrepancies in these values are likely caused by two factors. The first is a possible weakness in the interatomic potential. Ravelo and Baskes note an under predicted elastic constant  $C_{44}$  for  $\beta$ Sn by MEAM when compared to experiment. They also find the  $C_{33}$  constant (lattice *c-direction*) is slightly smaller (softer) than the  $C_{11}$  constant (*a-direction*), when experimentally it is shown that  $C_{33} > C_{11}$ . However, both MEAM values are larger than experiment. [21] Second, in measuring the shear modulus, we obtain a value for shear in the [010] lattice direction along the (101) plane, which is compared to an average value computed from experimental elastic constants. Basaran and Jiang reported that elastic and shear modulus measured values reported in the literature vary significantly. [88] It is therefore not surprising that the single-crystal average differs from our calculated value for a specific lattice direction.

### 5.2.7 Boundary Sliding in Solute Segregated Boundaries

Simulation work by Qi, et al. investigates the effects of applied force on the sliding of several grain boundaries. [89] For molecular dynamics simulations of aluminum at 750K, they calculate the critical level of shear stress necessary for sliding to occur, by varying the magnitude of shear force used. The authors show that for boundaries with higher excess energy, they observe a lower critical stress value, and an increase in grain boundary sliding. Namila, et al. compute static energies of Al grain boundaries and corresponding amount of slip when under shear. [83] Similarly, they show for higher energy boundaries, the sliding amount is greater. Previous work by the current authors quantified the energy of the (101)  $\beta$ Sn grain boundary and various others using molecular simulation. [80] The (101) boundary had the highest energy (and highest self-diffusivity) relative to the other boundaries investigated, and from comparison to other work, we can say that the pure (101) boundary will most likely exhibit the largest amount of sliding and lowest yield stress when compared to the other boundaries studied in ref. [80].

Investigations of sliding resistance by Millett, et al. find a decrease in the excess energy of the grain boundaries upon solute addition, and a corresponding resistance to sliding. [90] In Millett, et al.'s 2006 work, the effect of both interstitial and substitutional atoms were investigated. It was found for low energy (310)- $\Sigma$ 5 boundaries and higher energy boundaries, interstitial atoms and oversized substitutional atoms hindered sliding, while undersized substitutional atoms increased sliding for the higher energy boundary. From this, they note a correlation between enthalpy of segregation of the solute species and sliding resistance. Solute that is strongly segregating will aid in sliding resistance.

Results of our Ag and Cu additions into the (101) boundary follow this to some extent. Initially, the yield stress is lower for the interfaces containing 25 atoms of solute compared to the pure boundary, so these boundaries will begin sliding at a lower critical stress (in the context of Qi, et al. [89]). After leaving the elastic regime however, a high stress is maintained for those interfaces containing 25 and 50 solute atoms. This indicates a higher resistance to sliding at larger strains in comparison to the pure boundary.

### 5.2.8 Interface Structure During High Temperature Sliding

Taking a closer look at their *sliding displacement vs. time* plots, Qi et al. discuss a change from a linear to parabolic slope as the force changes. [89] The authors attribute this change to an increase in atomic disordering at the interface, where a parabolic slope is created by a large shear force perturbing the boundary region and increasing the atomic mobility. As the applied shear force increases, the mobility of the atoms at the interface increases.

Our pure boundary undergoes a similar transition at 450K, as time progresses during our constant shear velocity simulation. Initially, the interface becomes disordered over a 10-15 Å width that is perpendicular to the interface. This is followed by coexisting regions of ordered planes of atoms and mobile pocket of disordered atoms, maintained until a strain of about 0.04. At this point, there is a transition into a structure that envelopes the entire interface plane. The new phase in the interface, which is five atomic layers thick, slides relative to the  $\beta$ Sn lattice on planes above and below it, as shear progresses. This final structure is illustrated in *figure 5-7*. Here, the blue and red colored planes are those

of the new structure that has formed at the grain boundary interface. In *figure 5-7-3*, we provide a top view of the atoms in the new structure, as well as the planes separated. In the three parts of the figure we have highlighted the presumed lattice structure in green. As it is shown, the structure is a tetragonal body-centered lattice with x and y lengths equivalent, and z length larger than the other two. This is a deviation from  $\beta\text{Sn}$ 's tetragonal lattice, where the z length is shorter than x and y. We examined the normal stresses of the simulation box in an attempt to verify if the lattice at the interface was under compressive stress in a particular direction or tensile stress in a direction. Compressive stresses in x and y directions would indicate deviation from the  $\beta\text{Sn}$  structure, as would tensile stress in the z direction. However, stresses in x and y were opposite of each other, and the z direction was under compression.

In the hopes of maintaining bounds on the scope of this work, we will simply offer the notion that the many-body nature of the potential along with the specific strain distance in the x-z direction aided in the formation of this secondary phase. After formation, it is maintained throughout the duration of the simulation and provides a low stress slip plane for the (101) boundary. Interfaces containing solute do not exhibit this secondary phase formation, and subsequently offer an increased resistance to sliding.

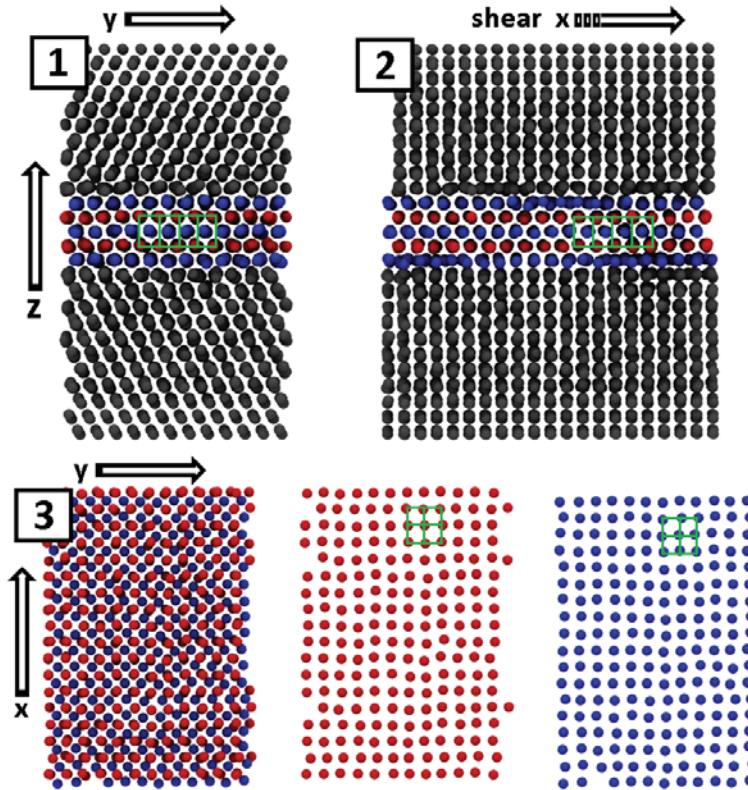


**Figure 5-7** Structural formation in pure GB interface at 450K under shear. (1) Side view in y-z plane. (2) Side view in x-z plane, shear direction indicated. (3) Top view of full BCC structure and separate lattice planes.

## 5.3 Conclusions

We investigated the excess enthalpy of the  $\beta$ Sn (101) grain boundary containing various amounts of Ag and Cu solute atoms, as well as its behavior under shear strain. It is shown that an increase in either type of solute at the interface lowers the excess enthalpy of the grain boundary. We then find the enthalpies of segregation for both solute types, computed as the slope of excess enthalpy of the grain boundary per area vs. interfacial solute concentration per area. Under constant shear strain, addition of solute lowers the

yield stress of the boundary, but for larger strain, stress levels are maintained when compared to the pure case.

For Ag solute, we find it has a greater driving force for segregation and thus lowers the excess energy of the boundary more than Cu for a given number of atoms for the (101) boundary. Experimental works from other authors discuss the change in microstructure for different amounts of solute in Sn-*x*Ag and Sn-*x*Cu solder joints in the context of Ag addition aiding in destabilizing special boundaries, and high concentration Cu addition forming Sn-Cu IMC and pinning  $\beta$ Sn grains. In regards to Ag, we observe only a reduction in excess grain boundary enthalpy, showing the beginnings of (101) interface stabilization. A short investigation of the (301) and two medium energy boundaries found very low, but positive, segregation enthalpies for Ag and Cu in the special boundary, and experimentally comparable segregation enthalpies for the (310) and (201) boundaries. However, considering the statistical uncertainty in the (301) results, these values indicate that an increase in that particular boundary excess energy is possible. We do find one experimental case where a  $\Sigma 3$  boundary's energy increased upon Mg addition, however numerous experimental works show solute atoms stabilizing grain boundaries, both low and high energy, as indicated by the solute's positive enthalpies of segregation (in our context). To completely rule out the possibility of "destabilization" by Ag solute however, more specific investigations should be carried out.

Cu and Ag solute both affected the behavior of the (101) boundary under constant shear strain. At 300K, the pure boundary exhibited the highest yield stress. Interfaces with either Ag or Cu however, maintained a high level of stress after yield, followed by a

quick decrease in stress to a value similar to that of the pure boundary. High temperature shear brought about almost no stress response from the pure boundary, and the initially disordered interface underwent a structural transition into a tetragonal body centered structure at long simulation time. With solute addition however, the boundary disordered less and showed no structural transitions. Large solute concentrations evoked elastic behavior from the boundary under shear, and yield stress values were about 50% and 25% of the 300K case, for Ag and Cu respectively. Overall, Ag and Cu solute addition at low and high temperature restricts  $\beta$ Sn (101) grain boundary sliding, evidenced by elevated values of stress at larger strains.

# Solute Effects on Grain Boundary Self-Diffusivity

*“And it must follow, as the night the day...”*

Continuing the investigation of transport in microcrystalline and polycrystalline  $\beta$ Sn, in this chapter we measure the self-diffusivity of Sn in a (101) symmetric tilt  $\beta$ Sn grain boundary containing various amounts of Ag and Cu solute. Using the Modified Embedded-atom method as an interatomic potential, we are able to quantify the effect that Ag and Cu have on the grain boundary self-diffusivity of Sn at typical solder operating temperatures. Additionally, we determine the effect solute has on the diffusive width of the grain boundary and offer insight into the unique characteristics of the grain boundary resulting from the two types of solute.

Underscoring the importance of determining, not only transport properties of the joint solvent material, but also the effects of dopants or solute additions on transport, is the experimental work by Bernardini, Gas, et al. [91] In their 1982 work, they observe a decrease in the self-diffusivity of Fe as Sn solute atoms strongly segregate to the grain boundary. Molecular simulation is well suited to complement this type of study.

Preliminary work using simple model systems has shown the effects of substitutional dopant atoms on Cu grain boundaries and in Cu polycrystals. [48] Although these studies approximate quantities such as excess entropy through the use of McLean's model and extensions, atomistic detail of concentrations and transport for particular structures can be measured. [44][80]

This chapter continues with specifics of our molecular simulations in Section 6.1. We then present and discuss our findings in Section 6.2, and end with concluding remarks in Section 6.3.

## 6.1 Simulation Details

In our simulations, and similar to Chapter 5, we model the (101) symmetric tilt grain boundary of  $\beta$ Sn, with varying amounts of solute particles randomly placed in interstitial positions along the interface. The grain boundaries and randomly inserted solute configurations are again constructed with the Etomica Molecular Simulation API, and for solute species we use Ag and Cu. [76] Interactions between Sn and Ag, and Sn and Cu are modeled with MEAM in the LAMMPS Molecular Simulator. [58][70] We follow the same system setup as in Chapters 4 and 5, and a similar equilibration setup which we explain in the following.

**Table 6-1** Ag and Cu solute quantities and corresponding excess interfacial density.

$N_s$ (atoms)	5	10	25	50
$\Gamma_s$ ( $10^{-3}$ atoms/ $\text{\AA}^2$ )	2.085	4.171	10.43	20.85

The process of minimization of the grain boundary is done in three steps. First, near 0K the two grains move independently in x, y, and z-directions via molecular dynamics, their respective atoms all having the same average force each time step. This step is shown in (figure 6-1-1). Next, solute atoms are randomly inserted at interstitial positions in the grain boundary interface. Shown in table 2 are the specific amounts of solute inserted and their corresponding interfacial excess density. The positions of the solute atoms are then adjusted via a conjugate gradient energy minimization, while holding the Sn atoms fixed (figure 6-1-2).

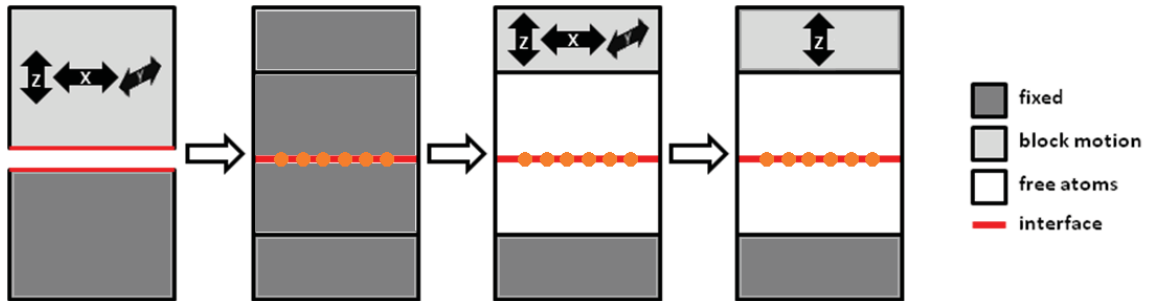


**Figure 6-1** (1) minimization (MD near 0K), (2) solute minimization (conjugate gradient), (3) equilibration, (4) production structures. Black arrows indicate direction of motion of the block portion. Free atoms are movable in x, y, and z directions. Actual simulation cells are 3-dimensional and periodic in x and y directions.

Finally, once a minimum energy structure is found, the system is then equilibrated using molecular dynamics (MD) at the desired production run temperature (figure 6-1-3).

Here, atoms in the bottom grain within twice the potential cutoff distance of the bottom edge of the structure are fixed and atoms in the top grain within twice the potential cutoff distance of the top edge of the structure are given an average force in the x, y, and z-directions. This creates a floating boundary at the top of the box and allows the system to reach an average pressure of zero over 100 picoseconds. Following these steps, the floating boundary is fixed and the grain boundaries are simulated with MD between 9 and 15 nanoseconds (*figure 6-1-4*). All molecular dynamics is carried out with a *Nose-Hoover* thermostat (NVT) and a time-step of 0.001 picoseconds.

## 6.2 Results and Discussion

Using MD over a range of temperatures, we simulate the (101) symmetric tilt grain boundary of  $\beta\text{Sn}$ . At each temperature, specific quantities of solute atoms of Ag and Cu are randomly inserted at the grain boundary interface and the width-scaled Sn self-diffusivity is calculated. We also analyze the planar self-diffusivity profiles in the direction perpendicular to the grain boundary interface. From this we can quantify the interface's diffusive width  $\delta_{\text{GB}}$  and characterize the effect that Ag and Cu have on the interface structure of  $\beta\text{Sn}$ .

### 6.2.1 Grain Boundary Width-Scaled Diffusivity ( $\delta_{\text{GB}}D_{\text{GB}}$ ) of Sn

We compute the mean-squared displacement of Sn for multiple MD runs at a given temperature and specific solute concentration. By employing *equation (2-24)* from Section 2.2.3, we plot the width-scaled diffusivity vs. temperature in *figure 6-2* for each type of solute over a range of quantities and temperatures. For Ag and at low

temperatures, the diffusivity of Sn does not exhibit any type of clear trend with increasing solute concentration. Statistically, the points at 300K and 350K are very close in magnitude. However, as the temperature increases, we see the Sn diffusivities for specific solute amounts begin to deviate. At 450K, the diffusivity for a system with 50 solute atoms is decreased by an order of magnitude when compared to the 5 solute atom system and by about one-third when compared to the 25 solute atom system. With the addition of Cu instead of Ag, the trends are similar but less pronounced. We see a smaller deviation in the diffusivity of Sn at higher temperatures with respect to solute concentration—about twice the diffusivity at 5 atoms than at 50 atoms. In contrasting the two solute types, the addition of 25 and 50 atoms of Ag lowers the diffusivity of Sn more than similar quantities of Cu. For small numbers of solute, the effect of Ag and Cu are statistically similar on this width-scaled diffusivity plot.

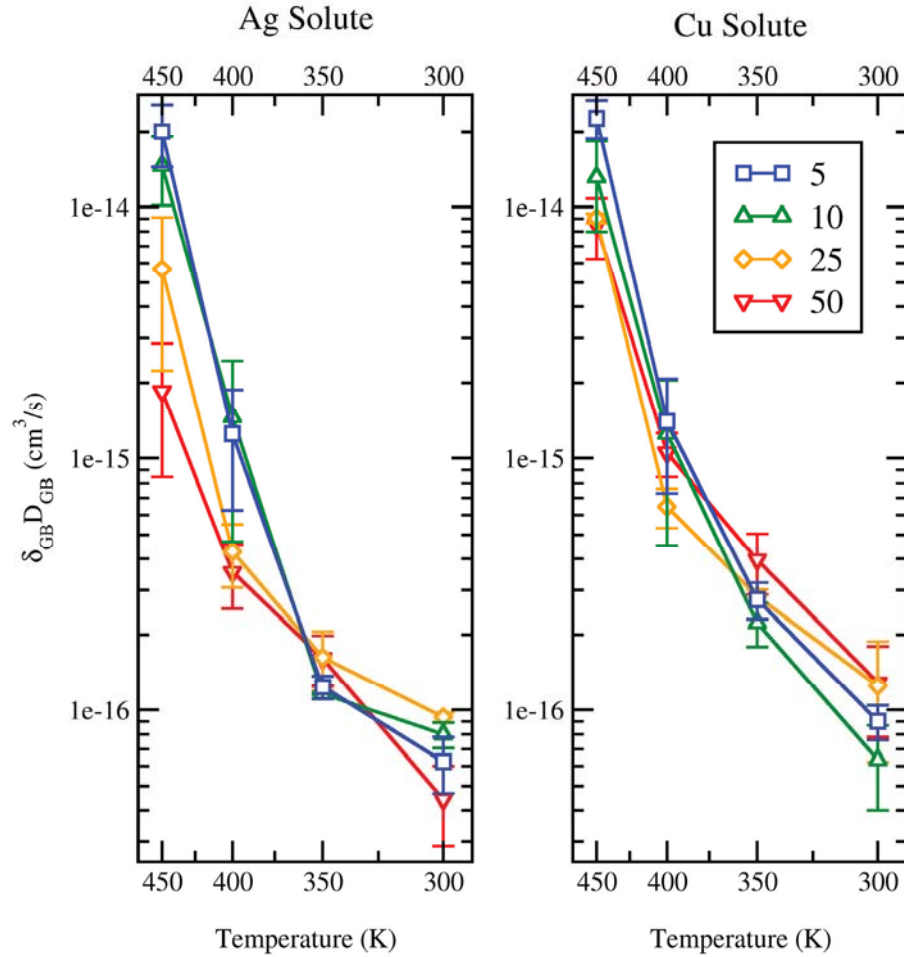


**Figure 6-2** Width-scaled self-diffusivity of Sn vs. temperature for various solute atom quantities. LEFT is Ag solute, RIGHT is Cu solute. Error bars are standard deviation from three or more simulation runs.

## 6.2.2 Planar Self-Diffusivity Profiles and Interface Width

For a closer look at the diffusive properties of Sn and an opportunity to investigate its interface structure, we plot the planar self-diffusivity in planes parallel to the grain boundary interface. For clarity in the plots in *figure 6-3* and *figure 6-4*, only profiles from a single run are plotted, however, the single run chosen was the one with a diffusivity closest to the average. Also, note the change in scale on the plots' y-axes.

The profiles for varying Ag amounts at temperatures of 300K, 350K, 400K, and 450K are

shown in *figure 6-3*. Similar to *figure 6-2*, at temperatures of 300K and 350K the authors are unable to discern any trend in diffusivity when increasing solute amount. Although at 300K, the profiles show a decrease in diffusivity when increase solute amount from 5 atoms to 10, and from 5 atoms to 50, the same does not hold true for profiles at 350K. At 400K and 450K, the effect of solute on Sn self-diffusivity is clearly evident and is amplified as temperature increases. Widths of the profiles remain relatively stable as temperature increases and as solute increases.

A similar analysis is completed for Cu solute in the  $\beta$ Sn grain boundary and illustrated in *figure 6-4*. Again, the scales of the plots y-axes vary with temperature, but are equivalent to those in *figure 6-3* at specific temperatures for the sake of comparison. In *figure 6-4*, the effect of Cu solute on the self-diffusivity of Sn with increasing solute amount occurs at 350K and continues to high temperature. The effect of specific solute concentrations on diffusivity becomes more distinct as temperature increases. As solute concentration is increased, we see in an increase in diffusive width at all temperatures, with the increase at 450K being the least prominent. Additionally and perhaps most importantly, the interface diffusivity profiles exhibit a change from a single peak at 5 and 10 atoms of Cu to double peaks at 25 and 50 atoms of Cu.

Further evidenced by the planar diffusivity profiles in *figure 6-3* and *figure 6-4* is the effect of solute on Sn self diffusivity. Both Ag and Cu decrease the planar diffusivity in the (101) grain boundary at temperatures at 400K and above, although the effect of Cu is seen at 350K. It is shown here however, that Ag plays a larger role. At 350K and 400K, peaks in the diffusivity of the Ag system are significantly lower than systems with Cu, for

corresponding temperatures. In the comparison of  $\beta$ Sn's structure for different solute types, we see no qualitative difference in interface width with temperature for Ag as solute, but for Cu, it is apparent that the interface width grows with increased solute amount and the diffusive profile changes shape at large solute amounts. The center of the  $\beta$ Sn grain boundary interface containing Cu exhibits slower diffusion than at the edges of the interface containing no Cu. To further characterize this behavior we quantify the interface width at a range of temperatures for various solute concentrations, as well as inspect simulation snapshots and trajectories.

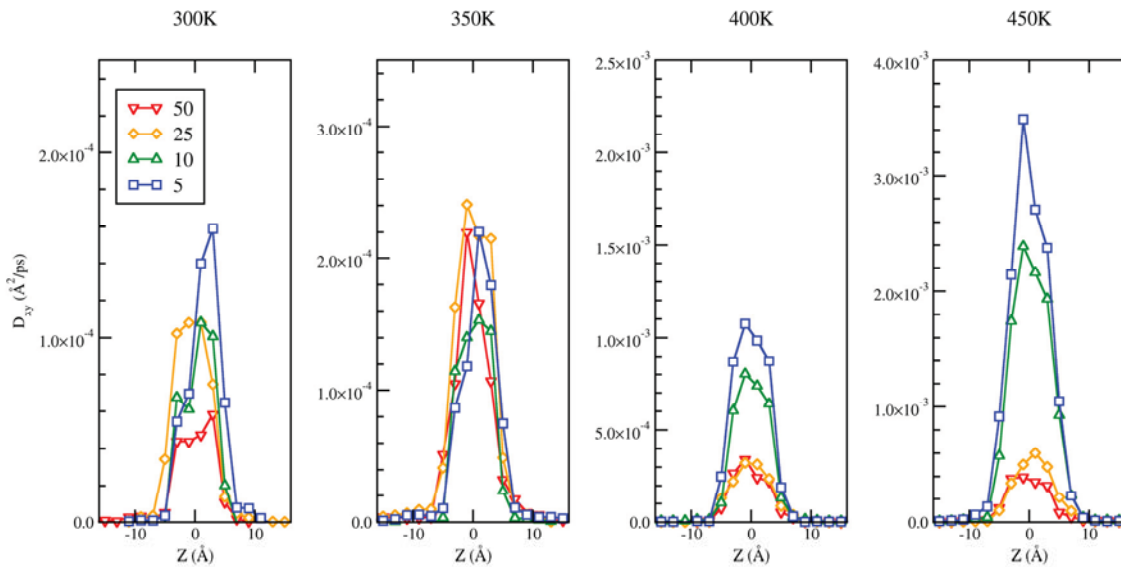


**Figure 6-3** Planar self-diffusivity profiles in z-direction of Sn for various solute atom quantities of Ag at a particular temperature. Note different scales on each ordinate.

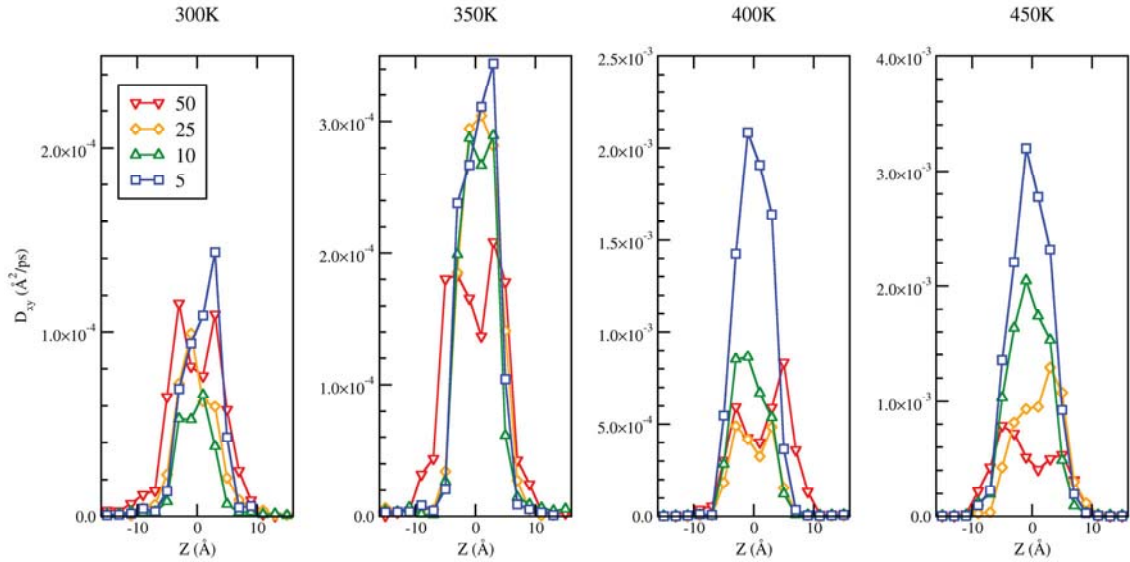


**Figure 6-4** Self-planar diffusivity profiles in z-direction of Sn for various solute atom quantities of Cu at a particular temperature. Note different scales on each ordinate.

An analysis of the *full-width at half maximum* of the planar self-diffusivity profiles in *figure 6-3* and *figure 6-4* is shown in *figure 6-5*. Here, we quantify the diffusive width of the (101) grain boundary interface with varying solute amount at a range of temperatures. It is important to mention that the analysis assumes a profile that is Gaussian-like, yet width computation from our profiles of the  $\beta$ Sn interface with large amounts of Cu solute deviate from this. In our analysis of these profiles, the maximum is taken as the highest peak of the two. This introduces the possibility to skew or induce spurious width determinations for very high peak and very low "trough" regions. However, the profiles in our case exhibit only moderate dips in diffusivity over the range of x-y planes, and it is unlikely that this affects the width measurements in such a manner.

At *figure 6-5 - LEFT*, it is shown that diffusive widths for the (101) interface containing Ag increase very little with solute concentration and temperature. In comparison to a

pure  $\beta$ Sn interface (shown as black circles), the width has decreased by at most 1 Å with the addition of Ag solute. As Cu is inserted at the interface (*figure 6-5 - RIGHT*), an increase in interface width with temperature is more obvious, as is the increase in width with solute amount. At 25 and 50 Cu atoms in the interface, the width of the (101) grain boundary exceeds the pure boundary width for temperatures above 300K. There is also a marked difference in widths between Ag and Cu at solute amounts of 50 atoms. The amount of Ag solute seems to have no effect on the width, while the addition of Cu causes a distinct increase in width.

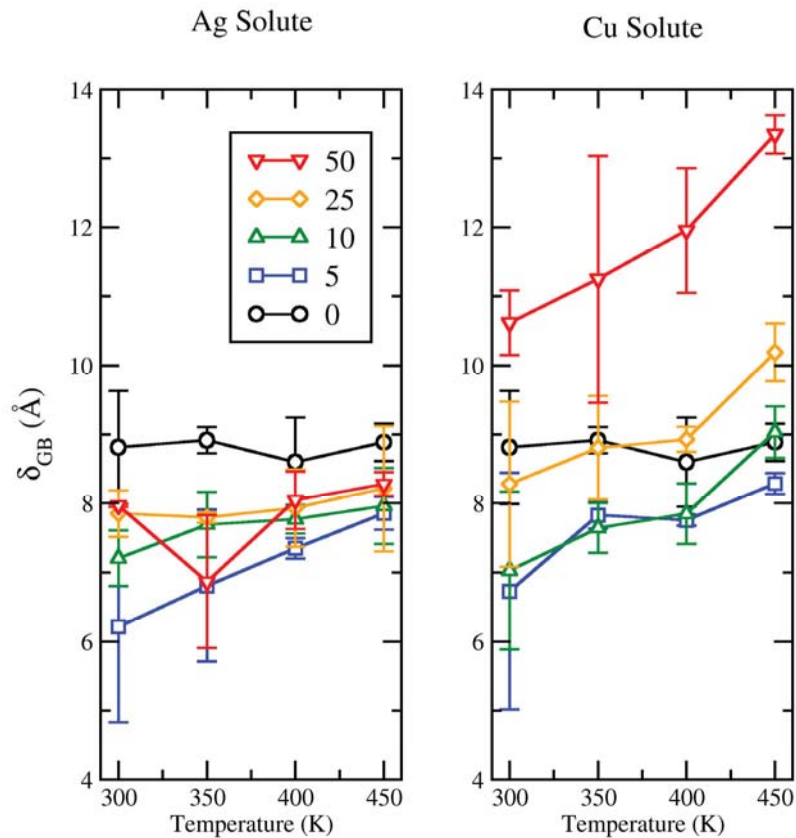


**Figure 6-5** Diffusive width vs. temperature for various solute concentrations. LEFT is Ag and RIGHT is Cu. Circle points (black) are the pure  $\beta$ Sn grain boundary widths.

We have shown thus far that the addition of both Cu and Ag decrease Sn self-diffusivity in the (101)  $\beta$ Sn grain boundary. Separately, Ag reduces the diffusivity more than Cu and promotes a smaller diffusive width of the grain boundary. With Cu addition, small amounts of solute give the same effect on diffusivity as Ag addition, but as the Cu amount is increased to 25 and 50, the grain boundary width grows larger than that of pure  $\beta$ Sn. Evidence of this is shown in the planar diffusivity profiles for  $\beta$ Sn with Cu added. At values of 25 and 50 atoms of Cu, we see wide profiles with two peaks in diffusivity, indicating a slower diffusing plane of the interface, sandwiched by two fast diffusing planes. We attempt to describe this behavior through the visual analysis of rendered simulation trajectories of both Ag in  $\beta$ Sn and Cu in  $\beta$ Sn. In *figure 6-6* we show a rendered snapshot of Ag in the (101) grain boundary (*LEFT*) and Cu in the boundary (*RIGHT*). These shots are taken from a simulation run at 450K, both containing 50 atoms of respective solute. It is evident that the amount of disorder in the system containing Ag is less than in the system containing Cu. This observation can explain the difference in diffusive widths of the two systems. A more ordered interface will be less mobile and exhibit a lower value of diffusivity.

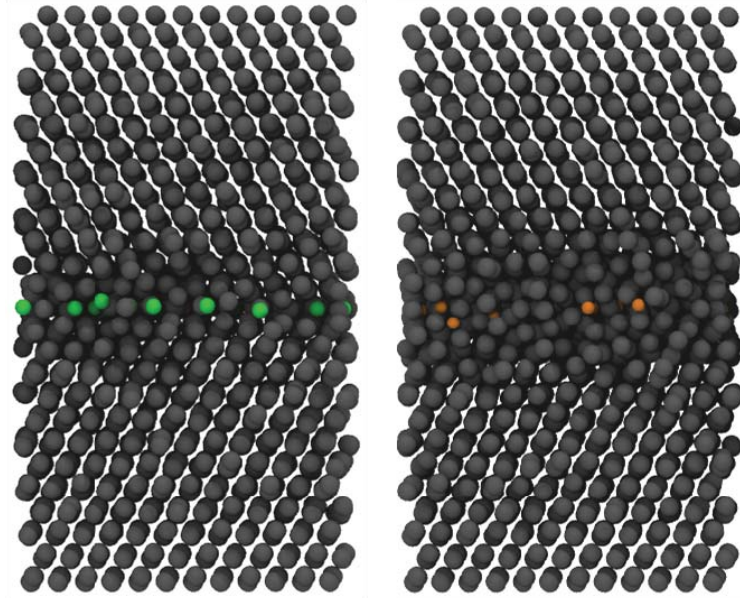


**Figure 6-6** Rendered simulation snapshot of two grain boundaries at 450K and containing 50 solute atoms in the interface. LEFT is Ag (green) and RIGHT is Cu (orange).

### 6.2.3 Effect of Atomic Size and Cohesive Energy

With a focus on the system with Cu added, the full trajectory (of which *figure 6-6* is a snapshot) shows that the Cu atoms maintain their  $z$ -axis position at the center  $x$ - $y$  plane of the interface. This plane corresponds to the "troughs" seen in *figure 6-4* profiles at higher solute concentration. Yet, only part of the interface behavior is described by Cu's  $z$ -axis position, and still unexplained are the highly mobile regions of  $\beta$ Sn in planes above and below the Cu solute. For this, further analysis of the trajectory was necessary. In observing the Cu solute atom's subtle motion in the central  $z$ -plane of the interface, we notice a preferred coordination of Sn around the Cu atom. Motion of the Cu atom is actually a concerted motion of a Cu and 4-Sn cluster.

A coordination similar to that of Cu is not seen for the other solute, Ag. This preference is described in a fairly straightforward manner by comparing the cohesive energies used in the MEAM potential, listed in *table 2-1*. We remind the reader, as mentioned in Chapter 5, Sn-Sn interactions carry a cohesive energy of 3.08eV, Ag-Sn is lower at 2.83eV, and Cu-Sn is higher at 3.5eV. At the interface, Sn-Sn interactions are preferred over Ag-Sn, while Cu-Sn interactions are favored over Sn-Sn. The larger cohesive energy of the Cu-Sn system is shown in the simulation trajectories to induce local ordering in the interface, which at larger distances creates disordering when in contact with the  $\beta$ Sn lattice. For an interstitial Cu in the bulk  $\beta$ Sn lattice, the quality of the surrounding  $\beta$ Sn structure may keep the preference for Cu-Sn ordering at bay. Conversely, when Cu is present at the grain boundary, the already low-coordinated Sn atoms are free to rearrange and form clusters with Cu. It appears these clusters are not structurally compatible with the  $\beta$ Sn lattice and create more disorder at the grain boundary. As such, the cohesive energy of Cu-Sn interactions actually increases diffusivity with respect to a Ag solute through the secondary effect of structural disruption at the interface.

Further comparison of the MEAM properties of Ag, Cu, and Sn, reveal that equilibrium values of the reference structure lattice constants  $r_0$  vary as well. For analysis in this work, values of  $r_0$  can be thought of as corresponding to relative atomic size—here Cu is smaller than Ag, and both are smaller than Sn. Because there is variation in both cohesive energy and size of the solutes, we cannot say definitively what effect the larger size of Ag has on the decreased mobility of Sn in the (101) interface. Nevertheless, other works have investigated the separate effects of atomic size and cohesive energy

mismatch. We again highlight the work by Millet, et al., referenced in Chapter 5, on the role dopant atoms play in grain boundary energetics and overall stability of nanocrystals. [46] In a 2005 investigation, they examined the effect of Lennard-Jones dopant particles—over a range of sizes and cohesive energies ( $\sigma$  and  $\epsilon$ )—on grain boundary energy. They demonstrated that while the overall contribution of a dopant atom's cohesive energy does not play a significant role in decreasing the energy of the solvent grain boundary, the size of the dopant atom as compared to the host atom is influential in affecting the energy. This is explained by a reduction of tensile stress at the grain boundary through the insertion of a dopant atom. Furthermore, for sizes of the dopant ranging from smaller than the host atom to larger than the host atom, the larger the dopant, the greater the decrease in grain boundary energy. In our case, one can equate a grain boundary energy with a grain boundary diffusivity by referring to both empirical relationships and trends observed in simulation. [30][80][92] Accordingly, we can say that the size of Ag plays an important role in the reduction of the self-diffusivity of Sn, as a result of a reduction in grain boundary energy.

A final comparison of the two solutes at high concentration is made in *figure 6-7*, where for 50 atoms of corresponding solute, we show planar diffusivity profiles at a range of temperatures. Noting the different scales on the plots' y-axes, it is shown that at temperatures of 400K and 450K, diffusivity is exceptionally hindered by Ag when compared to Cu. Again we see evidence of Ag's greater reduction in Sn self-diffusivity at the grain boundary versus Cu, here at similar concentrations. Still, whether this an effect of atomic size or decreased cohesive energy, we cannot state conclusively.

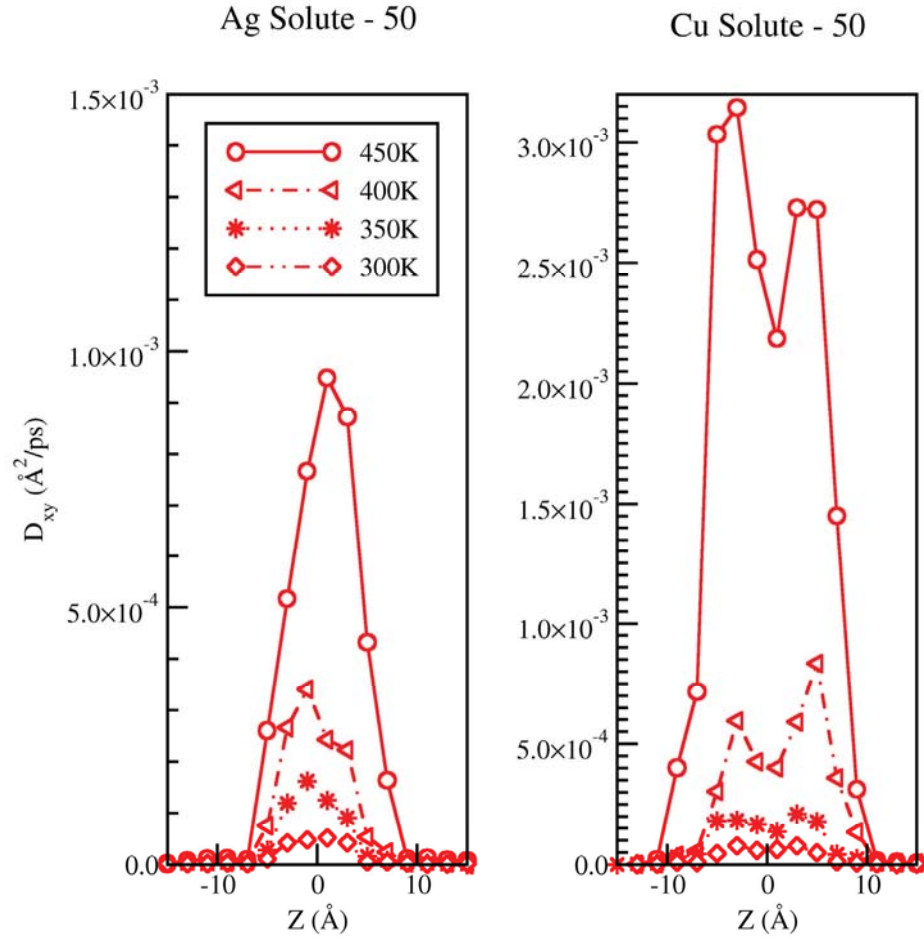


**Figure 6-7** Self-planar diffusivity profiles of  $\beta$ Sn in z-direction for solute atom quantities of 50 at various temperatures. LEFT is Ag and RIGHT is Cu. Note different scales on ordinate.

#### 6.2.4 Grain Boundary Self-Diffusivity ( $D_{GB}$ ) of Sn

After the direct calculation of grain boundary widths from plots in *figure 6-3* and *figure 6-4*, we can resolve the true grain boundary self-diffusivity of Sn, namely  $D_{GB}$  in units of length<sup>2</sup>/time. In doing so we have removed the effect of the interface width on the magnitude of the diffusivity. Specifically, we have normalized the quantity  $\delta_{GB}D_{GB}$  at various temperatures and solute amounts by the corresponding grain boundary width  $\delta_{GB}$  at the same conditions. This is shown in *figure 6-8*. In comparison to *figure 6-2*, low

temperature values of  $D_{GB}$  for the system with Ag added show very little change relative to  $\delta_{GB}D_{GB}$ , and at higher temperatures the relative magnitudes of  $D_{GB}$  are separated by a slightly larger amount. For Cu, low temperature diffusivities have collapsed to a smaller range of values for varying solute concentration. At temperatures of 400K and 450K, solute amounts of 25 and 50 show a greater deviation from amounts of 5 and 10.

Removing any variation of grain boundary width with temperature or solute concentration, allows us now to speak definitively about possible changes in diffusion rates or mechanisms of Sn. While there is a reduction in the magnitude of diffusivity with increased solute concentration, there is not a clear change in slope in these Arrhenius style plots. Therefore, we can say that the addition of Ag and Cu in low amounts influences the number of diffusive events, but does not affect the mechanisms of diffusion. For a mobile boundary like the (101) in  $\beta$ Sn, this is not surprising, and the interface may require larger solute concentrations or precipitation effects for it to exhibit a change in mechanism style.

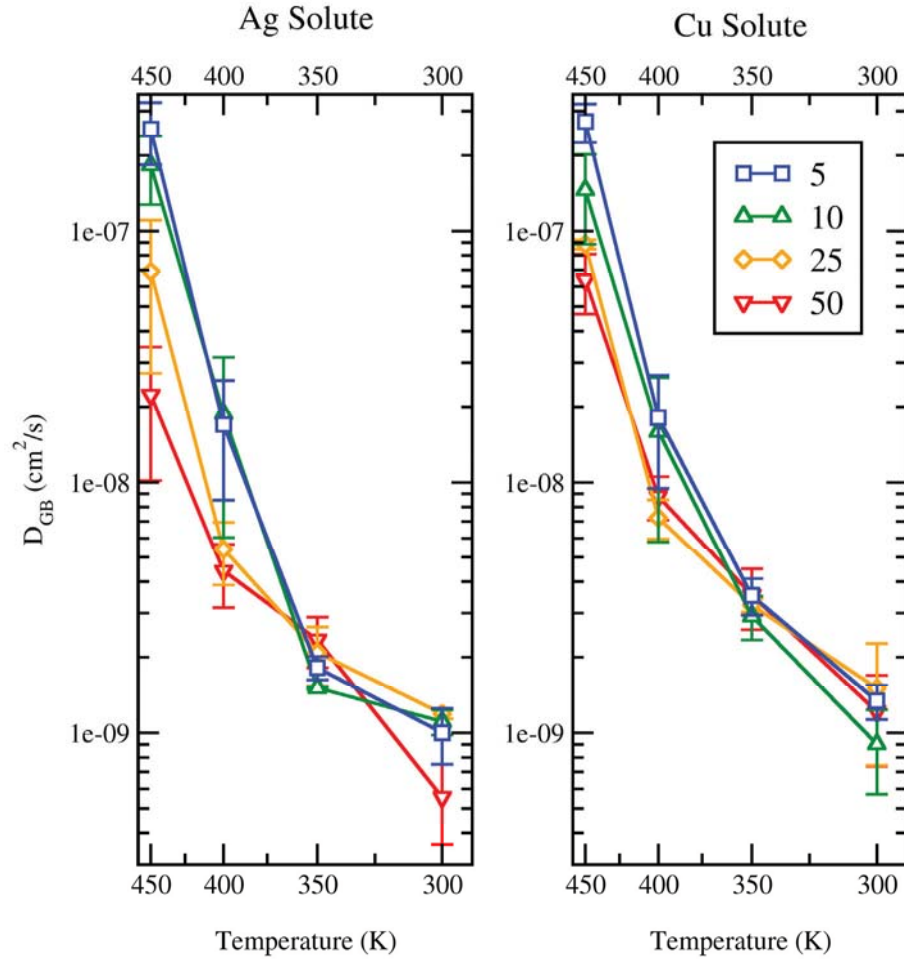


**Figure 6-8** Self-diffusivity of Sn vs. temperature for various solute atom quantities. LEFT is Ag solute, RIGHT is Cu solute.

### 6.3 Conclusions

This work investigated the effect of solute atoms of Ag and Cu on the self-diffusivity of Sn in the (101) symmetric tilt  $\beta$ Sn grain boundary. Through molecular dynamics simulations of various solute amounts, and over a temperature range of 300K to 450K, we show that both Ag and Cu decrease the grain boundary self-diffusivity of Sn as solute

amount in the interface increases. The magnitude of these reductions and secondary effects from each solute were also explored.

From the primary quantity of self-diffusion measurement in grain boundaries,  $\delta_{GB}D_{GB}$ , the effect of solute was shown in an Arrhenius style plot. For increasing solute amounts, the width-scaled diffusivity decreased at temperatures above 350K. There was also a greater decrease in this value for the Ag solute when compared to the Cu solute. Magnitudes at temperatures of 300K and 350K for both solute types were inconclusive regarding the effect of solute amount.

To quantify the width of the (101) grain boundary interface, planar diffusion profiles were plotted at various solute amounts and temperatures. For Ag, we saw again that an increase in the solute amount leads to a decrease in the self-diffusivity of Sn and over the range of temperatures the relative shape and width of the profiles remains constant. Profiles of Cu exhibit similar behavior in reducing the diffusivity in the interface, albeit by a smaller amount. In contrast to Ag, diffusion profiles for large amounts of Cu develop a double peak structure, with a slower diffusive “trough” at the center plane of the interface and an increased diffusive width. After visual analysis of simulation trajectories, we state that the cohesive energy of the Cu-Sn interactions creates highly coordinated clusters of Sn around single Cu atoms. This essentially induces a local order at the center of the interface and structural disorder the longer distances.

The diffusive widths of the planar profiles are also quantified using a *full-width at half maximum* analysis. From this we see no increase in the width of the (101) boundary upon

addition of Ag or increase in temperature—in fact the width is less than that of the pure (101) boundary. However, with the addition of Cu to the (101) grain boundary interface, there is an increase in width, and at solute amounts of 25 and 50 atoms, the width surpasses that of the pure (101) boundary. Also, with 50 Cu atoms in the interface, the diffusive width increases significantly with temperature to a value almost twice that of the pure interface. This is the effect of the large cohesive energy of Cu-Sn presenting itself.

Finally, using the calculated diffusive widths  $\delta_{GB}$  at each temperature and solute amount, we normalized the measured  $\delta_{GB}D_{GB}$  quantity to resolve a grain boundary diffusivity independent of width. This also allows us to comment on possible shifts in diffusion mechanisms at the interface. An Arrhenius plot of  $D_{GB}$  vs.  $T$  exhibited similar trends in the magnitude of diffusivity for each solute type and amount, as compared to the plot of  $\delta_{GB}D_{GB}$  vs.  $T$ . It is also evident that the slope of the diffusivity at a specific solute amount does not change significantly, indicating a common diffusion mechanism throughout the range of solute amounts studied.

# Conclusions and Future Work



*“This is too long.”*

There is a vast opportunity for molecular simulation to aid in the modeling of damage phenomena occurring in the electronics packaging of today’s high power devices and tomorrow’s nanoelectronics. Lead-free solder joints in particular, when under large current densities and temperature gradients, exhibit significant mass transport governed by the atomistic microstructure of the joint. Vacancies flow quickly through the joint’s  $\beta$ Sn grain boundaries leading to excess stress buildup, cracking, and eventual failure. Molecular simulation examines this problem at the atomic level and lends quantitative material properties of transport and structural behavior to micro- and macro-scale models as a way to better characterize the damage in the joint. The investigations in this dissertation are presented as contributions to larger scale damage models, and through the

study of  $\beta$ Sn surfaces, grain boundaries, and solute effects, we offer properties relating to diffusivity, boundary energy and stability, as well as justifications of experimentally observed behavior.

Chapter 3 investigates the energy and diffusivity of  $\beta$ Sn surfaces corresponding to low Miller index planes. The (100) surface is identified as exhibiting the lowest excess potential energy, and various diffusion mechanisms of an adatom moving on that surface are determined. These properties are valuable in describing void morphology and stability under electromigration in metals. We continue the study of  $\beta$ Sn structure with several molecular dynamics simulations of grain boundaries. The excess potential energy, grain boundary diffusivity, and interface width are determined for five grain boundaries in Chapter 4. The diffusivity results are in good agreement with experimental diffusion studies of polycrystalline Sn, however we find that the widths of a few of our boundaries are larger than the estimated value used in experiment. An interesting case is also presented, describing a boundary that exhibits fast channel like diffusion, but has a low excess energy. In these two chapters, simulations of pure Sn structures confirm experimental work and complement it by offering quantitative values of transport properties on surfaces and in grain boundaries, and additional parameters such as excess energies and diffusive widths.

Chapters 5 and 6 consider the effects of Ag and Cu solute addition on the  $\beta$ Sn (101) grain boundary. In Chapter 5, the excess energies of the (101) interface containing various amounts of solute are quantified, and the segregation enthalpy is determined for both Ag and Cu. Ag is shown to have a larger positive value compared to Cu, but by definition,

both lower the energy of the (101) boundary upon segregation from the bulk. Much experimental and simulation work is presented that validates this behavior. One simulation case finds the opposite, however; that Mg increases the energy of a particular Al grain boundary. Additionally, experimental work characterizing the microstructure in solder joints with different concentrations of Sn- $x$ Ag and Sn- $x$ Cu concludes that Ag increases the energy of special boundaries, to inhibit grain growth, and creating a finer microstructure full of many grain boundary types. Similarly, they state that Cu decreases the energy of special boundaries, allowing them to consume higher energy boundaries, leading to a coarser microstructure. We investigate this claim by simulating the (301) boundary, a low energy, special boundary identified in the experimental work, as well as two other medium energy boundaries. We find that Ag and Cu lower the energy of this particular boundary only slightly, much less than their effect on the (101) boundary. With respect to the computed enthalpies of segregation, statistically it is possible that Ag could increase the energy of this boundary, as its value is close to zero, albeit only slightly. The two medium energy boundaries exhibit enthalpies of segregation for both Ag and Cu that are experimentally comparable in magnitude to several reported studies. We conclude that there is a much larger driving force for Ag to stabilize higher energy boundaries, rather than increase the energy of special boundaries, and this is most likely the behavior leading to the fine microstructure present in Sn- $x$ Ag solder joints. For Cu, since it stabilizes the boundaries less, a fine microstructure does not develop in Sn- $x$ Cu joints until very high concentrations of Cu are present and an intermetallic phase is formed, pinning the  $\beta$ Sn grains. This type of structure is observed in other experimental studies.

The effects of solute addition on shear stress are also probed in Chapter 5. It is shown that while addition of Ag and Cu to the (101) boundary slightly lower the yield stress, this value is maintained during further shear. This indicates an increased resistance to boundary sliding. We also quantified the shear modulus of the (101) boundary and find that it is about 30% smaller than the experimental average value for single crystal Sn, and remains unchanged with solute addition. This discrepancy may be due to an under prediction of an elastic constant by the MEAM potential and the fact that we compute the shear modulus for a specific lattice direction.

In our final chapter, the study on solute effects is continued, and we determine to what extent the self-diffusivity of the  $\beta$ Sn (101) grain boundary is changed upon solute segregation. It is found by examination of planar diffusivity profiles that both solutes decrease the self-diffusivity, but Ag addition lowers the diffusivity of Sn to a greater extent than Cu. Also, we find for higher values of Cu, the interface disorders and the diffusive width increases to a value twice that of the pure boundary. A closer look at simulation snapshots reveal highly coordinated Cu-Sn structures, illustrating a short range order, with a longer range disorder. We explain this by comparing the cohesive energies of Ag-Sn, Sn-Sn, and Cu-Sn. Cu-Sn is the largest, and in the presence of a disordered boundary, Cu can freely coordinate with Sn in a favorable structure, thereby increasing the diffusive width of the boundary.

Taken in concert, these chapters present a microstructural picture of the lead-free solder joint. We have identified surfaces and interfaces of  $\beta$ Sn, likely present in the many structural regimes of the joint, and reported their various transport properties. Increasing

the scope of the study, we report the atomistic effects of Ag and Cu solute addition on the (101) and (301) grain boundaries, examine their separate effects on boundary energy, diffusivity, and resistance to shear stress, and provide explanations for experimentally observed grain structure.

## 7.1 Original Contributions

This dissertation presents several new and significant additions to the field of lead-free electronics packaging research. Although determined computationally, many of these are quantitative material properties that show very good agreement with experimental data. For this reason, the validity of our models is strong, and the interesting atomic scale behavior that is investigated in this work is used to explain existing experimental observations. The various contributions are singled out here.

- ◆ In Section 2.4, we use the volumetric strain in an Al lattice to develop a consistent relationship describing the relative size of a lattice vacancy via a vacancy relaxation factor. Before this work, the vacancy relaxation factor was reported in various ways, often with dimensional inconsistencies.
- ◆ The lowest energy  $\beta$ Sn surface for low index Miller planes is computed in Chapter 3, and the anisotropic tracer diffusivity is determined. This surface is shown to be present in experimental thin-film growth. At the time of publication, it is the belief that this is the first calculation of the diffusivity of a Sn surface.
- ◆ Chapter 4 details the quantification of specific grain boundary diffusivities for  $\beta$ Sn interfaces. These show good agreement with experimental work on polycrystals.

Previously uncalculated grain boundary widths and energies are reported, and a low-energy grain boundary is characterized as exhibiting fast channel diffusion.

- ◆ Through Ag and Cu solute addition studies in Chapter 5, we demonstrate that the energy of the (101), (201), and (310) grain boundaries can be reduced. This is in agreement with general theory and other general simulation work. Critical values of interfacial concentration are calculated, and it is determined that reducing the boundary energy to zero would require an extreme amount of interfacial solute.
- ◆ Additionally, we compute the shear modulus in [010] for the (101) grain boundary, and illustrate the boundary's behavior under shear, in the presence of solute. Ag and Cu are shown to improve the resistance of the boundary to slipping, in agreement with general simulation work.
- ◆ In Chapter 6, it is shown that Ag and Cu addition can dramatically reduce the self-diffusivity of  $\beta$ Sn in the grain boundary interface. Ag invokes a greater reduction because of its larger covalent radius and weaker cohesive energy, with respect to Cu.
- ◆ We also show that Cu's large cohesive energy causes local structural ordering and long-range disordering in the grain boundary. This increases the diffusive width of boundary compared to Ag addition, and at large Cu concentration, the boundary develops a bimodal planar diffusion distribution.

## 7.2 Recommendations of Future Work

With the availability of accurate interatomic potentials for Sn and its alloy interactions, much work can be done in the study of these compounds with respect to lead-free solder

joints. Possibly the chief contribution to the field from a methodology standpoint is the development of a technique to equilibrate a given amount of solute in and around a grain boundary in a reasonable amount of simulation time. This was attempted using Monte Carlo moves of solute-vacancy swaps, and expansion and contraction of local Sn neighbors. However, developing moves that gave practical Boltzmann factors proved more complicated than initially thought, and work on this project stopped. This type of scheme has worked for some other Grand Canonical simulations (an interested reader is pointed to work by Stephen M. Foiles on Ni-Cu alloys [93]), but the large difference in the Sn lattice around the neighborhood of an interstitial solute versus a vacancy creates a roadblock not easily overcome by current methods.

Another recommendation is to expand the Sn system into a larger nano- or polycrystal. This type of system may be able to connect more easily to finite element level models, if not work directly in tandem. It also represents a more direct experimentation of solder microstructure, and effects of solute can be introduced to examine the dynamics of grain growth and grain sliding. The reader is referred to a kinetic Monte Carlo simulation package in development at *Sandia National Laboratory* called SPPARKS.

Finally, in the search for better solder compounds, molecular simulation can play a big role. With the ability to parameterize the MEAM potential for single and binary component materials, potentials for new alloying compounds in Sn can be developed. Characteristics of  $\beta$ Sn, Ag, and Cu should be considered when investigating new components, and calculations improved by including a measure of entropic contributions to further quantify solute-solvent interactions in different microstructures.

# References

# Ref

- [1] Kirchheim, R., *Acta Metallurgica et Materialia* **40** (2), 309-323 (1992).
- [2] Kirchheim, R., *Materials Research Society Symposium Proceedings* **309**, 101-110 (1993).
- [3] Basaran, C., Lin, M., Ye, H., *International Journal of Solids and Structures* **40** (26), 7315-7327 (2003).
- [4] Basaran, C., Lin, M., *International Journal of Materials and Structural Integrity* **1** (1,2,3), 16-39 (2007).
- [5] Li, S. and Basaran, C. *Mechanics of Materials*, **41** (3), 271-278 (2009).
- [6] DIRECTIVE 2002/95/EC OF THE EUROPEAN PARLIAMENT AND OF THE COUNCIL, <http://eur-lex.europa.eu/LexUriServ/LexUriServ.do?uri=OJ:L:2003:037:0019:0023:EN:PDF>

- [7] NIST Materials and Metallurgy  
[http://www.boulder.nist.gov/div853/lead\\_free/props01.html](http://www.boulder.nist.gov/div853/lead_free/props01.html)
- [8] Lloyd, J.R. and K.N. Tu, Handbook of lead-free solder technology for microelectronic assemblies, 827-850 (2004).
- [9] Singh, P. and Ohring, M. *Journal of Applied Physics* **56** (3), 899-907 (1984).
- [10] Dyson, B. *Journal of Applied Physics* **37** (6), 2375-2378 (1966).
- [11] Dyson, B., Anthony, T.R., Turnbull, D. *Journal of Applied Physics* **38**, 3408 (1967).
- [12] Korhonen, M., Paszkiet, C.A, Li, C. Y., *Journal of Applied Physics* **69** (12), 8083-8091 (1991).
- [13] Sarychev, M.E., Zhitnikov, Y.V., Borucki, L., Liu, C.-L., Makhviladze, T.M., *Journal of Applied Physics* **86** (6), 3068-3075 (1999).
- [14] Sarychev, M.E., Zhitnikov, Y.V., Borucki, L., Liu, C.-L., Makhviladze, T.M., *Thin Solid Films* **365**, 211-218 (2000).
- [15] Kirchheim, R. and Kaeber, U. *Journal of Applied Physics* **70**, 172-181 (1991).
- [16] Li, S. and Basaran, C. *Computational Materials Science* **47**, 71-78 (2009).
- [17] Telang, A.U., Bieler, T.R., et al. *Journal of Electronic Materials* **33** (12) (2004).
- [18] Seo, S-K., Kang, SK., Shih, D-Y. *Journal of Electronic Materials* **38** (2) (2008).
- [19] Daw, M. S.; Foiles, S. M.; Baskes, M. I., The embedded-atom method : a review of theory and applications. North-Holland: Amsterdam, 1993.
- [20] Foiles, S. M., *Physical Review B* **32** (6), 3409. (1985).
- [21] Ravelo, R., Baskes, M.I., *Physical Review Letters* **79** (13), 2482-2485 (1997).
- [22] Baskes, M.I., *Physical Review B* **46** (5), 2727-2742 (1992).
- [23] Baskes, M.I., *Modeling Simulation in Materials Science Engineering* **2**, 505-518 (1994).
- [24] Huang, H., Ghoniem, N., Wong, J., Baskes, M.I., *Modeling Simulation in Materials Science Engineering* **3**, 615-627 (1995).
- [25] Gullet, G.M., Wagner, G., Slepoy, A., *Sandia Report SAND2003-8782*

- [26] Baskes, M.I., Muralidharan, M.S., Valone, S.M., Cherne, F.J. *Journal of Minerals, Metals, and Materials Society* September, 41-50, (2003).
- [27] Dong, H., Fan L., Moon, K., Wong, CP., Baskes, MI., *Modeling Simulation in Materials Science Engineering* **13**, 1279-1290 (2005).
- [28] Aguilar J.F., Ravelo, R., Baskes, M.I., *Modeling Simulation in Materials Science Engineering* **8**, 335-344 (2000).
- [29] NRL Crystal Lattice., <http://cst-www.nrl.navy.mil/lattice/> (2009).
- [30] Sutton, P.G. and Balluffi, P.G. Clarendon Press, Oxford. (1995).
- [31] Lutsko, J.F., Wolf, D., Yip, S., Phillpot, S.R., Nguyen, T. *Physical Review B* **38**, 16 (1988).
- [32] Jonsson, H., Mills, G., Jacobsen, K.W., *Classical and Quantum Dynamics in Condensed Phase Simulations* (1998).
- [33] Bolhuis, P.G., Chandler, D., Dellago, C., Geissler, P.L., *Annual Reviews in Physical Chemistry* **53**, 291-318 (2002).
- [34] Henkelman, G., Jonsson, H., *Journal of Chemical Physics* **111** (15), 7010-7022 (1999).
- [35] Olsen, R.A., Kroes, G.J., Henkelman, G., Arnaldsson, A., Jonsson, H., *Journal of Chemical Physics* **121** (20), 9776-9792 (2004).
- [36] Wert, C., Zener, C., *Physical Review* **76** (8), 1169-1175 (1949).
- [37] Gomer, R., *Reports on Progress in Physics* **53** (7), 917-1002 (1990).
- [38] Ratsch, C., Scheffler, M., *Physical Review B* **58** (19), 163-166 (1998).
- [39] Frenkel, D., Smit, B. *Academic Press, Elsevier, San Diego* (2002).
- [40] Koblinski, P., Wolf, D., Phillpot, S.R., Gleiter, H. *Philosophical Magazine A* **79**, 11 (1999).
- [41] Suzuki, A., Mishin, Y. *Journal of Materials Science* **40**, 3155-3161 (2005).
- [42] Ciccotti, G., Guillope, M., Pontikis, V. *Physical Review B* **27**, 9 (1983).
- [43] *Collected Works of J.W. Gibbs, Vol. 1. Longmans Green and Co., New York* (1928).

- [44] McLean, D. Clarendon Press, Oxford. (1957).
- [45] Weissmuller, J. *Journal of Materials Research* **9** (1) (1994).
- [46] Millet, P.C., Selvam, R.P., Bansal, S., Saxena, A. *Acta Materialia* **53**, 3671-3678 (2005).
- [47] Millet, P.C., Selvam, R.P., Saxena, A. *Acta Materialia* **46**, 297-303 (2005).
- [48] Millet, P.C., Selvam, R.P., Saxena, A. *Acta Materialia* **55**, 2329-2336 (2007).
- [49] Blech, I. A.; Herring, C., *Applied Physics Letters* **29** (3), 131-133 (1976).
- [50] Gleixner, R. J.; Nix, W. D., *Journal of Applied Physics* **86** (4), 1932-1944 (1999).
- [51] Bassman, L. C. Stanford University, Palo Alto, California, (1999).
- [52] Doyama, M.; Cotterill, R. M. J., Gordon and Breach Science: New York, pp. 79-165 (1967).
- [53] Shewmon, P. G., Diffusion in Solids, Minerals, Metals, & Materials Society Warrendale, PA, p. 246 (1989).
- [54] Zimmerman, J. A.; Webb III, E. B.; Hoyt, J. J.; Jones, R. E.; Klein, P. A.; Bammann, D. J., *Modeling and Simulation in Materials Science and Engineering* **12** (4), S319 (2004).
- [55] Hardy, R. J., *Journal of Chemical Physics* **76** (1), 622-628 (1982).
- [56] Zhou, M., *Proceedings of the Royal Society A: Mathematical, Physical and Engineering Sciences* **459**, 2347-2392 (2003).
- [57] Plimpton, S., *Journal Computational Physics* **117** (1), 1-19 (1995).
- [58] LAMMPS Molecular Simulator, <http://lammps.sandia.gov> (2010).
- [59] Balzer, R.; Sigvaldason, H. *Physica Status Solidi B: Basic Research* **92** (1), 143-147 (1979).
- [60] Ryu, J.T., Fujino, T., Katayama, M., Kim, Y.B., Oura, K. *Applied Surface Science* **190**, 139-143 (2002).
- [61] Kim, D., Lu, W. *Journal of the Mechanics and Physics of Solids* **54**, 2554-2568 (2006).

- [62] Wang, W. and Suo, Z. *Journal of Applied Physics* **79** (5), 2394-2403 (1996).
- [63] Gungor, M. and Maroudas, D. *Journal of Applied Physics* **85** (4), 2233-2246 (1999).
- [64] Sorensen, M.R., Mishin, Y., Voter, A.F., *Physical Review B* **62** (6), 3658-3672 (2000).
- [65] Henkelman G., Jonsson, H., *Journal of Chemical Physics* **115** (21), 9657-9665 (2001).
- [66] Henkelman, G., Jonsson, H., *Physical Review Letters* **90** (11), 116101/1-116101/4 (2003).
- [67] Zhang, J-M., Ma, F., Xu, K-W. *Applied Surface Science* **229**, 34-42 (2004).
- [68] Zhang, J-M., Wang, D-D., Xu, K-W. *Applied Surface Science* **252**, 8217-8222 (2006).
- [69] Zhao, M., Zheng, W., Jianchen, L., Wen, Z., *Physical Review B* **75** (8) (2007).
- [70] Huang, F.H., and Huntington, H.B., *Physical Review B* **9** (4), 1479-1487 (1974).
- [71] Peterson, N.L. *Solid State Physics*. 22:429-430 (1970).
- [72] Sun, P.H. and Ohring, M., *Journal of Applied Physics* **47** (2), 478-485 (1976), and references therein.
- [73] Basaran C., Li S., Hopkins, D.C., Veychard, D. *Journal of Applied Physics* **106**, 013707 (2009).
- [74] Suzuki, A., Mishin, Y. *Interface Science* 11, 131-148 (2003).
- [75] Telang, A.U., Bieler, T.R., et al. *Journal of Materials Research* **17**, 9 (2002).
- [76] Etomica Simulation API, <http://www.etomica.org> (2010).
- [77] Mishin, Y., Farkas, D. *Philosophical Magazine A* **78**, 1 (1998).
- [78] Fisher, J.C., *Journal of Applied Physics* **22** (1951).
- [79] Seo, S-K, Kang, DK, Shih, D-Y, Lee, H-M. *Microelectronics Reliability* **49**, 288-295 (2009).

- [80] Sellers, M.S., Schultz, A.J., Basaran, C., Kofke, D.A. *Physical Review B* **81** (1) (2010).
- [81] Rottler, J., Robbins, M. *Physical Review E* **68**, 011507 (2003).
- [82] Horstemeyer, Baskes, M.I., Plimpton, S.J. *Acta Materialia* **49**, 4363-4374 (2001).
- [83] Namilae, S., Chandra, N., Neigh, T.G. *Scripta Materialia* **46**, 49-54 (2002).
- [84] Divinski, S., Lohmann, M., Herzig, C. *Acta Materialia* **49**, 249-261 (2001).
- [85] Divinski, S., Ribbe, J., Schmitz, G., Herzig, C. *Acta Materialia* **55**, 3337-3346 (2007).
- [86] Kirchheim, R. *Acta Materialia* **50**, 413-419 (2002).
- [87] Adams, P.J. Massachusetts Institute of Technology MS Thesis, Drapier Lab (1986).
- [88] Basaran, C., Jiang J. *Mechanics of Materials* **34**, 349-352 (2002).
- [89] Qi, Y., Krajewski, P.E. *Acta Materialia* **55**, 1555-1563 (2007).
- [90] Millett, P.C., Selvam, R.P., Saxena, A. *Materials Science and Engineering A* **431**, 92-99 (2006).
- [91] Bernardini, J., Gas, P., Hondros, E.D., Seah, M.P. *Proc. R. Soc. Lond. A* **379** (1982).
- [92] Diffusion Processes in Advanced Materials. D. Gupta, editor. William Andrew Publishing, Norwich, NY (2005).
- [93] Foiles, S.M., *Physical Review B* **40** (17), 11502-11506 (1989)

[ \* ] Quotations from the character Polonius in Shakespeare's *Hamlet* begin each chapter.